University of Wollongong
Research Online

University of Wollongong Thesis Collection 2017+ University of Wollongong Thesis Collections

2021

Vortex pinning and critical current control and enhancement by magnetic structure and artificial arrays in YBa2Cu3O7-δ superconductor thin films

Mustafa Al-Qurainy

Follow this and additional works at: https://ro.uow.edu.au/theses1

University of Wollongong
Copyright Warning
You may print or download ONE copy of this document for the purpose of your own research or study. The University does not authorise you to copy, communicate or otherwise make available electronically to any other person any copyright material contained on this site.
You are reminded of the following: This work is copyright. Apart from any use permitted under the Copyright Act 1968, no part of this work may be reproduced by any process, nor may any other exclusive right be exercised, without the permission of the author. Copyright owners are entitled to take legal action against persons who infringe their copyright. A reproduction of material that is protected by copyright may be a copyright infringement. A court may impose penalties and award damages in relation to offences and infringements relating to copyright material. Higher penalties may apply, and higher damages may be awarded, for offences and infringements involving the conversion of material into digital or electronic form.

Unless otherwise indicated, the views expressed in this thesis are those of the author and do not necessarily represent the views of the University of Wollongong.

Research Online is the open access institutional repository for the University of Wollongong. For further information contact the UOW Library: research-pubs@uow.edu.au

Vortex pinning and critical current control and enhancement by magnetic structure and artificial arrays in $YBa_2Cu_3O_{7-\delta}$ superconductor thin films

By

Mustafa Al-Qurainy

Supervisor:

Prof. Alexey V Pan

Co-supervisor:

Associate Prof. Josip Horvat

This thesis is presented as part of the requirement for the conferral of the degree:

Doctor of Philosophy

University of Wollongong

School of Physics

Institute for Superconducting & Electronic Materials (ISEM)

March 2021

Acknowledgements

I am very grateful to Professor Alexey V. Pan School of Physics at UOW, for providing me with the opportunity for investigating this great topic. I also would like to thank him for allowing me to join his wonderful group as well as for his support, guidance, discussions, and valuable feedback on thesis writing.

Also a big thank to Dr Sergey Fedoseev at the PLD laboratory, for helping me to get involved and learn everything related to the thin film growth process that was required for this investigation, which is considered as a basic foundation stone for studying superconductors properties

My sincere thanks to my fellow students from Alexey's group at ISEM: Jonathan George, Frederick Wells, Antony Jones, Alaa Hamood and Cankut Eker for scientific discussions and knowledge sharing at meetings of our group, and for help with the laboratory work skills that were acquired along of my PhD study journey.

Also to whom financially supported me that funded study and, the living costs for my family, and provided all the facilities for my studies before coming to Australia. Many thanks to the Iraqi Ministry of Higher Education and Scientific Research for giving me this opportunity.

To all ISEM staff members and technicians, I would like to extend my thanks and appreciation for training on equipment, technical support, servicing and maintenance of other laboratory devices, which were indispensable for completing this project.

Last but not least, I would like to thank my parents and beloved family members for their constant moral support throughout the duration of this intensive study.

Thanks to all,
Mustafa

Certification

I, **MUSTAFA AL-QURAINY**, declare that this thesis submitted in fulfilment of the requirements for the conferral of the degree **Doctor of Philosophy**, from the University of Wollongong, is wholly my own work unless otherwise referenced or acknowledged. This document has not been submitted for qualifications at any other academic institution.

MUSTAFA AL-QURAINY

31st of March 2021

Abstract

Superconductivity provides revolutionary solutions to practical applications, such as magnetic resonance imaging, fault current limiters, and unsurpassable sensitivity and characteristic for electronics and quantum computing, which to date are unattainable by more conventional technologies. The is still a lot can be improved in making superconductors cheaper, more reproducible and robust to enable even easier and broader paths into our everyday lives.

One of the most versatile superconductor with strong potential for many types of technologies and corresponding applications is $YBa_2Cu_3O_{7-\delta}$ (YBCO), a high temperature superconductor (HTS) ceramic material. This material can be manufactured in the form of high quality single-crystalline epitaxial films, not only on small chips for electronic devices, but also on large area wafers and tapes over a hundred meters long for cellular communication filters and electric power generation, handling and transmission. They suffer, however from the relatively low degree of reproducibility of their functional characteristics, especially for devices required for electronics and quantum computation, for which highly accurate and reproducible functionalities are required. This reproducibility problem stems from the fact that YBCO has four elements in its crystal structure, which are rather difficult to grow in a perfectly ordered fashion.

In this work, a new approach enabling the functionalities required of superconducting films for applications is proposed. Different novel methods are investigated, so that materials such as YBCO that are, manufactured in the form of thin films can be less dependent on structural imperfections, on the one hand, but, on the other hand, can be developed with the necessary defect structures in the thin films, either naturally or artificially, fulfilling the optimal conditions for superconducting vortex pinning, which governs the current-carrying abilities necessary for applications.

High quality HTS thin films of $YBa_2Cu_3O_{7-\delta}$ grown on single crystal substrates by the pulsed laser deposition (PLD) technique have been manufactured with optimal current-carrying characteristics are currently being considered for potential applications. For commercial recognition, however, these films have to still show a reduction of the cost to performance ratio, as well as to allowing a certain degree of control, enabling tuning for

particular application needs. In particular, high critical temperature and critical current density as a function of the applied magnetic field are main objectives.

With this in mind, combinations of YBCO superconducting thin films with magnetic materials have been explored. Magnetic materials have been proven to be beneficial for achieving such goals. The research that has been carried out so far, however, was either technologically expensive, requiring a submicron range of magnetic features to be involved, or the available results to be inconclusive. In addition, magnetic pinning has so far been experimentally elusive on the global scale making it useless for applications.

A fundamental understanding of vortex matter behaviour in underlying superconductor materials as based on vortex-vortex and vortex-pinning sites interactions, and their dependence on temperature and applied magnetic field can provide a crucial conception of a rational design desirable that could enhance superconductor performance. Therefore, magnetic pinning is another objective in achieving enhanced critical current density in this research, with various pinning scenarios combining natural and artificial pinning landscapes.

In order to enhance and/or control critical current density (J_c) in superconducting thin films, different arrays of micrometre-scale large ferromagnetic (iron) dots with differing configurations and shapes have been deposited on top of high-quality YBCO thin films capped with a layer of insulating and non-magnetic CeO_2. Micron-size dots have been hardly considered in the literature so far, since the main consensus is that in order to control J_c, the features fabricated with this goal in mind have to be of the order of the superconducting coherence length that is the nanoscale range. This work, however, clearly shows that this is not the case. Some tremendous J_c enhancement of up to nearly 100% has been obtained at high temperatures and low magnetic fields.

It was found, however, that the J_c performance is strongly dependent on the array configurations, shape and amount of ferromagnetic iron involved. The results are clearly different to those for similar non-magnetic array structures, which directly proves the magnetic origin of the changes obtained.

Another approach to enable a J_c enhancement is to use magnetic properties of the ferromagnetic material and active interactions between superconducting films and magnetic layers of different thicknesses if these two types of antagonistic materials are

combined in hybrid heterostructures. Moreover, taking into account that the second generation of superconducting HTS YBCO tapes (the so-called coated conductors) can be manufactured on magnetic templates, this research successfully explores the combination of materials that are chemically incompatible: oxide YBCO superconducting films and metallic (iron) layers deposited with the same pulsed laser deposition (PLD) technique on top of the YBCO material. These two materials are separated by a thin intermediate non-magnetic and insulating layer of CeO_2 about 10 nm thick to avoid both possible proximity effects and direct contact, as well as oxidation for iron, oxygen loss for YBCO, unwanted inter-diffusion, and the corresponding degradation of properties.

Spectacularly, not only was J_c enhancement obtained over a certain range of the applied magnetic field, but significant, unexpected enhancement of the critical temperature has also been observed. These results show an enormous potential for such an approach, which is obviously beneficial for a range of superconducting parameters in an unexpected way. It is important to note that the critical current enhancements are achieved at high temperatures. This is likely due to a peculiarity of magnetic pinning, which is independent of temperature, unlike pinning driven by both natural defects and artificial structures, including dots.

In this thesis, these results are presented, investigated and discussed. Different pinning mechanisms and magnetic interactions are considered and proposed for explanations of the observations. The results obtained can be useful for both electronics for critical current manipulations, and for electricity handling, generation and transmission through the enhancement of the critical current density.

Table of Contents

List of Figures

List of Tables

List of Symbols and Abbreviations

HTS	*High-Temperature Superconductors*
YBCO	*Yttrium Barium Copper Oxide* $YBa_2CuO_{7-\delta}$
B_a	*Applied Magnetic Field*
B_{c1}	*Lower Critical Field*
J	*External Electrical Current*
F_L	*Lorentz force*
J_c	*Critical Current Density*
B_{c2}	*Upper Critical Field*
T_c	*Critical Temperature*
I_c	*Critical Current*
PLD	*Pulsed Laser Deposition*
STCE	*Sputtering Thermal Co-Evaporation*
CVD	*Chemical Vapour Deposition*
LPE	*Liquid Phase Epitaxy*
MOD	*Metal Organic Deposition*
LHe	*Liquid Helium*
T	*Temperature*
λ_L	*London penetration depth*
λ_o	*London penetration depth at zero temperature*
ψ_x	*superconductivity wave function*
n_s	*charge carriers for superconductors, saturation point*
ξ	*Coherence Length*
κ	*Ginzburg-Landau Parameter*
BCS	*Bardeen, Cooper and Schrieffer theory*
H_c	*Critical Field*
$\Phi_\circ$	*Magnetic Flux Quantum*
h	*Planck's constant*

e	*Electron Charge*
η	*Anisotropy Factor*
ρ	*Resistivity*
E	*Electric Field*
F_P	*Pinning Force*
J_d	*Depairing Current*
H_{irr}	*Irreversibility Field*
χ	*Susceptibility*
μ	*Permeability*
$\mu_{\circ}$	*Permeability of Free Space*
M_{sat}	*Saturation Magnetization*
U_{cp}	*Maximum Potential Pinning Energy*
U_{mp}	*Magnetic Pinning Energy*
SC	*Superconductor*
FM	*Ferromagnetic*
SQUID	*Superconducting Quantum Interference Device*
MRI	*Magnetic Resonance Imaging*
SMES	*Superconducting Magnetic Energy Storage System*
MBE	*Molecular Beam Epitaxy*
PVD	*Physical Vapour Deposition*
UV	*Ultraviolet light*
CIF	*Crystallographic Information File*
IBE	*Ion-Beam Etching*
Ar^+	*Argon ions gas*
MPMS	*Magnetic Properties Measurement System*
PPMS	*Physical properties Measurement System*
VSM	*Vibrating Sample Magnetometer*
ZFC	*Zero Field Cooling*
ΔT	*Transition width of M-T curve*

Δm	*Magnetic Moment*
W_p, L_p	*width and length dimensions of thin film sample*
ΔM	*Magnetization*
ETO	*Electrical Transport Option*
S	*cross-sectional area*
TEM	*Transmission Electron Microscopy*
SEM	*Scan Electron Microscopy*
APCs	*Artificial pinning sites*
d_s	*Superconducting Film thickness*
H_n	*Matching Field*
A_{uc}	*Unit Cell Area of the Artificial Pinning sites lattice*
RFM	*Radio frequency*

Chapter 1

Introduction and Research Objectives

1.1 Introduction

1.1.1 Background

One of the major sources of the weak efficiency of traditional electronic devices is energy dissipation, leading to possible overheating and even malfunction. Superconducting electronics, however, exhibit great potential, some unique characteristics, and unsurpassed performance not attainable by conventional counterparts in advanced computing, particularly in electronics insensitive to radiation, in ultra-sensitive detectors and receivers while enabling low energy consumption [1]. So, interest in developing superconductor electronics has been reinforced by the search for loss-less energy solutions in applications dependent on high-performance, especially quantum computing. This makes technical applications using the special superconducting properties increasingly attractive [2]. Therefore, high quality superconducting materials consuming lower power, having low noise, a high transition temperature, high critical fields, and high critical current densities are required.

The high-temperature superconductor (HTS) $YBa_2Cu_3O_{7-\delta}$ (YBCO) is one of the most promising materials for applications and hence it has been intensively investigated by many researchers since its discovery in 1986. Although it has a lower transition temperature of 92 K compared with other complex cuprates based on Bi, Tl, and Hg, which have critical temperature (T_c) values up to the current record at ambient pressure of 138 K [3], YBCO has lowest anisotropy, and correspondingly, the most beneficial structural and electromagnetic properties, which are exploited for electronics as well as for high current and high power applications. YBCO is relatively simple to fabricate (compared to Bi-, Tl- based superconductors). It is not harmful to health. YBCO retains a higher current carrying ability in the presence of magnetic fields. Its superconductivity, however, experiences deterioration at higher temperatures and in strong magnetic fields.

The important issue is to improve the efficiency of current transmission for HTS YBCO, as well as making its superconducting properties more reliable, robust, and reproducible, which is associated with difficulty in fabrication for practical applications.

Research has made a significant progress towards achieving a high critical current density (J_c) in YBCO thin film, which represents the main goal of most efforts in fundamental research. A strong increase of J_c can be achieved by immobilising the vortex motion. Effective artificial pinning centres can be introduced for higher critical current density at higher magnetic fields and higher temperatures.

At an applied magnetic field B_a larger than the lower critical field B_{c1}, vortices are manifested inside superconductors as single quanta of magnetic flux composed of supercurrents circulating around normal cores, and arranged in a triangular array (Abrikosov vortices). By applying an external electric current J in the superconductor, a Lorentz force $F_L = J \times B$ is exerted on vortex lines that is perpendicular to both the current direction J and the applied magnetic field B_a. Once the current goes up to a threshold value (critical current density), the vortices are set in motion. Energy dissipation induced by movement of vortices, limits the high current carrying capability of superconductors [4, 5].

The critical current density $J_c(B_a,T)$ is a parameter at which a superconductor can sustain a maximum electrical current value, above which the material passes to the normal state. So, critical current density considered as a crucial factor for various applications [6, 7]. Figure 1.1 shows that J_c is highly dependent on two parameters, temperature and applied magnetic field [8], because the superconductivity may be either destroyed by overlapping of the expanded normal cores of vortices at the upper critical field B_{c2} or at the critical temperature T_c, respectively. The absence of dissipation is however restricted to current densities lower than the critical value J_c, which is denoted as the critical current I_c for a superconductor wire with a defined cross-section. Therefore, superconductors are considered as the best candidate for wider potential applications to fulfil the essential requirement to carry electric current without losses [9].

Crystalline defects induced during epitaxial thin film growth, such as grain and twin boundaries, dislocations [10, 11], non-superconducting precipitates, oxygen vacancies [12, 13], etc., act as pinning sites. Different successful approaches have been employed to the maximize critical current density J_c by introducing artificial defect structures (nonmagnetic pinning) into superconductors for trapping vortices, including substrate engineering [14], manufacturing of micrometre-scale holes [15], and heavy ion irradiation [16], as well as multilayering [17]. The difficulties, however, in the technological control of the distribution and density of crystalline defects in thin film structures to produce the desired influence is a big challenge. Progress has been made on the engineering of introducing and controlling artificial pinning sites, and the performance of YBCO superconductor was improved dramatically. Moreover, pinning on structural defects is less effective with increasing temperature and above boiling point of liquid nitrogen (LN_2) thermal fluctuation effects are more dominant.

Another possible approach to maximizing J_c is associated with introducing and manipulating extrinsic pinning sites which suppress superconductivity locally. This is in contrast to defect pinning (intrinsic pinning), which is characterized by pinning the magnetic flux rather than the normal cores of vortices. In other word, magnetic flux interacts directly with the pinning sites (attractive interaction) for vortex pinning. Therefore, magnetic pinning is considered a promising approach at high temperature for trapping the vortices, so long as a large force is required to move the vortices [18, 19].

Substantial progress has been focused on the development of $YBa_2Cu_3O_{7-\delta}$ (YBCO) by taking into consideration the fabrication processes for high quality (more homogeneous) superconducting thin films, such as by Pulsed Laser Deposition (PLD), Sputtering Thermal Co-Evaporation (STCE), Chemical Vapour Deposition (CVD), Liquid Phase Epitaxy (LPE), and Metal-Organic Deposition (MOD) [20, 21]. Pulsed laser deposition is considered more convenient and efficient for the synthesis of high temperature superconducting thin films, because it meets all the criteria for the best deposition characteristics, as represented by the quality of the thin film compared with others, a lower level of contamination for film growth, a high deposition rate, and good thin-film stoichiometry which is a replica to the target due to the short pulses of the laser [5, 22].

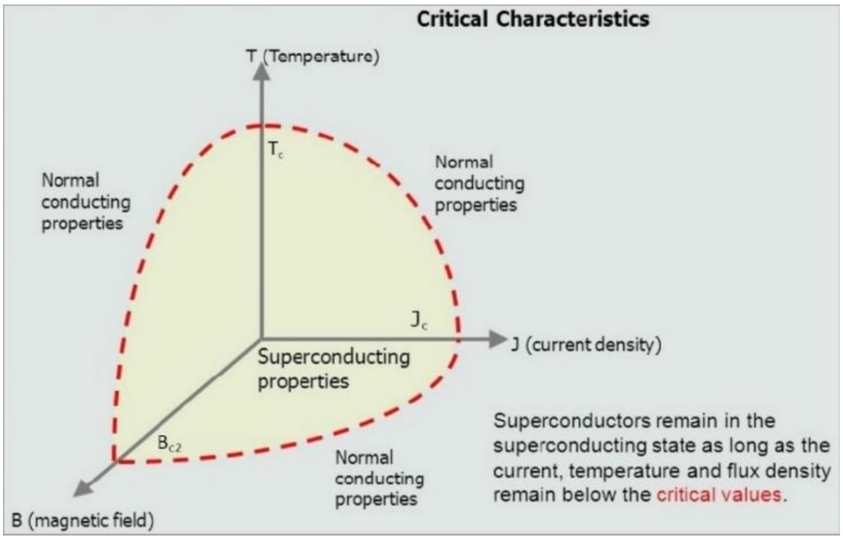

Figure 1.1 *Critical phase diagram of superconductors [8].*

1.2 Objectives of project

This research aims to focus on studies that involve both manufacturing and the characterization of high quality YBCO thin films, as well as combining them in hybrid structures with ferromagnetic materials, and exploring the influences on their superconducting behaviour prior and post to introducing various artificial hybrid structures and pinning sites. Distortion of the crystal lattice in a thin film is more likely to take place upon introducing artificial structure. In addition, the antagonistic nature of both superconducting and ferromagnetic materials poses an addition challenge for achieving the enhancement of both material aspects and superconducting properties.

The pulsed laser deposition technique was applied for thin film epitaxial growth. YBCO superconductor properties are susceptible to the deposition conditions, such as the substrate temperature, oxygen pressure, annealing time, and distance between the target and the substrate. These conditions have been, to a large extent, optimized in previous studies. Therefore, the effect of these parameters in relation to T_c and J_c will be taken into account in this work. Moreover, this research has an emphasis on investigating the effect of architecture design and inclusion of artificial magnetic pinning sites, which are on the order of micro-meter in size. Artificial magnetic structures having this dimensionality have not been studied to a large extent, in contrast to other pinning sites, which have a size on the order of the superconductor coherence length. Pinning sites in sizes considerably larger than the coherence length will be effective in trapping magnetic flux [23]. Also, exploiting the distribution density of pinning site configurations (periodicity) is an effective way for trapping vortices between the dots (interstitial vortices). Increased interaction between trapped vortices and those at interstitial positions (between pinning sites) has a significant influence on the pinning phenomenon [24]. The findings have been analysed and compared with the outcomes of different approach towards flux pinning (holes), taking into account different structural changes and mutual influences compared to those introduced by magnetic pinning structures and arrays.

In addition, using magnetic configurations in an asymmetric manner can contribute to rectification of the motion of flux quanta(ratchet effect), and they are potentially useful for many novel electronic device, such as superconducting transistor-like devices, superconducting quantum interference devices (SQUIDs) and superconducting qubits [25, 26]. In some cases application of an alternating current to a superconductor sample patterned with asymmetrical pinning sites can lead to vortex rectification effects, to vortex pump systems, and vortex diodes [27].

This project deals with the following issues in the quest search for enhancement of the current-carrying performance, manipulation and control of vortices, and decoding the corresponding mechanisms of vortex pinning in YBCO superconducting thin films combined with ferromagnetic materials in the form of heterostructures, various arrays, magnetic dots, and other relevant structures. Investigations have also been carried out on the enhancement and suppression of superconducting properties by varying the thickness of the ferromagnetic component in multilayered hybrid systems made of a superconductor (SC) and a ferromagnet (FM).

Chapter 2

Theory, Material, Literature Review, and Applications

2.1 Chapter outline

The following chapter gives an overview of superconductivity and the theories that have explained this phenomenon. It also deals with magnetic flux clusters (vortex clusters) and their penetration into superconductors, as well as the vortex interaction with intrinsic defects, and the effect of increased interactions by introducing artificial pinning sites to modify the order parameters of superconductors at high temperature. The mechanisms of flux pinning on pinning sites that are more attractive for vortex pinning are introduced and outlined.

This chapter also contains a description of the structure of YBCO material used to grow thin film superconductors, as well as the ferromagnetic material and the role of Fe layer thickness in switching the domain walls. A detailed literature review covering experimental developments in research efforts towards enlarging the critical current density then follows. Potential applications for superconductors are presented in this chapter in detail

2.2 History of superconductivity

Superconductivity is a phenomenon that was discovered in 1911 by the physicist H Kamerlingh Onnes at the University of Leiden. He observed that, when he had been using liquid helium (LHe) to cool mercury below 4.2 K, the electrical resistance of mercury dropped to zero, i.e. when he turned off the voltage, the current continued to flow without dissipation of energy. such a material is known to be in the superconducting state at temperatures below a transition temperature T_c.

Soon after this discovery, many alloys and compounds were detected which showed the same sharp decrease in resistivity, including Nb_3Sn (superconducting critical temperature, T_c =18.1 K) and niobium germanium (T_c = 23.2 K) [28, 29].

In 1933 W. Meissner and R. Ochsenfeld discovered a significant magnetic property when they noticed that a superconductor behaved not only as a perfect conductor but also showed perfect diamagnetism, when they noted that a superconductor could expel applied magnetic field completely below a critical temperature [30], as shown in Figure 2.1 (b) [31], which is known as the Meissner effect.

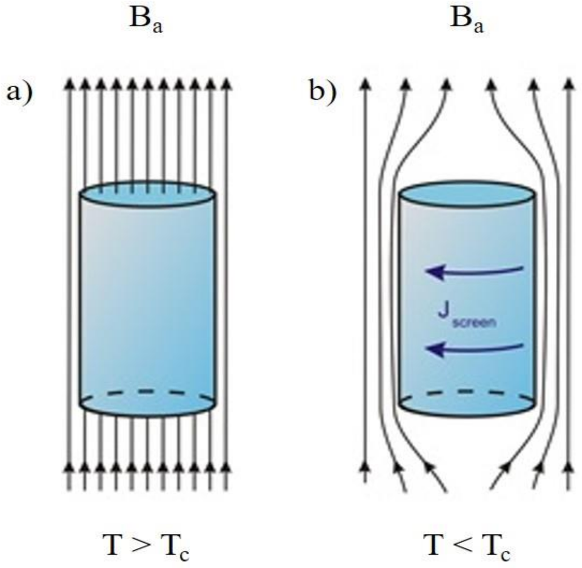

Figure 2.1 *Distribution of an applied magnetic field (B_a): a) normal conductor, b) superconductor material (Meissner effect) $B_a < B_{c1}$ [30].*

After the Meissner effect was discovered, numerous efforts were devoted to explaining the superconductivity phenomenon from the theoretical point of view. Some of them agreed well with experimental findings, others less so. The classical model of Fritz and Heinz London [32-35] developed a phenomenological theory of superconductivity in 1935. London theory incorporated with the Maxwell equations successfully described the motion of free electrons in a superconductor (perfect conductivity) and the expulsion of magnetic flux from the interior of the superconductor (perfect diamagnetism), by superconductor's generation of a screening current (Meissner current), which, in turn produces a magnetic field inside the superconductor that has the same magnitude but the opposite direction to the applied field. Moreover, the theory indicated that the external magnetic field decreases exponentially over a distance (λ) London penetration depth, which has temperature dependence and diverges at a temperature close to the critical one, according to Equation 2.1.

$$\lambda_T = \lambda_o/\sqrt{1-(T/T_c)}, \qquad 2.1$$

where λ_o is London penetration depth at zero temperature. London theory, however, was unable to explain the superconductivity of type-II superconductors, nor provide the insight into its microscopic properties, which also includes high temperature superconductors (HTS).

The Ginzburg-Landau (Vitally L. Ginzburg and Lev Landau) (GL) theory 1950 introduced an effective wave function (ψ_x) to describe the superconducting electrons [36]. The square of the wave function (ψ_x) is proportional to the number of charge carriers in the superconductor, n_s, which are bound in pairs known as Cooper pairs.

$$|\psi_x|^2 \alpha\ n_s. \qquad 2.2$$

The main result of this theory is the presence of an intermediate state of superconductors, where superconductivity and the normal state can coexist in the presence of magnetic field up to a critical field known as the second critical field (B_{c2}). Correspondingly, this theory is considered as a useful tool for investigating the mixed state of superconductors [34].

GL theory introduces the second characteristic length scale in superconductivity, known as the coherence length (ξ), which is defined as the spatial variation of the order parameter (ψ_x) at the normal-superconductor interface. The coherence length can be expressed as:

$$\xi_T = \xi_o/\sqrt{1-(T/T_c)}, \qquad 2.3$$

where ξ_o is coherence length at zero temperature. The ratio between both characteristics lengths (λ, ξ) is defined as GL parameter, $\kappa = \lambda/\xi$, which, to a large extent, determines the behaviour of superconductor materials in an applied external magnetic field, due to the penetration of so-called Abrikosov vortices. Figure 2.2 [34, 37] shows a schematic illustration of such a vortex with the parameters (λ, ξ, ψ_x and B_x).

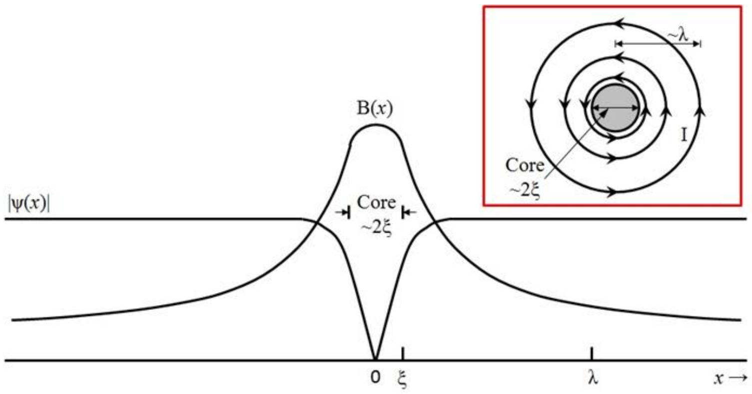

Figure 2.2 *Structure of a quantized flux line, magnetic flux in the vortex core and the order parameter (ψ_x). The inset is the distribution of current flowing around the normal core within radius of ~λ [33, 36].*

The Bardeen, Cooper, and Schrieffer (BCS) theory (1957) gave a rather precise explanation of the microscopic origins of superconductivity in materials [38]. It is based on the assumption that the so-called Bose-Einstein condensation of many pairs of bound electrons (Cooper pairs). Which have opposite momentum and spin, is carrying the supercurrent through the superconductor with less energy dissipation. The Cooper pairs are formed as a result of indirect attraction between two electrons mediated by a phonon interaction (lattice distortion). The electrons coupled in pairs (condensation state) are more stable than a single electron in the material lattice, due to having a slightly lower energy and hence experiencing zero resistance, which is the main feature exhibited by the superconductivity and is unattainable by other known materials. Since then, BCS theory has been proven in all metallic superconductors. It cannot be applied directly to superconductors possessing high critical temperatures, however, such as some metallic alloys, or to HTS (cuprates), which possess much higher T_c than any known metallic alloys. The problem with the theory arises due to thermal energy, which would cause stronger lattice vibrations and electron-phonon interactions, leading to too much scattering of electrons. These strong lattice vibrations would not allow the formation of sustained Cooper pairs, or these pair would simply fall apart, so that the material turns into the normal conductor.

2.3 Superconductors of type I and type II

Abrikosov, who first introduced the concept of type I and type II superconductors in 1957, described a new (at the time) concept of vortices according to the Ginzburg-Landau theory. He found that there is a breakpoint in the GL parameter κ, which is the ratio between the magnitudes of the penetration depth and coherence length for a superconductor material $\kappa = \lambda/\xi = 1/\sqrt{2}$. This breakpoint determines the behaviour of the superconductor when applying magnetic field, whether it belongs to the type I or II superconductor. Correspondingly, type II superconductors can also be considered to behave as soft or hard superconductors, with the hard superconductor having the ability to pin vortices and hence sustain a useful supercurrent for applications. The behaviour of these two types of superconductors in applied magnetic field is quite different. The type I superconductor with $\kappa < 1/\sqrt{2}$ displays superconductivity with the diamagnetic-like state below the critical field H_c, where the superconductor expels all magnetic field and does not allow it to penetrate into its interior, i.e., the supercurrent flows only on the surface of superconductor. This supercurrent, in turn, generates the magnetic field to oppose the external magnetic field below the critical field H_c. This state is one in which magnetic flux is expelled from the superconductor in the so-called Meissner effect. Above the critical field, the superconductivity vanishes, and the entire material becomes a normal conductor, as shown in Figure 2.3-(a).

The type II superconductors. Which have $\kappa > 1/\sqrt{2}$, show a perfect diamagnetic-like effect below the lower critical field, H_{c1}. At the magnetic field of H_{c1}, a partial penetration of magnetic flux in the form of flux lines known as vortices takes place. The number of vortices increases inside the superconductor with increasing strength of the applied magnetic field. At the applied field at which the vortices become so densely packed inside a superconductor that their cores start touching each other, the superconductivity is destroyed, turning the material into the normal state. This field at which superconductivity is destroyed is called the second (or upper) critical field (H_{c2}) [39].

Flux quantization also plays a significant role in the physics of type II superconductors. When such a superconductor is placed in a magnetic field with the strength between the first critical field H_{c1} and the second critical field H_{c2}, the field partially penetrates into the superconductor in the form of a triangular lattice of quantized tubes known as Abrikosov vortices (fluxon), so the Meissner effect is incomplete at this stage, allowing the superconductor to withstand very high magnetic fields. On the contrary, due to the current circulating on the surface of a type I superconductor, even a small magnetic field would destroy superconductivity. Abrikosov vortices (Shubnikov or mixed state) are shown in Figure 2.3-(b) [40], and 2.2 in more details, consists of a normal core, which is a cylinder of the normal (non-superconducting) phase with a diameter in the order of the 2ξ, the superconducting coherence length. The magnetic field lines pass along this normal core through the whole sample. The screening currents circulate within the London penetration depth (λ_L) from the core and screen the rest of the superconductor from the magnetic field in the core. In total, each such Abrikosov vortex carries one quantum of magnetic flux $\Phi_{\circ}$ =h/2e=2.07×10^{-15} Wb (h = Planck's constant and e = electron charge) [41].

It has long been a dream of scientists working in the field of superconductivity to find a material that becomes a superconductor at room temperature. A discovery of this type would revolutionize every aspect of modern day technology such as power transmission and storage, communication, transport, electronics and even computing.

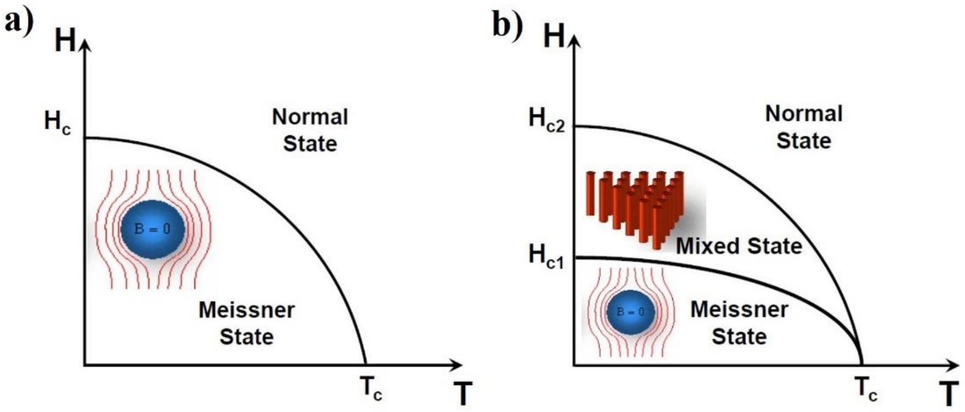

Figure 2.3 *Schematic diagram of type I a) and type II b) superconductors [40].*

2.4 High temperature superconductors

The researchers G. Bednorz and A. Muller made a breakthrough in 1986 when they discovered a high temperature superconductor (HTS) at the IBM laboratory in Switzerland. They synthesized a ceramic superconductor from lanthanum, barium, copper and oxygen (LaBaCuO) with the highest T_c = 30 K known at that time[29]. One year later in 1987, P. M. Wu et al. made the remarkable discovery of the superconductor yttrium barium copper oxide ($YBa_2Cu_3O_{7-\delta}$) with a transition temperature T_c = 92 K, which was the first superconductor material to exhibit a T_c above the boiling point of liquid nitrogen (77 K). Achieving this point of critical temperature resulted in a widening of potential superconductor applications, as liquid nitrogen is a cheaper, easier to handle, and more convenient cryogenic refrigerant than liquid helium [42]. It must be mentioned that the pressure of the need for liquid cryogens is not as high today as in the past due to the development of cryocooling technologies, which do not require any cryogens, to the extent that even large superconducting magnets can work in the cryogenic liquid-free environment.

Soon after the discovery of YBCO material, several HTS compounds were found, based on copper oxides with critical temperatures as high as 110 K in $Bi_2Sr_2CaCu_2O_{8+x}$ (x = 0.15-0.20) (BSCCO 2212) [43]. The highest critical temperature reported to date in such a compound, T_c = 134 K at high pressure, which has stirred considerable interest, was in a compound with the composition $HgBa_2Ca_2Cu_3O_8$ [44]. Figure 2.4 [45] shows the transition temperatures for superconducting materials from 1911 up to 2015.

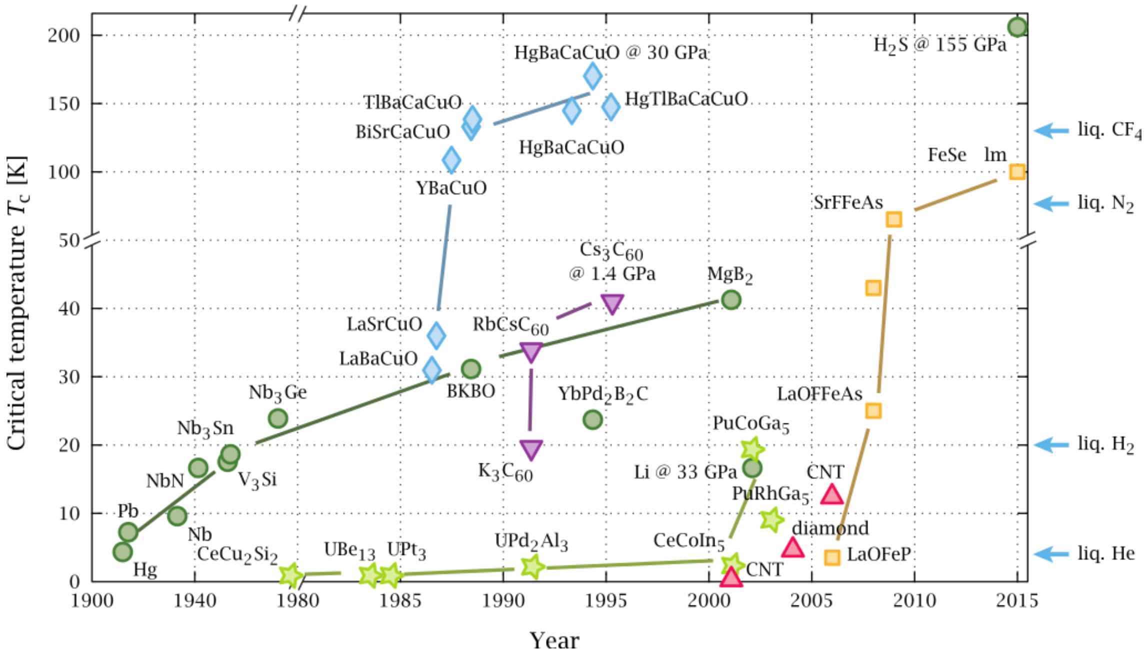

Figure 2.4 Superconducting transition temperatures (T_c) recorded through the years. [44].

2.5 Structural of YBCO

The crystal structure of YBCO superconductor is shown in Figure 2.5 [46], which has an orthorhombic unit cell with lattice parameters a = 3.82 Å, b = 3.89 Å, and c = 11.68 Å. It consists of 2 Cu-O_2 plane and 2Cu-O planes separated by a Ba-O layer with a Y layer without any oxygen atoms, so each of the Cu-O planes has its copper atoms surrounded by 4 oxygen atoms, and these planes consist of parallel Cu-O-Cu-O chains, while in the Cu-O_2 planes, the copper atoms are such surrounded by 5 oxygen atoms. The Cu-O and Ba-O layers act as a reservoirs to assist strong superconductivity in the Cu-O_2 planes [47].

Generally, YBCO displays metallic behaviour at room temperature in the *ab*-plane due to the copper-oxygen planes, which give such metallic conductivity in the normal state [47], while the electrical conductivity is lower along the *c*-axis. As a result, cuprate superconductors (YBCO) exhibit anisotropy in electrical conductivity, and this anisotropy can produce significant differences in properties along the *a-b* plane and along the *c*- axis. The anisotropy factor (η) for YBCO is 5-7, while $(Bi,Pb)_2Sr_2Ca_2Cu_3O_x$ (Bi-2223) has a high anisotropy value, ~50-100. The anisotropy factor is defined as the ratio of the upper critical field parallel to the *ab*-plane to the upper critical field perpendicular to these planes, $\eta = H_{c2}^{\parallel} \,/\, H_{c2}^{\perp}$ [48]. The strongest anisotropy for BSCCO leads to enormous suppression of the irreversibility field, H_{irr} (at which J_c vanishes) to the very low value of 0.2-0.3T at 77 K, restricting the applications for Bi-2223 at 77 K, even though H_{c2} exceeds 10 T. This is in contrast to YBCO material with a much smaller anisotropy factor (H_{irr} 5-7T at 77K) [1], implying that the latter is more practically attractive for applications.

The high anisotropy is determined by the layered structure of YBCO components, where the conductivity is confined in the *a-b* directions of Cu-O planes, and the Cu-O chains acts as charge reservoirs for providing carriers to the Cu-O planes, while conductivity along the *c*-axis is too small compared to that along the *ab*-plane. Furthermore, the anisotropy is also reflected in the length scales of YBCO (penetration depth and coherence length), where λ along the *c*-axis is fivefold greater than that in the *ab*-plane at 0 K [49], while the ξ along the *c*-axis is smaller than in the *ab*-plane, being about 1-4 nm, by the same factor [50], as indicated in Table 2.1. This is quite small compared to conventional superconductors such as niobium (~ 40 nm). The modest value of the coherence length indicates that the superconducting state is more susceptible to local disruptions from interfaces or defects on the order of a single unit cell, such as the boundary between twinned crystal domains and other crystal defects. The high sensitivity of superconductor material to small defects, as well as the degradation in their performance by humidity, leads to complicated fabrication processes for devices using these materials. In practice, to obtain higher quality superconducting films, the *c*-axis has to be oriented perpendicular to the substrate, so that current can be applied easily along the *ab*-plane [51]. The oxygen atoms in $YBa_2Cu_3O_{7-\delta}$ play a significant role in the electrical conductivity properties, so oxygen deficiency leads to implantation of holes into the CuO_2 layers. More exactly, when $\delta < 0.7$, the structure is orthorhombic, but superconductivity disappears when $0.7 < \delta$ where the structural transformation occurs from orthorhombic (metal) to tetragonal (insulator) [52].

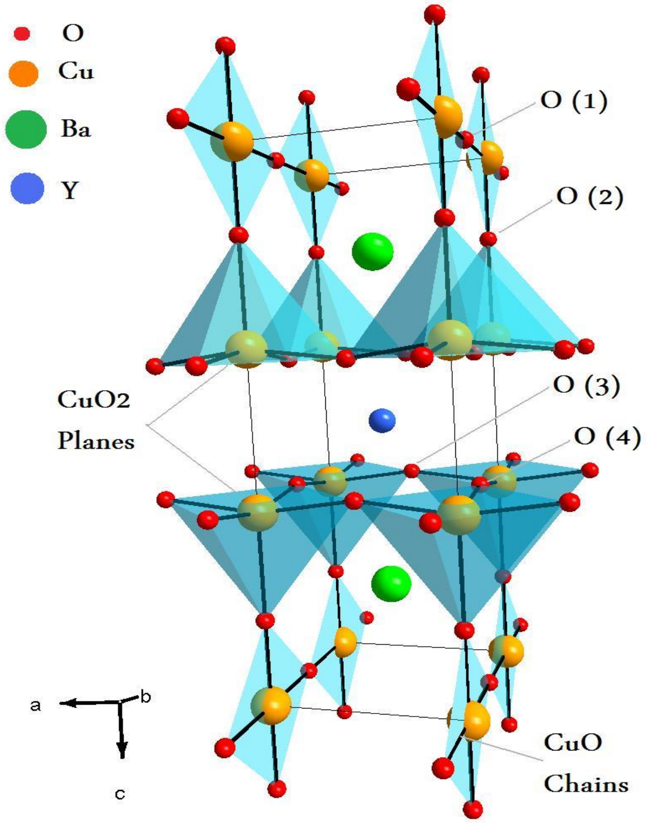

***Figure 2.5** Crystallographic structure of orthorhombic of $YBa_2Cu_3O_7$ [46].*

Table 2-1 *Optimal properties of YBCO [50].*

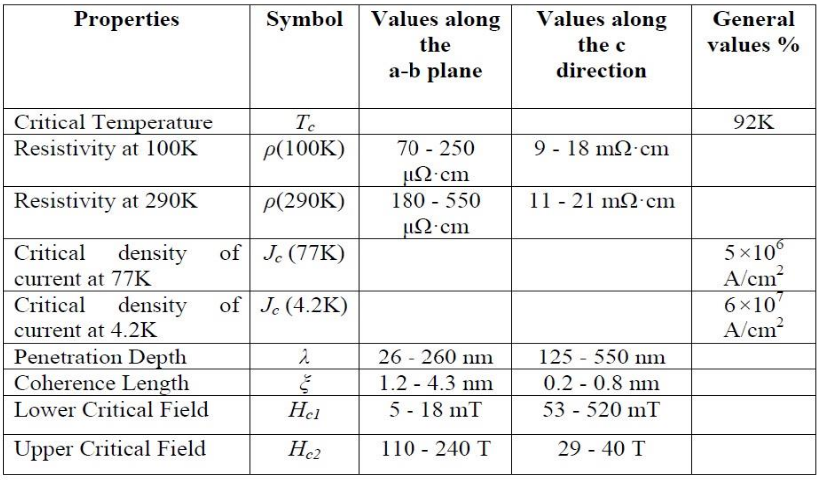

Properties	**Symbol**	**Values along the a-b plane**	**Values along the c direction**	**General values %**
Critical Temperature	T_c			92K
Resistivity at 100K	ρ(100K)	70 - 250 μΩ·cm	9 - 18 mΩ·cm	
Resistivity at 290K	ρ(290K)	180 - 550 μΩ·cm	11 - 21 mΩ·cm	
Critical density of current at 77K	J_c (77K)			5×10^6 A/cm^2
Critical density of current at 4.2K	J_c (4.2K)			6×10^7 A/cm^2
Penetration Depth	λ	26 - 260 nm	125 - 550 nm	
Coherence Length	ξ	1.2 - 4.3 nm	0.2 - 0.8 nm	
Lower Critical Field	H_{c1}	5 - 18 mT	53 - 520 mT	
Upper Critical Field	H_{c2}	110 - 240 T	29 - 40 T	

2.6 Flux pinning

The critical current density rapidly deteriorates in increasing temperature and/or applied magnetic field due to the lower pinning potential barrier of intrinsic crystalline defects at these external parameters, which also promote enhanced thermal fluctuations [53]. As mentioned before the main goal of this research is to achieve a high capability to carry electrical current (J_c) in superconductors with less dissipation of energy in the presence of a given magnetic field. Introducing artificial pinning centres plays a significant role in raising the superconductor efficiency for electrical transportation. This is despite the fact that artificial pinning sites have been widely studied over the past decade due to their fundamental as well as technological importance [54]. The emphasis in this work is placed on the artificial features, however, which are on the order of the coherence length or even larger.

2.7 Kinds of pinning sites

Flux pinning sites in superconductor materials can be present in two categories artificial pinning sites (engineered) or natural pinning sites

2.7.1 Natural pinning sites

Superconductors have various intrinsic defects, which are mostly formed during the process of thin film growth or exist in the target itself. They are the so-called natural pinning sites[10]. These natural pinning sites can be found as point or plane defects, dislocations, twin boundaries, atomic substitutions, antiphase boundaries, stacking faults, etc., see Figure 2.6. Achieving high critical current density in a superconductor with high defect density might have a deleterious effects, so controlling the defects in the superconductor rather than making it with perfect crystallinity is the main goal [55]. The presence of these types of disorder in the superconductor structure at high temperature is less effective, since thermal fluctuations cause vortices to fluctuate about their equilibrium positions [56].

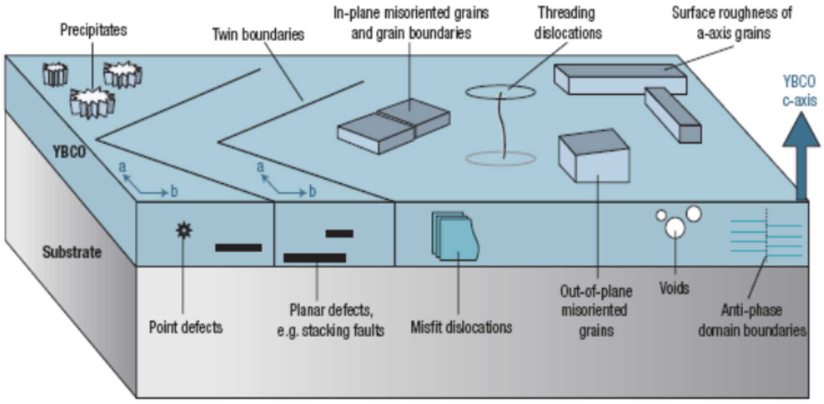

Figure 2.6 *Defects in thin film superconductor act as flux pinning sites [55].*

2.7.2 Artificial pinning sites

Many efforts have been made by researchers to increase the critical current density (J_c) in superconductors by adding artificial pinning sites using different routes such as: multilayering [17, 57, 58], introducing nanorods [59, 60], and heavy –ion irradiation [61]. Recently, artificial pinning sites were made such as microholes (antidots) [27, 62] or magnetic dots (ferromagnetic dots) [62] by using electron-beam lithography. Combining artificial and natural pinning sites is required to increase the effective pinning sites and consequently the critical current density, in contrast when superconductors containing only natural pinning sites [59, 63].

2.8 The flux pinning mechanism

In the interior of type II superconductors, with applied magnetic field in the range of $B_{c1} < B_a > B_{c2}$, magnetic flux penetrates the material in the form of a lattice of tubular structures called flux lines or vortices, each of them carrying one unit of magnetic flux equal to the flux quantum, $\Phi_\circ$ [41]. The repulsive interactions between the vortices arrange them in a regular pattern to maximize the distance between nearest neighbours [64].

As mentioned before and as indicated in Figure 2.2, the vortices are based on non-superconducting cores of radius $\xi(T)$, which is of the order of several nanometres for high temperature superconductors. The cores are surrounded by circulating superconducting screening currents and extends outward to $\lambda(T)$. Application of an electrical current to a superconductor leads to a lateral Lorentz force (F_L) exerted on the vortices, which, in turn, moves the vortices from their positions in perpendicular path to the current direction. Due to the vortex motion, energy dissipation occurs as a result, leading to resistance (resistive state), and the superconductor loses its main superconducting property of interest, which also implies degradation in its J_c value. Moreover, a finite electric field (E) is induced in the superconductor, and it is proportional and perpendicular to the vortex velocity vector, while it is parallel to the electrical current, as exhibited in Figure 2.7 [5]. Therefore, achieving sustained high critical current densities requires suppression of flux flow (vortex immobilization), i.e., introducing effective pinning sites to pin vortices in their positions.

Pinning centres induce a pinning force ($F_P = J_c \times B$) as a result of interaction between the vortex and the pinning site, so high critical current density is defined by the balance between the two forces, so $F_L = F_P$. At $F_L > F_P$, the superconductor is said to be in a state of energy disspation exceeding the maximum pinning force.

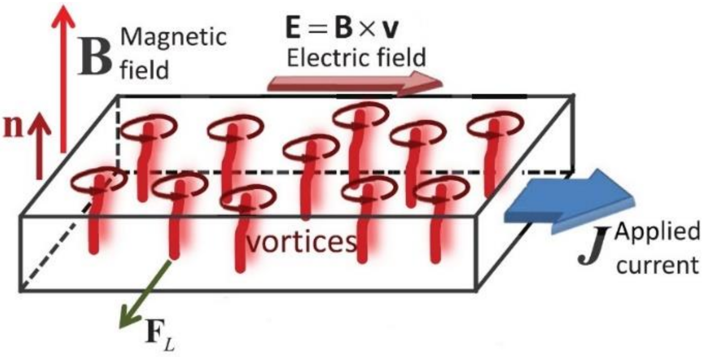

Figure 2.7 *the forces and dissipation energy when an electrical current is applied to a uniform superconductor [5]***.**

The superconducting thin-film fabrication process involves the growth of various sorts of crystalline imperfections or local material defects, which are less favourable for superconductivity (normal material) due to partially blocking electric current percolation [65]. The presence of crystal defects in a superconductor plays a significant role in pinning flux flow. It is more favourable for vortices to be pinned at these potential energy wells, since the formation of vortex cores require energy to break up the coupling of Cooper pairs, so that defects are attractive for vortices, so as to minimize their energy instead of originating their own cores.

All forms of HTSs possess crystalline defects of different kinds, which provide effective pinning sites at different temperatures. Whereas YBCO film can exhibit a J_c of value more than 10^7 A·cm^{-2} at 4.2 K, it is lower by an order of magnitude at 77 K [53, 66]. Moreover, these values are still less than the value of the depairing current (J_d) where $J_d = \emptyset_{\circ} /[\frac{3}{\sqrt{3}} \pi \mu_{\circ} \lambda^2 (T)\ \xi(T)] \approx 3\times10^8$A·cm^{-2} for YBCO at 4.2 K [1]. The depairing current is the threshold point at which a large current applied to the superconductor is strong enough to break up the Cooper pair coupling. Put differently, the kinetic energy of the supercurrent electrons exceeds the condensation energy and thus breaks down the superconducting state [5, 67, 68]. Furthermore, the results show that J_c for thin film superconductors achieves values 10-100 times higher than that for YBCO single crystals due to large intrinsic density of defects accompanying the thin film growth process [55, 69].

In addition to the limitations and considerations provided above, all applications of high temperature superconductors are limited by a lower characteristic field, known as the irreversibility field (H_{irr}). The irreversibility field is defined at the point where reversibility of magnetization loops collapses into irreversible behaviour, implying that the magnetization measurements exhibit no critical current density and hence no pinning. Sometimes, the irreversibility line is called the depinning line [69]. The H_{irr} at 77K is roughly 7 T for YBCO (far below H_{c2}). It is important to note that the irreversibility line is not a fundamental parameter and strongly depends on the sensitivity of the measurement technique, sample size, and type of measurement [70-72]. This parameter provides a key argument for developing a second generation of HTS technology for superconducting wires and cables based on YBCO. Indeed, the first generation was based on Bi-based superconducting tapes, although the irreversibility field is more than six time smaller than for YBCO [73].

2.9 Critical state Bean's model

The Bean model is phenomenological and based on a purely microscopic approach, since it describes the behaviour of vortices in the mixed (Shubnikov) state for $B_a > B_{c1}$, providing nevertheless a global description of the critical current density in a superconductor. The assumption has been proposed according to this model [74] that the entire superconductor exhibits critical current density rather than any type of its distribution. Above the critical current density J_c, a superconductor switches into a dissipative, vortex-flow state driven by the Lorentz force. As mentioned previously, flux lines are surrounded by a vortex current, so as soon as B_a exceed B_{c1}, vortices penetrate the thin film with ascending applied field from its edges, creating a flux front gradient due to microstructural imperfections (vortex pinning), as shown in Figures 2.8 and 2.9(a, b). Thus, there is a corresponding bulk current flowing perpendicular to the flux lines according to Ampere's law [75], as indicated at Figure 2.8. The centre area of the superconductor, however, will be completely free of current and flux lines. So, a superconductor can carry a current density that is determined by the density of pinning sites (if J_c is assumed to be field-independent), where the latter provide a sustained flux gradient [76].

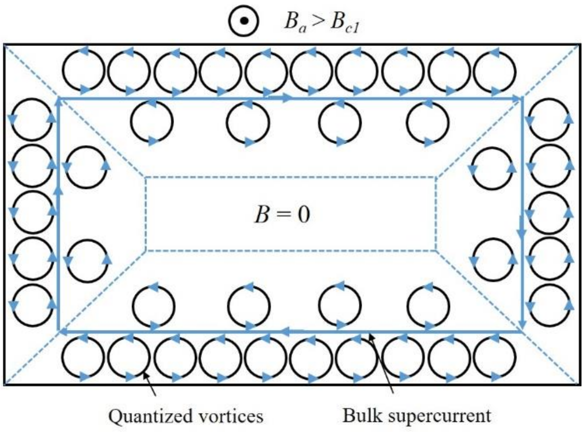

Figure 2.8 *Magnetic field distribution in the mixed state* $B_{c1} < B_a < B_{c2}$ *in a thin film superconductor.*

Since the Lorentz force increases with further increases in the current, it pushes the flux lines out of its pinning potential well, and hence, the flux front advances inward to centre area (the dotted rectangular area in Figure 2.8), and flux gradient starts to decay. On the other hand, ever more flux lines (vortices) penetrate the material with ramped up applied magnetic field B_a. The system of flux line configuration reorders itself into another metastable state, such that vortices are pinned again to realize a flux gradient, and the equilibrium with the B_a at the boundary is re-established.

In descending applied field B_a, the scenario is different and opposite of the one in ascending applied magnetic field. The vortices start to move outward from the sample edges, leaving the middle of the thin film with a high density of flux lines (with $B \neq 0$ at the dotted rectangular area shown in Figure 2.8) due to the pinning of vortices (gradient of vortex distribution) Figure 2.9(c, d). The possibility of achieving a non-uniform spatial distribution of magnetic flux lines is of fundamental significance from both a theoretical and a practical perspective. This is because the non-uniform pinning of flux lines (overall vortex density gradient) corresponds to a uniform superconducting current flow that can reach as high as the value of the critical current density. For comparison, the current density in the Meissner state can flow on the surface, bit it is limited by a tiny surface layer, so it will be not appropriate in most cases for practical applications.

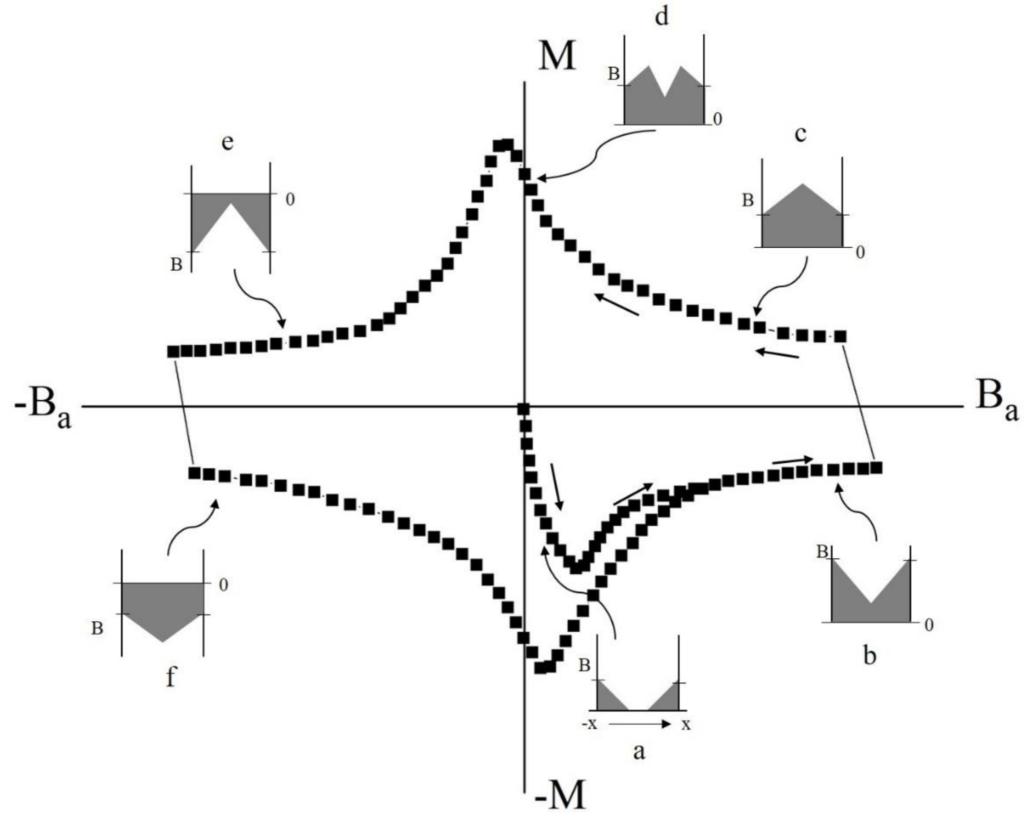

__Figure 2.9__ Field profile of magnetization hysteresis loop (M) for ascending and descending applied magnetic field (B_a) of a type II superconductor. The shaded areas represent the magnetic flux lines gradient.

2.10 Ferromagnetic materials

In general, the categories of magnetic substances are diamagnetic (repulsion with B_a), paramagnetic (slightly attracted to B_a), and ferromagnetic (strong attraction to B_a), i.e., by how these materials respond to applied magnetic field (B_a), where each material possess various order of magnetic moments or spin.

Ferromagnetic materials below the Curie temperature tend to line up their intrinsic magnetic moments in the same direction via exchange interaction. Intrinsic magnetic moments tend to align along the direction with lowest energy (easy axis of magnetization). Thus, applying an external field forces magnetic moments to flip the orientation of their magnetization upon reaching a sufficiently high values of B_a [77]. Ferromagnetic materials possess a magnetic susceptibility χ and permeability μ. These quantities are typically quite large and positive, being functions of applied magnetic field according to [78]:

$$\chi = \frac{M}{H} \qquad 2.4 \quad , \qquad\qquad \mu = \frac{B}{H}\ \frac{Tesla}{(\frac{A}{m})} \ , \qquad 2.5$$

where M is the magnetization, the relationship between susceptibility, and permeability is given as:

$\mu = 1 + 4\pi\chi$ or $\frac{\mu}{\mu_\circ} = 1 + \chi$ where $\mu_\circ$ is the permeability of free space and equals $4\pi \times 10^{-7}$ Wb/(A·m).

Ferromagnetic materials comprise spontaneously spilt domains, which is energetically favourable. Forming these configurations lowers the total energy of the system. The boundaries between domains structures are domain walls, where magnetic dipoles in different magnetization orientations are adjacent. The formation domains walls require the energy to force adjacent dipoles to rotate their magnetization direction, which is proportional to area of the wall. The domain formation process persists up to where the energy required to establish additional domain walls is greater than the reduction of magnetostatic energy consequent to the formation of domains [77].

In thin films, at an applied magnetic field, the magnetic moment rotation at domain walls take place without leaving the plane of the thin film Néel wall, thereby minimizing the demagnetization energy (stray field). Such rotation is more stable and is commonly takes place in thinner film, where the thickness is comparable to the domain wall width. Whereas, out-of-plane rotation of magnetic moments is dominant at Bloch wall structures, and it occur when the film is considerably thicker than the wall width [79]. This is where the maximum demagnetizing energy locally suppresses superconductivity. Figure 2.10 presents the configurations of Néel and Bloch walls, as well as magnetization switching when the ferromagnetic film becomes thicker. The demagnetization energy or strength of stray fields ~ $M_s^2\ \delta d$ per unit length of wall, where δ and d, are the wall and material thickness, respectively (since stability of the domain walls as a function of the film thickness is more susceptible to the demagnetizing effect). More precisely, a strong demagnetizing stray field able to realign the magnetic moments of the domains, and consequently, movement of magnetic domain walls during the magnetization reversal is more likely to take place[80].

The spanning of domain walls from Néel to Bloch as a function of magnetic film thickness has been proved experimentally in cobalt, permalloy, and nickel, where the transition from Neel to Bloch wall take place at 30 nm for Co and 20 nm for Ni [81-85].

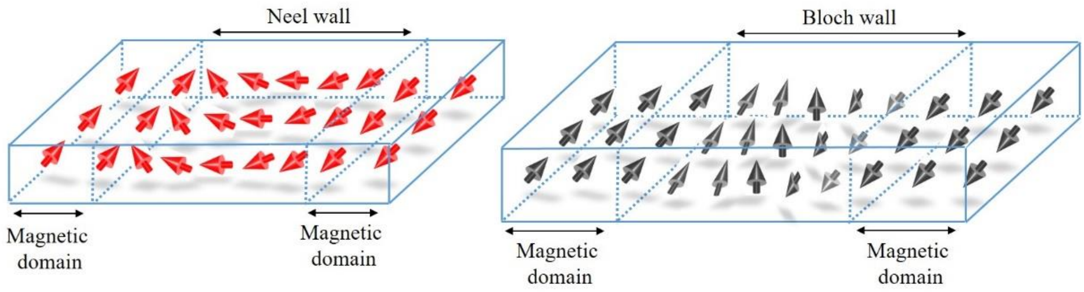

Figure 2.10 *Domain wall configurations (Bloch and Néel wall) with perpendicular magnetic anisotropy. Domain walls (DW) separate domains of magnetization pointing parallel to the film plane as shown. The difference between the two DW configurations is the direction of rotation of the magnetization from one domain to the other.*

If a superconductor (SC) is combined with a ferromagnet (FM) in some sort of hybrid structure [86, 87], in particular, if two thin films of these different materials are deposited as a bi- (or multi-)layered heterostructure, the magnetic domains and their domain walls may play a significant role in high temperature superconductors as support for the pinning mechanism of vortices [87].

Even nucleation of superconductivity can be controlled in an unusual way when driven by a hybrid structure due to the somewhat periodic organization of domains manifested in a ferromagnetic film. In this case, the superconductor is influenced by the non-uniform magnetic field profile, which can be altered by changing the magnetic domain structure and the external applied magnetic field, affecting the nucleation of the superconductivity due to its dependence on localized magnetic fields [88, 89].

The relationship between magnetization and applied magnetic field B_a is highly nonlinear. At sufficiently high fields, all atomic magnetic moments align and this achieves the maximum magnetization, called the saturation magnetization, M_{sat}, so that all of the magnetic domains are aligned to the applied field. This can be seen in a cycle of magnetisation versus applied field, as it alternates between the $+B_a$ and $–B_a$ directions, which is called a hysteresis loop. The shape of the hysteresis loop depends on material susceptibility and the magnitude of the applied field in addition to the shape and size of the sample, as it is apparent from Figure 2.11.

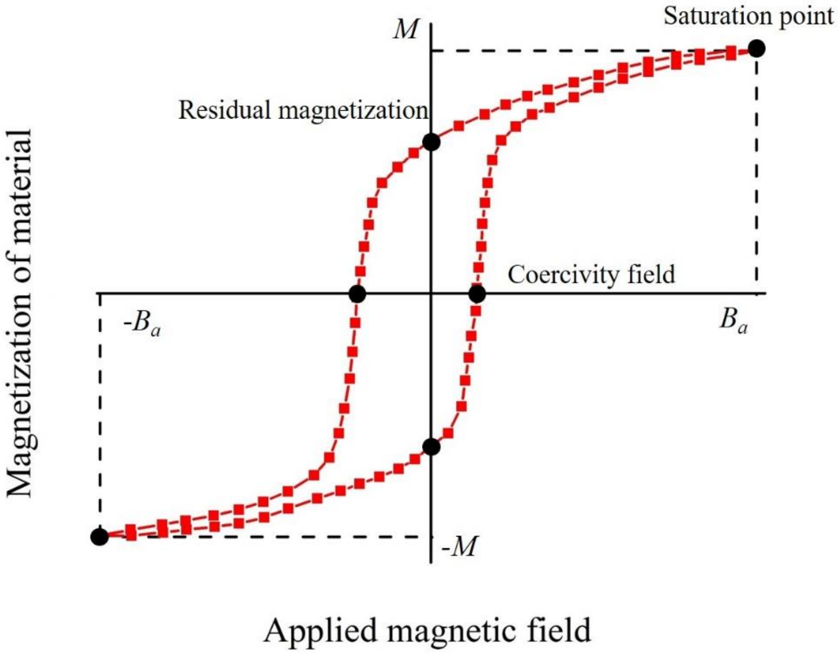

***Figure 2.11** Hysteresis loop shows magnetization properties for ferromagnetic material.*

The coercive field (coercivity) depicted in Figure 2.11 represents the resistance of material to demagnetization (applied magnetic field in the reverse direction), At this point the net flux within the material is zero because the reversed magnetizing force has flipped enough of the domains.

Some ferromagnetic materials, such as iron, nickel, and cobalt, will retain an imposed magnetization indefinitely, even though the magnetizing force is zero (since some magnetic domains remain aligned but some have lost their alignment), so these materials are useful as "permanent magnets". Ferromagnetism occurs below a critical temperature (Curie temperature). Above the Curie temperature, the ferromagnetic spin ordering is lost due to overwhelming thermal activations of the spin system and this material would start behaving as a paramagnet above this temperature.

2.11 Heterostructure coupling and interfacial interactions

Superconductivity and magnetism have antagonistic order parameters, so if these materials are brought into contact, numerous physical phenomena with different length scales can emerge in the entire structure or at their interfaces [90, 91]. Extensive research has been carried out so far on combining high temperature superconductors with ferromagnetic materials, as arguably this system open a new horizon for research and has the potential for future applications. A Superconductor has a spin-singlet state where the electrons in a Cooper pair have opposite spins and momenta (anti-parallel). The magnetic order of a ferromagnet is the spin-triplet state, however, as the spins of electrons are parallel [92]. The magnetic exchange field (stray field) tends to align spins of electrons with defined spin orientation along the field, i.e., spin-singlet state at the interface destroyed by an exchange mechanism. The length scale of singlet Cooper pairs in a ferromagnetic material (ξ_f) is short-range, and it is < 3nm for iron [93-95]. The propagation of pairs in a ferromagnetic material can be extended up to tens of nanometres [96-105], however, with an inhomogeneous magnetic exchange field at the interface, Ψ_{long}, which converts pairs from the singlet to the aligned triplet state [106-109], where $\xi_f = (hD/k_BT_c)^{1/2}$ D and k_B are electron diffusion coefficient and Boltzmann's constant respectively [110]. On the superconductor side of the interface, the stray field penetrates over a distance of less than the coherence length (ξ_s) and acts to break the correlation of superconducting pairs. Therefore, spin polarization of Cooper pairs offers a possibility for spin current with Joule heating and dissipation in the spintronic device minimized. On the other hand, electrons tunnelling across the interface also result in the penetration of non-superconducting electrons into the superconductor layer to a distance on the order of the superconducting coherence length ξ_s, and there is leakage of superconducting pairs into the ferromagnetic material. The superconductor order parameter rapidly decays in an oscillating manner in the ferromagnet, in contrast to non-magnetic materials [92], as indicated on Figure 2.12. The continuity of the order parameter at the interface implies the absence of a potential barrier. Therefore, the superconductivity is more likely to weaken, which is typically associated with deterioration of T_c and J_c over the range of the corresponding proximity effect [92].

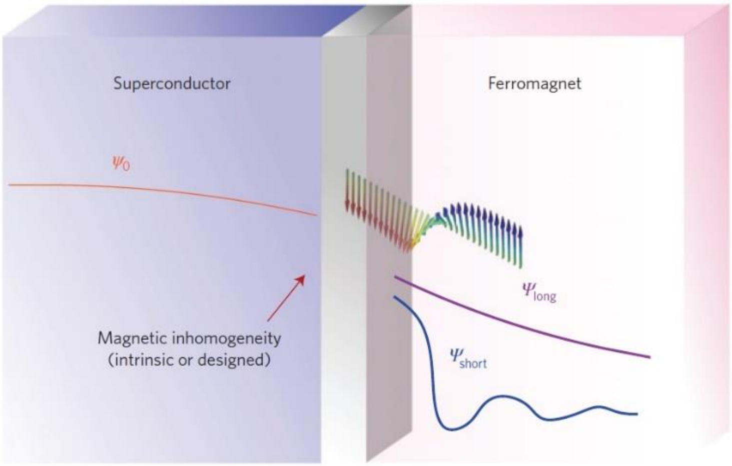

Figure 2.12 *Proximity effect at superconductor/ferromagnet S/F heterostructure , $\Psi_\circ$ is the superconducting order parameter, Ψ_{short} is the triplet-order parameter with short range penetration and decays in an oscillatory manner, while Ψ_{long} is the triplet-order parameter with long range penetration in the presence of magnetic inhomogeneity at the interface [106].*

It has been shown that deterioration of the critical current density occurs as a result of destroying the superconducting correlations induced by YBCO due to the magnetic exchange field, and it depends on the transparency of the interface (since the proximity effect is negligible with a low transparency interface).

Fedoseev *et al.* approximated the interactions between layers in a heterostructured system. An intermediate layer (insulating) was introduced between the ferromagnetic and superconductor thin films to keep both layer properties unaffected [111, 112]. It was found that the proximity effect became negligible on superconductor order parameters for buffer layer thickness > 5 nm.

Manufacturing electronic devices from oxide heterostructure to exploit supercurrent requires keeping the order parameters (T_c and J_c) for the superconductor layer unaffected, and also keeping the superconductor morphology free from any deformities due to deposition process of the ferromagnetic material on top. So, an oxide insulator layer (non-magnetic) should be used as an interstitial layer between these two incompatible materials. Such as $SrTiO_3$ (STO), CeO_2, $PrBa_2Cu_3O_7$ (PBCO), and Pr_2CuO_4 (PCO) for proximity effect suppression. All the insulator layer mentioned above, however, have a certain amount of lattice mismatch with YBCO when they are introduced as a buffer layer between the substrate and the HTS film [113]

In this work, the non-magnetic layer has been used as a cap on thin film superconductors to form heterostructure system, as long as a combination of ferromagnetic material as a buffer layer in heterostructure yield a remarkable effects (much more distorted) in superconducting thin film. While the presence of an interstitial layer at the interface also improves the structure slightly, in contrast to the case where a magnetic layer has been introduced as a capping layer to form a heterostructure (distortion) [114], and more a thin of non-superconducting layer not supporting the current flow at superconductor layer [115].

2.12 Effective flux pinning sites

2.12.1 Defect flux pinning

Generally, the J_c in high temperature superconductors deteriorates rather rapidly as a function of applied magnetic field. The main reason is that, upon increasing the temperature, a thermal activation effect is induced, where vortices may no longer be bound to a certain position (creating the so-called vortex liquid phase) as shown in Figure 2.13. In this phase, the thermal activation energy exceeds the vortex pinning energy [75]. Furthermore, due to the layered structure of high temperature superconductors, the crystal anisotropy is strong, and applying magnetic field parallel to the *c*-axis direction weakens the superconducting characteristics compared to field parallel to the *ab*-plane. Moreover, with increasing magnetic field, the interactions between the vortices become important, and they start to compete for pinning sites and also experience strong vortex-vortex interactions. Therefore, alternative approaches have been adopted where introducing effective artificial pinning sites is required. The intentional incorporation of artificial pinning sites in YBCO film beyond those present normally is a probable route to the ultimate optimization of both self and in-field performance of superconductors.

Introducing, engineering, and controlling the density of artificial pinning sites has a significant impact on improving a superconductor's characteristics. Upon increasing the density of pinning sites in superconducting materials, the vortex lattice order may be destroyed, so that the vortex lattice would evolve into the so-called vortex glass phase, as shown in Figure 2.13 [5, 56].

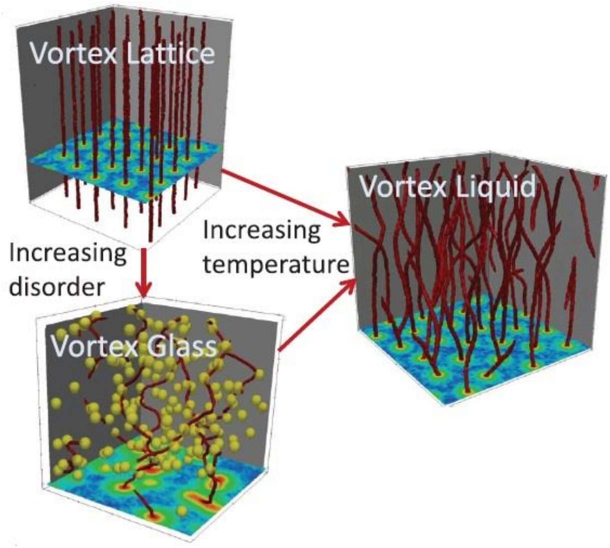

Figure 2.13 *Vortex phases induced by increased temperature and defects in superconductor material [5].*

Thus, how to design and introduce defects is one of the key issues for real-life applications. To date, various techniques have been developed to control defect structures, particularly through the research on high-transition-temperature cuprate superconductor (YBCO) thin films. Irradiating superconductor material with electrons [116], protons [117], fast neutrons [118, 119], and light ions generates randomly distributed defects in atomic or nanometre scale. Columnar defects can be produced by high-energy heavy ion irradiation [120]. Adding defects by irradiation of YBCO thin films, however, achieved only a marginal improvement in J_c [121, 122]. Doping with impurities is one of the routes for introducing pinning sites, such as $BaZrO_3$ nanorods [60], $BaSnO_3$ nanorods[59], and Y_2O_3 nanoparticles [123], which can be included in the superconductor structure during epitaxial growth of YBCO thin film, by multilayering [17, 57, 58]. The results showed that bismuth silicon oxide (BSO) achieved a pinning force (F_p) almost two times larger than that of bismuth doped zinc oxide (BZO), while, J_c for nanoparticles surpassed that of BZO at low temperature, even though they had a J_c value half of that for BZO at 77 K. These defects have to be on the order of superconductor coherence length to result in effective pinning, and this is a significant challenge, as the ξ for HTS is relatively small.

Introducing extrinsic pinning sites has been adopted for YBCO thin films in a bid to enhance their performance in addition to their intrinsic defects. Different extrinsic artificially fabricated pinning sites have been introduced into superconducting thin films. The examples of such artificial defects are perforations in thin films, that is, full or partial perforation throughout the entire thickness of the films [124], substrate engineering [125], magnetic dots [126], or flux pinning induced by the vicinity of magnetic materials to superconductors [127, 128].

Tremendous efforts have been undertaken in introducing and engineering configurations of antidots, where the antidots were utilized as artificial pinning sites. These efforts involved the removal of some amount of superconductor material from certain regions (hollow defects), i.e., the T_c inside the antidots is effectively non-existent. In general, the interactions of vortices with these pinning sites are subject to some geometrical parameters: depth, size, shape, and distribution. The research results have demonstrated that the fully perforated sample has a stronger effect in pinning and guiding the vortices than partially lithographically drilled holes [129, 130]. The effect of the hole density distribution was investigated by Y. L. Wang et al. [131], where a nanoscale conformal arrangement was introduced to the film of MoGe to examine the efficiency of flux pinning at transport measurements. The comparison results with as-grown and triangular counterpart films revealed that the conformal arrangement had a significant impact on avoiding interstitial vortex motion, and it was more pronounced at high magnetic fields, as shown in Figure 2.14 (left), although both conformal and triangular arrays improved their superconducting performance. On the other hand, a random order of antidots leads to degradation in critical current density as compared with a quasiperiodic lattice of pinning sites close to T_c, as indicated in Figure 2.14 (right), which was implemented by M. Kemmler et al. [132] on a niobium thin-film superconductor bridge.

The improvement at I_c in previous cases (conformal and quasiperiodic pinning arrays) was manifested by the appearance of local maxima on the critical current curve, which can be attributed to the commensurability effect between the vortex lattice and the pinning arrays [133, 134]. Arguably, all vortices are trapped at pinning sites, but once the vortices start to emerge at interstitial sites (B_a exceeding the matching field), there is a steep drop in flux pinning. On the other hand, destroying the order of the vortex lattice can be realized by using strong disorder in certain patterns (incommensurate with the Abrikosov triangular lattice), so that a disruption in current flow will occur at lower field.

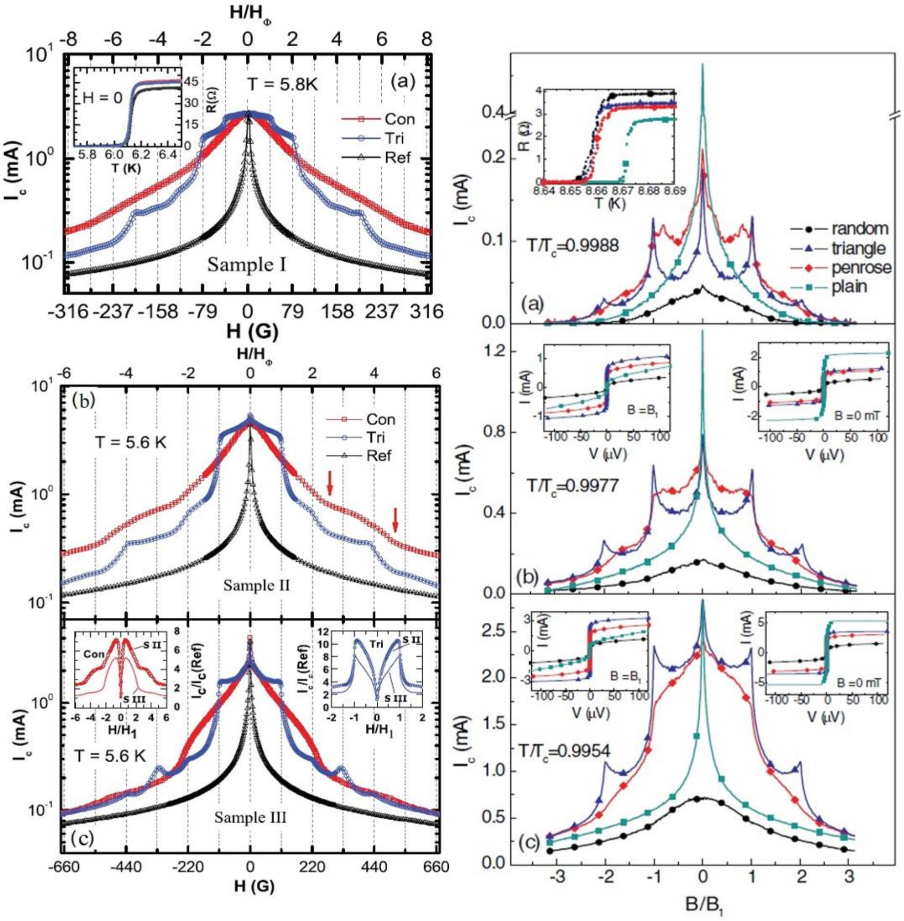

Figure 2.14 *(left) Critical current as a function of magnetic field for conformal and triangular arrays of round antidots and the as-grown film, while sample III has a blind antidots. The densities of holes in Samples II and III are higher than those in sample I [131]. The inset in (a) is R(T) curves for three sections of sample I, and insets in (c) present comparison for the conformal and triangular arrays. (right) Critical current comparison for the samples with different distribution of holes in bridges at given temperatures [132]. The insets in (b) and (c) are current voltage curves for all perforated and plain bridges.*

As mentioned previously, introducing an antidots array into a thin film in a certain manner leads to enhance superconductor performance at high temperature. At low temperature, however, these arrays channel the propagation of flux. Motta et al [135] have addressed this issue. They investigated a graded distribution of pinning site rows and compared them relative to uniform arrays and as grown films. The results revealed that graded pinning sites introduced into MoGe thin film were more effective compared to a uniform distribution. In addition, graded configurations showed resistance to flux channelling and flux avalanche, which are triggered due to thermomagnetic instabilities, and this is manifested by noisy response of the loop at low temperature, as shown in Figure 2.15.

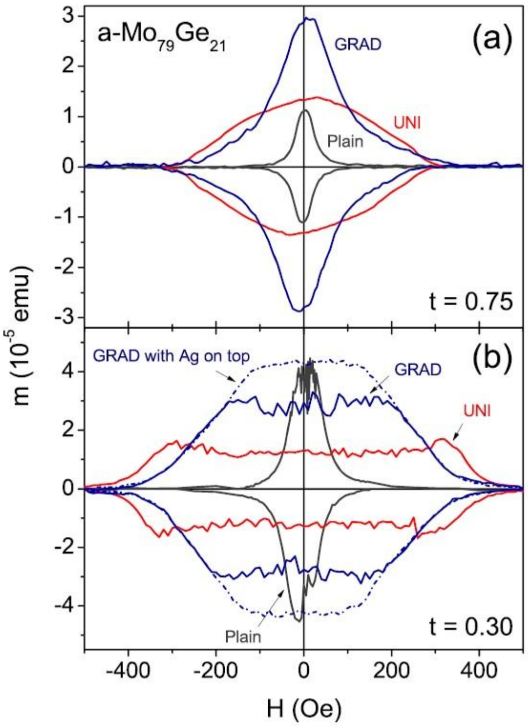

Figure 2.15 *The magnetic moments of three samples, as-grown, and with uniform and graded arrays, at two different temperature. Moreover, the noise responce region for the graded one is less pronounced compared to the uniform one [135].*

It is still unclear whether the improved superconductor performance and reduction of the region showing noisy behaviour (graded sample) came from the lack of perfect periodicity in the antidot lattice or from the gradient itself.

George et al. [136] have undertaken this issue by examining antidot lattices (triangle arrays) with sizes exceeding the penetration depth in arrays with different geometrical arrangements. The antidots were considered as collective pinning sites for magnetic flux, rather than vortices, due to their ability to trap large chunk of flux in the rather larger areas free of superconducting material (antidots) [137]. The study proved that all the samples with a graded distribution of antidot arrays outperformed the arrays with uniform distributions of antidots over broad ranges of applied magnetic field and temperature, as shown in Figure 2.16 (left). They are more effective in flux pinning due to creating a non Bean-like flux profile for vortex penetration.

The hypothesis that non-uniform arrays of antidots suppresses channelling effect at high magnetic field was confirmed by Jones et al. [138], where large-scale triangular arrays with different shapes of antidots were utilized to examine the behaviour of J_c. Triangular arrays have more opportunity to pin interstitial vortices as a consequence of the channelling of vortices between saturated antidots. The results revealed that the sample including large-size antidots showed a reduction in J_c. The smallest size antidots, however, improved flux pinning dramatically at low temperature, where intrinsic pinning is more effective, as it is obvious in Figure 2.16 (right). Manufacturing antidots arrays as pinning sites involves removing a certain amount of superconductor material from specific and controlled locations, thus leading to damage to the superconductor integrity and degrading in its performance. Even with increasing J_c relative to the plain film, the overall critical current (I_c) may still be reduced due to the removal of a relatively large volume of the superconductor. The integrity of superconductor material is proportional to the shape and density of the pattern that was used [139]. Therefore, to address this issue alternative approaches are required.

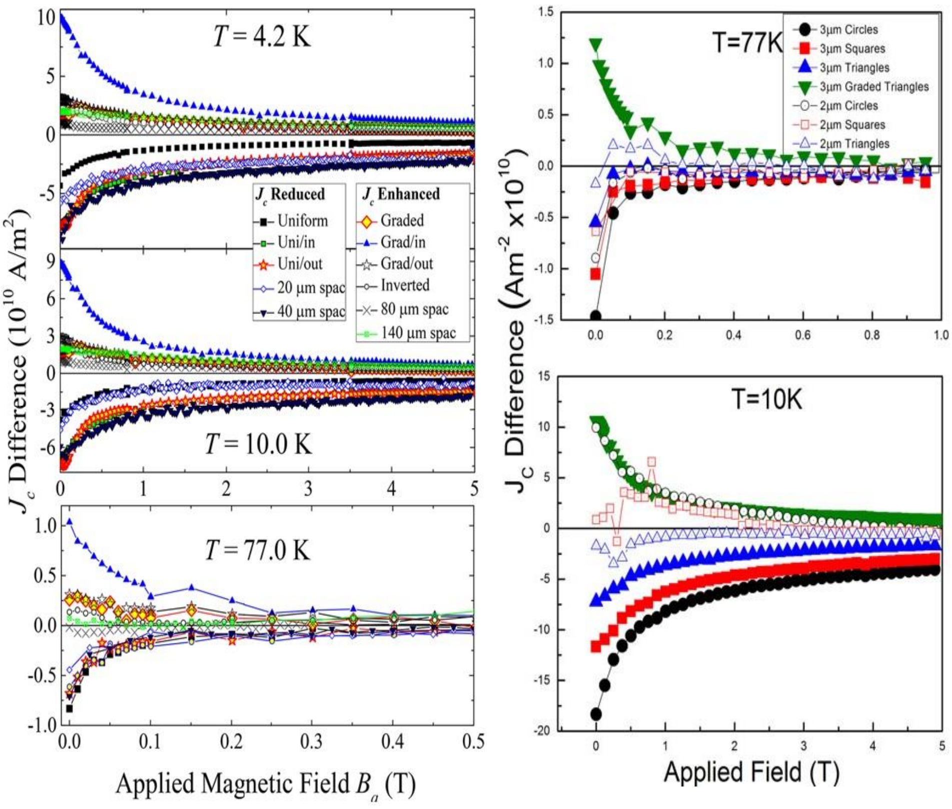

Figure 2.16 *(left) J_c difference between the post- and pre-lithography perforated films with uniform and non-uniform triangular and square arrays [136]. (right) J_c differences as a function of applied magnetic field for various geometric configurations of antidot arrays [138].*

Substrate nano-engineering is considered as a promising technique for flux immobilization, where any enhancement in J_c is accompanied by an increase in I_c. Jones et al. [125] proposed substrate exposure to ion beam etching prior to the deposition of superconducting material, where different patterns were introduced on the substrate for examination purposes. The main point in this study was to ensure that the quality of YBCO film was the same for etched and un-etched regions. The sample with a rounded pattern (hexagonal array of circles) had a higher J_c at low temperature, where enhancement arises due to flux pinning at the edges of the etched pattern rather than the collective pinning effect. In contrast, other patterns (hexagonal array of triangles, squares and graded concentric square rings) exhibited weak pinning due to easy vortex channelling of suppressed superconductivity [131, 140]. Collective pinning in vortex dynamic is more prominent at elevated temperature for patterns, which is clearly seen in Figure 4 in Ref.[125]. Put differently, a non Bean-like uniform gradient in the magnetic flux profile was present for patterns with sharp bends (triangles, squares and square rings), while the symmetric shape of circle provided homogeneous penetration of vortices (creating a vortex state resembling to that in the Bean-model for flux entry[141]).

Artificial defect pinning introduced by non-magnetic pinning sites has less effectiveness in pinning vortices. These defects need to pin the vortex cores and should be comparable to coherence length (ξ) in size to achieve perfect pinning. Furthermore, at elevated temperatures the maximum potential pinning energy, which can be expressed as $U_{cp} \sim \left(\frac{H_c^2}{8\pi}\right)\pi\xi^2 \approx (\frac{\emptyset_\circ}{8\pi\lambda_L})$, where H_c is the thermodynamic critical field, starts to decrease as λ_L increases at high temperatures, thus leading to a weakened pinning effect at high temperature [142]. On the other hand, even when using large-size of defects, the superconductor is more likely to be degraded due to more damage to the thin films integrity.

2.12.2 Magnetic flux pinning

Essentially, producing a high-quality film requires as few processing steps as possible to avoid degradation of any of its properties, which could arise through these manufacturing and handling steps. Moreover, fewer steps would reduce the time and cost of film manufacturing. Therefore, magnetic pinning has been proposed as a promising route to improve YBCO film performance at high temperature, which is more desirable for practical applications [142]. Magnetic pinning sites are characterized by pinning the magnetic flux in a vortex, in contrast to non-magnetic pinning sites. Put differently, magnetic pinning interacts directly with magnetic flux, which, in turn, would produce an anchoring effect for vortices subjected to the Lorentz force, which is able to set vortices into motion. Furthermore, magnetic pinning possesses a robustness at increasing temperature, in contrast to other types of pinning sites. The magnetic pinning energy can be calculated as, $U_{mp} \sim \emptyset_\circ M(x) d_s$ [143]. It is clearly seen from equation that temperature is not a major factor in determining the pinning level. U_{mp} is only dependent on the magnetization of ferromagnetic material together with a certain superconductor layer thickness, d_s. Therefore, magnetic pinning is desirable to overcome the thermal fluctuations that take place at high temperatures. Therefore, flux pinning by domain walls was proposed by Bulaevskii et al. [142], where these systems comprised of nanoscale period of superconductor/ferromagnetic multilayers. They indicate that, as a result of magnetic interaction with the domain structure in the FM layer, strong vortex pinning could be achieved below coercivity field range. This theoretical expectation by Bulaevskii is compatible with the experimental results of Garcia-Santiago et al. [144] and Zhang et al. [145]. A different scheme involved epitaxial growth of FM/SC bilayers composed of YBCO/yttrium stabilised zirconia (YSZ) (buffer)/Ba-orthoferrite and YBCO/$Pr_{0.67}Sr_{0.33}MnO_3$, respectively. The previous systems that had in-plane magnetization showed evidence of enhancement in flux pinning by the domain structure in the FM layer compared to as grown film. Moreover, the flux pinning potential has depend on the thickness of the underlying ferromagnetic layer. The weak perpendicular anisotropy of permalloy (Py) was investigated by D. Mancusi et al. [146], to show the influence of domain strips on vortex pinning in niobium (Nb) superconductor. Thicker Py films led to a reduction in pinning strength, which was attributed to a smaller strip domain density, resulting in a weak interaction between the moving vortices and those pinned at domain walls.

On the other hand, the results indicated that the contribution of SC thickness has less effect on J_c and pinning by the underlying ferromagnetic layer, as shown in Figure 2.17. The superconductor films in FM/SC bilayers are rather sensitive to ferromagnetic epitaxial growth, i.e., whether it is a cup or buffer layer in the system. This issue has been addressed by Mika Malmivirta et al. [114] and Jijie Huang et al [147]. They proved that the optimum design is for the FM to be a cap layer, where magnetic ferrite (nanocomposite layer) is incorporated onto YBCO and iron chalcogenide superconductors, respectively. This effect can be ascribed to the lesser distortion to the superconductor structure when the ferrite on top. Even when there was an extra layer of pure CeO_2 on top of the ferrite buffer layer, there was still much distortion compared to FM as a capping layer. In addition, Malmivirta et al. found that the ferrite deposition temperature has an effect on the magnetic properties of the superconductor. Increasing the deposition temperature led to increases in the coercivity and saturation field, while introducing different sorts of ferrite had less influences on J_c enhancement.

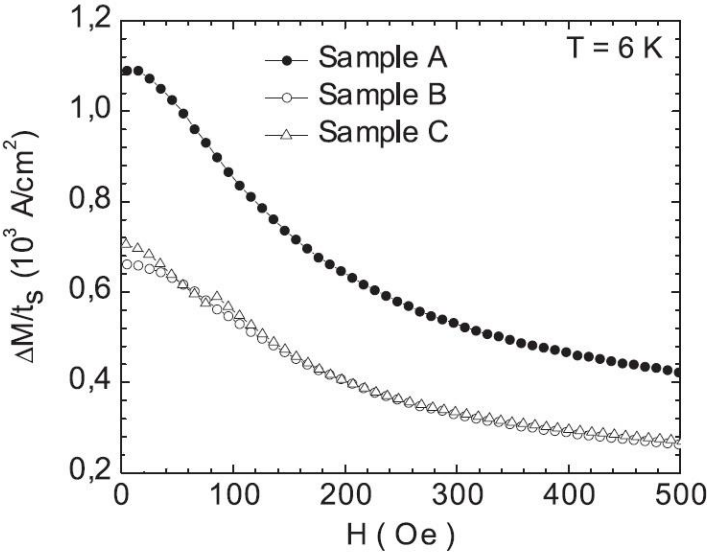

Figure 2.17 *Field dependence of the difference in ΔM normalized to the Nb layer thickness* t_s *at 6 K, for Samples (-•-) A [Py(1.5 μm)/Nb(150 nm)], (-o-) B [Py(2 μm)/Nb(200 nm)] and (-Δ-) C [Py(2 μm)/Nb(120 nm)] [146].*

In addition, the type of the domains (Bloch or Néel) influences the flux pinning in its own way in the structure of FM/SC bilayers. This effect was manifested in the report of E.J. Patiño and M.G. Blamire [148]. They noticed that a sharp drop in magnetization reversal at the coercivity field in structure of Nb/Co was due to the dominance of Bloch domain walls in thicker films, as shown in Figure 2.18 (left). These experiments were compared with one reproduced with a thinner cobalt film. A conventional type II magnetization hysteresis loop was observed, and the influence of the Bloch walls was absent. The reduction in superconductor properties has been confirmed by E. Bhatia et al. [149] in Nb/Ni bilayers with various magnetic film thickness, with nickle having the in-plane magnetization.

Transport measurements showed a suppression in T_c for the superconductors in the T_c-H phase diagram for thicker magnetic films, as shown in Figure 2.18 (right) [149]. The T_c suppression is due to the high intensity of stray field generated by the Bloch domain walls, generating out of-plane vortices that penetrate the thin-film superconductor. These stray fields (vortices) locally affect the superconductivity along the domain walls stripes. The maximum suppression is at the coercive field, where the maximum domain wall density is present. However, this suppression is recovered at the saturation point of magnetization, which implies that domain-wall stray fields are at a minimum (where the magnetic layer behaves as a single domain). The stray field intensity is minimal in the thinner nickle film where, the Néel walls were energetically favourable.

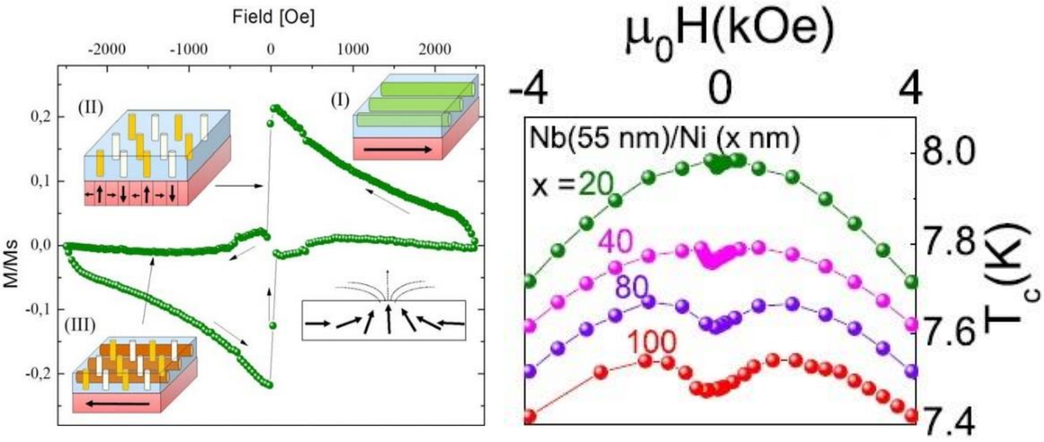

Figure 2.18 *(left) Magnetic moment as a function of transverse applied field for Nb(25nm)/Co (45nm) [148]. (right) H-T phase diagram for heterostructures of Nb with different thicknesses of magnetic layer [149].*

Periodic magnetic pinning arrays structures have been adopted as a fruitful approach to promote pinning phenomena with a well-ordered superconducting vortex lattice. This is because the magnetic character induces stronger pinning effects than nonmagnetic sites by locally suppressing the superconductivity through the magnetic proximity effect and stray fields [150, 151]. Moreover, vortices are more likely to be present in pinning sites in contrast to antidot structure, which affects the pinning status that occurs in the different regimes. This would increase the interaction between the vortex and the pinning centres. Introducing magnetic configurations is unrestricted by size and periodicity conditions on the pinning centres, as in the case of antidots (superconductor integrity), although, size and periodicity might yield different pinning mechanism [152].

As elucidated previously, using magnetic or antidot lattices as pinning sites involves a plethora of physical effects, including, matching effects [153-156], individual and collective flux pinning, or the rectification of flux motion through pinning sites asymmetrical configurations, and channelling effects in vortex lattice motion [134, 157, 158]. Insight into the microscopic origin of magnetic pinning is still lacking, however. In this context, commensurability effects between the vortex lattice and arrays of gold nanoparticles in clusters linked to the superconductor film surface via organic linker molecules has been investigated [159]. Pinning potential has been achieved at temperatures close to T_c and can be observed by a drop in resistance for the Au/organic-linker/Nb architecture, in stark contrast to samples that had metallic islands arrays (Au, Ni) (triangular lattice) directly coupled at the Nb thin film surface. Modification of the thin film magnetoresistance is attributed to a reduction in the local pairing amplitude induced by a process of multiple Andreev reflections [160], where nanoparticles are coupled to the superconductor through organic linker molecules. So, where there is a suppression of Nb order parameters beneath nanoparticles linked via organic molecules, the potential pinning strength is enhanced. Furthermore, the magnetoresistance results pointed to a number of matching effects where the number of pinning sites (dips) was higher than the saturation number. This demonstrated that an additional pinning mechanism for interstitial vortices was present, which was different from the local pairing potential mechanism beneath Au nanoparticles mediated by the organic linkers, which may cause denser pinning of vortex lattices.

The nucleation, annihilation, and channelling of vortices and antivortices, and their interactions with magnetic disks and an external field were studied [18, 161]. Vortex-antivortex pairs are spontaneously induced by arrays of magnetic configurations (out of plane magnetization) in close proximity to a superconducting film. The scanning Hall probe microscopy images in Figure 2.19 show that the vortices sit on top of the disks whereas the antivortices tend to avoid them at zero field, in contrast to the case where the magnetic disk have an in-plane magnetization [162]. These results indicate that the polarity of the applied field (flux lines) plays a significant role in supressing or modulating the superconductor order parameter, where more vortices are present at interstitial positions when the field is antiparallel to the polarity of the magnetic dots and vice versa, as indicated in Figure 2.19 (a and c, respectively). Furthermore, researchers examined the mobility of different vortex species (vortex pinning at magnetic dots and at interstitial locations), they found that interstitial vortices are more susceptible to small excitation by ac field forces than when they are pinned by the magnetic structure.

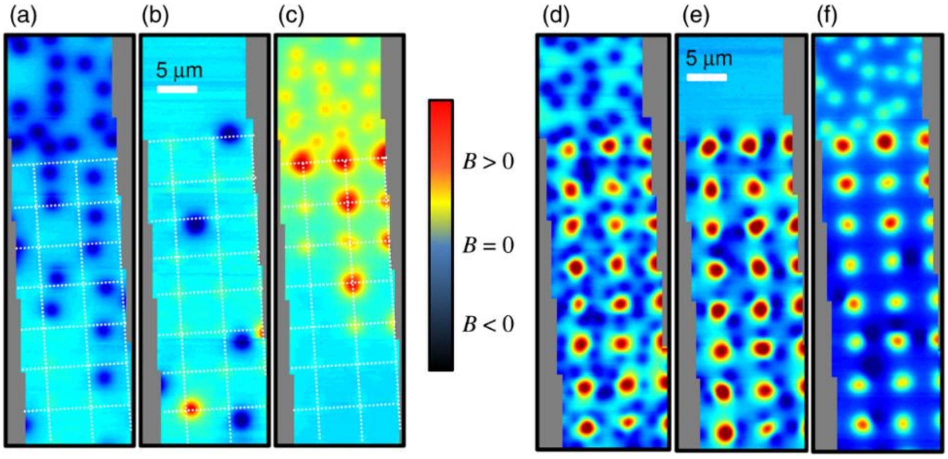

Figure 2.19 *Scanning Hall microscope images taken at $T<T_c$ showing the flux distribution from outside to inside the pattern, as indicated by the dotted lines, (b and e) images of the sample in the demagnetized state with zero applied field. (a, c, d, and f) is the sample after applied field parallel and antiparallel to the polarity of magnetic disks. (d) shows the high density of the vortex lattice at interstitial positions as a result of nucleation and channelling, and (f) the vortex lattice with less density between magnetic dots (annihilation). Dotted lines and their intersections in (a-c) represent the pattern and magnetic dot locations, respectively [161].*

In addition, asymmetric magnetic pinning potentials can be exploited to rectify flux motion, which arise as a result of vortex lattice interactions with asymmetric configurations. The mechanism responsible for vortex rectification is called the ratchet effect, and this phenomenon is useful for many electronic and molecular applications. Such as rectifiers, pumps, switches, or transistors, which enable us to remove undesirable trapped flux and reduce the density of vortices in devices [25, 26]. The ratchet effect requires collective pinning to function. Put differently, interstitial vortices are required to interact with vortices pinned at asymmetric pinning sites, so no ratchet signals are expected when there are no interstitial vortices [163]. Asymmetric pinning potentials can be implemented with many different techniques[164]. Toward that end, numerous studies have been performed, but the majority of studies have been focused on individual vortex effects (low-field) studied in conventional ratchet systems [134].

2.13 Applications of superconductors

The absence of electrical resistivity and their unique magnetic properties make superconductors the materials of choice in a wide range of applications. Applications of superconductors can be divided into two categories: high power applications, using the high current transport capabilities of the superconductor materials, and superconducting electronics, which depend on the quantum properties of the superconductors. Some examples of applications of superconductors are listed below:

SQUIDs:

- SQUID stands for superconducting quantum interference device.
    - It is an ultra-sensitive instrument used to measure very weak magnetic fields on the order of 10^{-15} tesla.
    - SQUIDs can be used to detect the variation of very minute signals in terms of quantum flux.
    - They are useful in the study of earth quakes, removing paramagnetic impurities, and the detection of magnetic signals from the brain and heart [165].
- Superconductors in microwave and radio frequency (RF) devices for filtering the signals in order to improve the performance of communication systems, where using the high temperature superconductors has proven efficiency in network technology [166, 167].
- Superconducting fault-current limiter devices in electric power distribution, where the current flows through the superconductor without any energy loss, but above the superconducting parameters (T_c, J_c and H_{c2}), the abrupt transition to normal state can be exploited to divert the current to a circuit with the desired higher impedance at fault current levels [168].
- Magnetic levitation
    - Because superconducting materials strongly repel an external magnetic field (Meissner effect), this effect is used for magnetic levitation such as in Maglev trains.
- Magnetic resonance imaging (MRI) provides medical researchers with another means of non-destructive visualization of the structure and functions of the human body.

- Additional applications:
    - Computer memory devices
    - Superconducting magnetic energy storage systems (SMESs). In these systems, energy storage in the magnetic field is induced by the flow of direct current in a superconducting coil [168] .
    - Electrical machines [168].
    - Power cables that can be used to transmit electrical power without any voltage drop [168].

- Based on the intrinsic electron spin orientations between superconductors and ferromagnetic materials, interesting phenomena are expected at the interfaces between the SC and the FM. A comprehensive understanding of the interactions at the interface between these two incompatible materials has the potential to pave the way to a new horizons in electronic device applications made from oxide SC/FM systems [169].

Chapter 3

Samples fabrication and characterization

3.1 Chapter outline

This chapter will highlight the experimental procedures used to synthesis thin film superconductor samples, which include substrate preparation prior to the deposition of films followed by the film deposition process by pulsed laser deposition technique, and then applying the desired pattern on it in a cleanroom. Moreover, they will include studying the superconducting thin film properties by measurements of magnetic and transport properties. Laboratory based characterization of the thin film morphology and structure are then discussed.

3.2 Thin film growth technology

Enormous interest has been generated on the fabrication of high-temperature superconductor thin films for advanced microelectronic devices. Different approaches that have been used for thin film synthesis include chemical vapour deposition (CVD) [170], molecular beam epitaxy (MBE), and sputter deposition [171]. On-axis deposition by the pulsed laser ablation (PLD) technique is widely used in the synthesis of high-quality oxide and heterostructured thin films for investigation. Oxide thin film growth is extremely susceptible to the oxygen content [172], i.e. when transferring stoichiometric compounds from the target to the substrate surface, it is essential that this takes places at a particular oxygen pressure for oxidation of the film materials. Moreover, many parameters might affect the properties of high temperature superconductor thin films, some of which are relevant to deposition parameters, while others are associated with substrate selectivity.

3.2.1 Substrates used for thin film growth

Fabrication of high-quality (good morphology and stability over time) thin film superconductors with a remarkable capability of carrying large currents relies on epitaxial growth on their substrates. Different substrates have been utilized for film growth, but each substrate has parameters that might have an effect on the thin film properties, which include the thermal expansion coefficient, dielectric constant, and the degrees of lattice mismatch with the material deposited on it. Table 3-1 shows the main characteristics of common substrates used for YBCO thin film epitaxy [173].

Table 3-1 *Characteristics of the substrates used in this investigation.*

Substrate	Structure/Lattice Constant (Å)	Thermal Expansion $(\times 10^{-6})$/K	Dielectric Constant	Lattice Mismatch to YBCO	M.P. (°C)
$SrTiO_3$	Cubic, a=3.905	10.4	300	0.12%	2080
$LaAlO_3$	Rhombohedral, a=3.790 c=13	9.2	24.5	2.8%	2100
MgO	Cubic, a=4.21	12.8	9.80	7.9%	2852
YSZ	Cubic, a=5.125	10.3	27	31%	~2500

According to Table 3-1, $SrTiO_3$ (STO) has smallest lattice mismatch (so more compatible) with YBCO, giving it superior performance over other types of substrates, and hence STO is most widely used for all cuprate thin film deposition. STO has a higher dielectric constant, however, making it unreasonable to use this type of substrate if the high frequency properties of the deposited superconducting film are important. High-quality of YBCO thin film can be achieved on MgO substrate, which has a lower dielectric constant (but higher mismatch) by optimizing deposition procedure. A thin layer of STO coated on the substrate surface before superconductor film deposition can play a crucial role in the properties of YBCO [174]. The effect of the substrate type on the properties of YBCO has been investigated by Fedoseev [175], by depositing a thin layer of superconductor on STO, $LaAlO_3$ (LAO), yttrium stabilized zirconia (YSZ), and MgO substrate with the same deposition parameters. The results indicate that superconductor thin layers grown on STO substrate achieved a high transition temperature and lowest transition width, as obviously shown in Figure 3.1 [175]. Moreover, a superconductor thin layers grown on YSZ substrate showed good enough superconducting properties after introducing a buffer thin layer of STO prior to superconductor layer deposition, even though YSZ has a higher lattice mismatch with YBCO, which makes it promising for future high frequency applications.

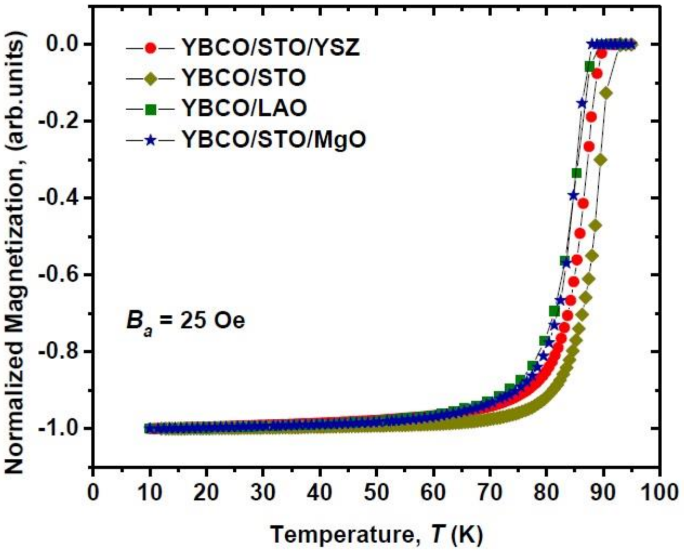

Figure 3.1 *Normalized magnetization as a function of temperature for YBCO thin films grown on different types of substrate [175].*

3.2.2 Pulsed laser deposition technique

Pulsed laser deposition has attracted a dramatic interest since it was utilized for the growth of high temperature superconductors in 1987. In addition, due to its characteristics, with very stable stoichiometry, low contamination level, high growth rate, and easy control of oxygen pressure, temperature, and number of laser pulses, it is more widely used in thin film growth than other techniques. The principle of pulsed laser deposition (type of physical vapour deposition, PVD) is based on using a high power focused pulsed laser beam to strike and evaporate a small amount of material to be deposited from the surface of a target. Evaporated material is ejected from the target (in an ultra-high vacuum chamber or under a wide range of ambient pressures and gas species) in a forward-directed plume to condense on the surface of the heated substrate, which is kept a few centimetres away from the target [176].

The deposition system can be characterized as shown in Figure 3.2: (a) schematic diagram [177], (b) and (c) LabVIEW images of PLD system.

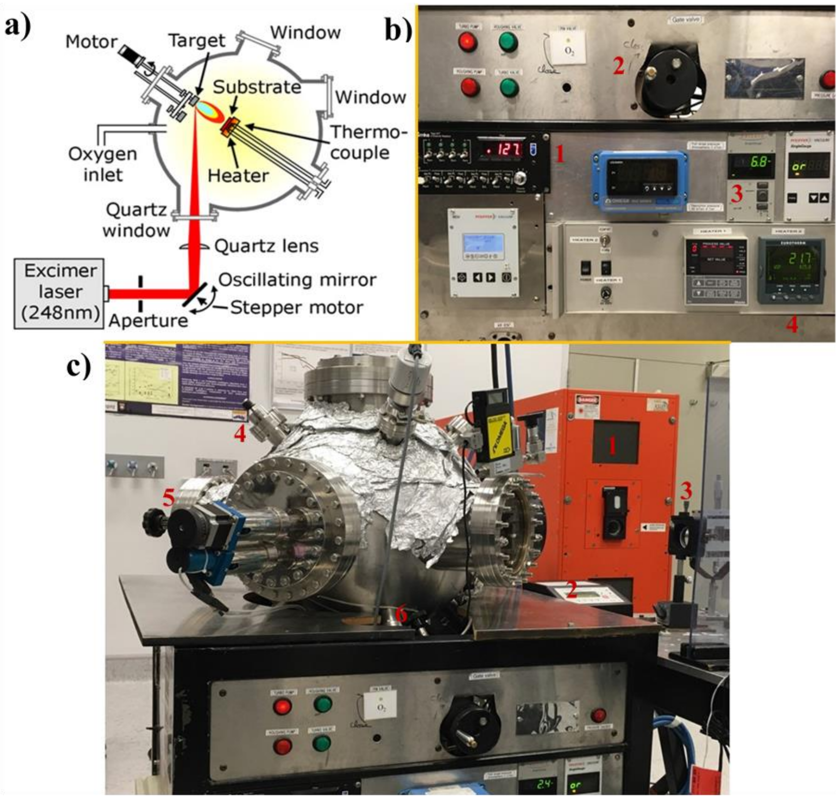

Figure 3.2 *a) Schematic diagram of pulsed laser deposition system [175, 177]. b) Front panel with controls of deposition parameter: 1) Flow control of oxygen gas. 2) Gate valve for turbo pump, 3) Vacuum chamber gauges, 4) gauge for monitoring substrate temperature. c) LabVIEW image of PLD system: 1) excimer Laser source, 2) target carousel, 3) lens for guiding laser beam, 4) shutter between substrate and target, 5) motor for target rotation, 6) Swagelock valve to fill chamber with gas.*

An KrF excimer laser (or 4-th harmonic of a Nd:YAG laser) provides the laser pulses with high power density and wave length 284 nm, pulse duration τ = 25 ns, and repetition rate f = 1-10 Hz. A set of optical components is used to focus and raster the laser beam over the target surface. The main parts of chamber include a substrate holder, where the substrate is placed on a heating platform connected to a power source with a thermocouple for controlling substrate temperature when warming up and cooling down Figure 3.3.

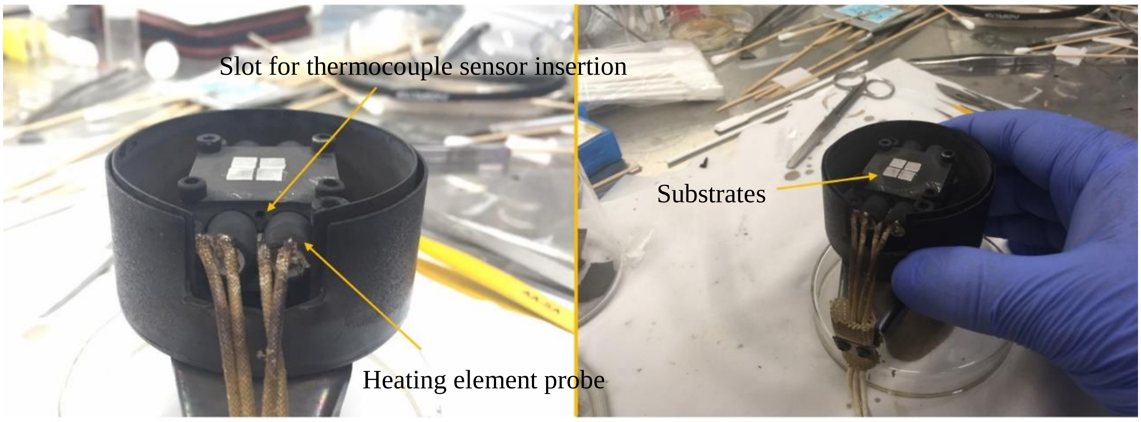

Figure 3.3 *substrate holder with precise temperature control at pulsed laser deposition system*

Moreover, the deposition chamber includes a holder for the material target, which can hold more than one and thus give an opportunity for multilayer thin film growth of different materials without the need to break vacuum when changing between target materials. Furthermore, the material target holder is connected to a motor for rotation of the target to make sure that the target material is consumed gradually and homogeneously. The valve and flow controller, as shown in Figure 3.2(b and c), are used for pumping gas into the chamber. Some deposition processes can be carried out in the presence of a particular gas that is used to build up the composition of films such as YBCO. An oxygen atmosphere is required because this gas is needed for epitaxial growth to form thin films of tetragonal YBCO superconducting phase. For all oxide-superconducting films, oxygen is the most common background gas. So, controlling the oxygen pressure in the chamber during the deposition process plays a significant role [178], and thus, the oxygen composition in the structure of the YBCO thin film can be tuned more precisely, as shown in Figure 3.4 for different ambient oxygen pressures in the YBCO thin film deposition process [179].

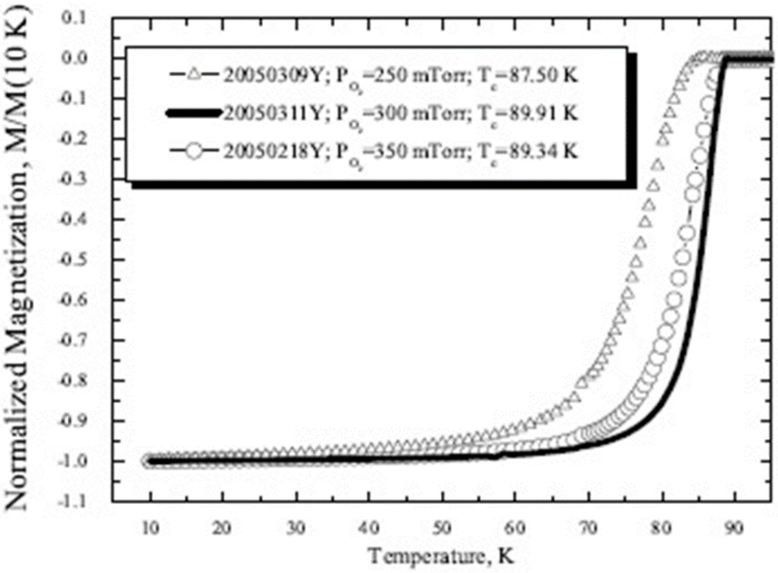

Figure 3.4 *Normalized magnetization as a function of oxygen pressure in the YBCO thin film deposition process [179].*

Moreover, the substrate temperature and target-substrate distance parameters have been investigated and optimized, which have an influence on the grain orientation and surface morphology (roughness), and thus on thin film properties [180] [175] [181].

In this context, manufacturing all thin-film superconductor samples has been implemented on (100) single crystal substrates varied between $SrTiO_3$, Al_2O_3, and MgO purchased from Hefei Kejing Materials Technology Co., LTD., China in different sizes. Each sample was mounted on a sample holder. It was glued gently (to make sure not to leave any scratches or patches on the sample surface) using aqueous conductive liquid silver, and then the holder was installed inside the vacuum chamber. The next steps included pumping out the vacuum chamber down to 10^{-6} Torr, heating up the substrate to 780°C (at which the highest J_c(0,77 K) is obtained), and then filling the vacuum chamber with around 300 mTorr oxygen pressure. As mentioned before, a KrF laser excimer was used with laser energy around 456-474 mJ and laser frequency of 5 Hz for all YBCO deposition.

The film thickness can be adjusted by controlling the time of deposition and the repetition rate, which it is usually ranges between 150-400 nm (while keep rest of deposition parameters constant) [182]. The target-substrate distance was kept fixed during the deposition process at 75 mm (at which the position of the substrate is on the edge of the plume). In contrast, when the substrate is placed within or beyond the plume, it results in degradation of the transport properties.

In-situ deposition was carried out for CeO_2 as an intermediate layer under different deposition conditions, with background oxygen pressure of 150 mTorr and laser repetition rate of 2 Hz, with material target-substrate distance tuned according to the plume produced by the CeO_2 material. The reasons for introducing an intermediate layer are to make sure that mutual magnetic interaction is dominant between F and S rather than electrical interaction, and to prohibit the proximity effect between antagonistic layers. In addition, it is also to reduce lattice mismatch and minimize chemical reactions with the YBCO layer. This is what characterizes the CeO_2 as a buffer layer, making it more favourable for growth upon the superconductor film [183].

Subsequently, post-deposition annealing was conducted on the specimens in oxygen atmosphere (high pressure) for roughly one hour in 400°C in order to improve their crystalline quality, surface roughness, and to promote a transition from the tetragonal to the superconducting orthorhombic phase, and then the sample was cooled down to room temperature.

3.2.3 Laser lithography for introducing patterns

Pre-exposing the film to a laser for a pattern, a few steps need to be applied. These include cleaning the sample by sonicating in acetone for a minute or less. A Branson 2510 ultrasonic sonicator bath was used for this purpose. The sample was then washed with ethanol and blown dry with nitrogen gas for drying and to also make sure that there was no dust on sample surface. A positive-tone photoresist (weakened when exposed to ultraviolet (UV) light and dissolved in a certain chemical solvent in contrast to negative-tone photoresist) was applied for coating the sample surface by using a spin-coater device with a certain rotational speed and time to spread the photoresist material [184], producing a layer with a thickness of roughly 1μm, as indicated in schematic diagram Figure 3.5 (apparatus is shown in Figure 3.6). A pre-exposure baking was carried out on the sample on a hot plate for exactly 1 min at 115°C for partial solidification purposes. At this stage, the sample is ready for exposure to the laser. The samples were exposed to a UV laser to activate areas of photoresist using a Heidelberg pg101 Micro Pattern

Generator after the pattern was created by a layout Editor using a Crystallographic Information File (CIF). The laser parameters were 10 mW at 100% and an energy factor of x2. The sample is centred onto the small hole on the laser lithography stage, and a suction was applied to the back of sample by a small vacuum pump to hold it in place while the stage was moved in a transverse direction. Subsequently, the design has been loaded from a computer into the system. The UV laser will weaken any shaded area in the design (pattern) and vice versa when an inverse option is activated (see Figure 3.5 for the system). Afterwards, the sample was post-baked again for 1 min at 125°C, immersed in MF^{TM}-26A developer and sonicated briefly, followed by a quick washing with distilled water to stop the development process and blow drying. A schematic diagram in Figure 3.6 shows the processes through which the sample passes, starting from growth up to acquiring the desired pattern.

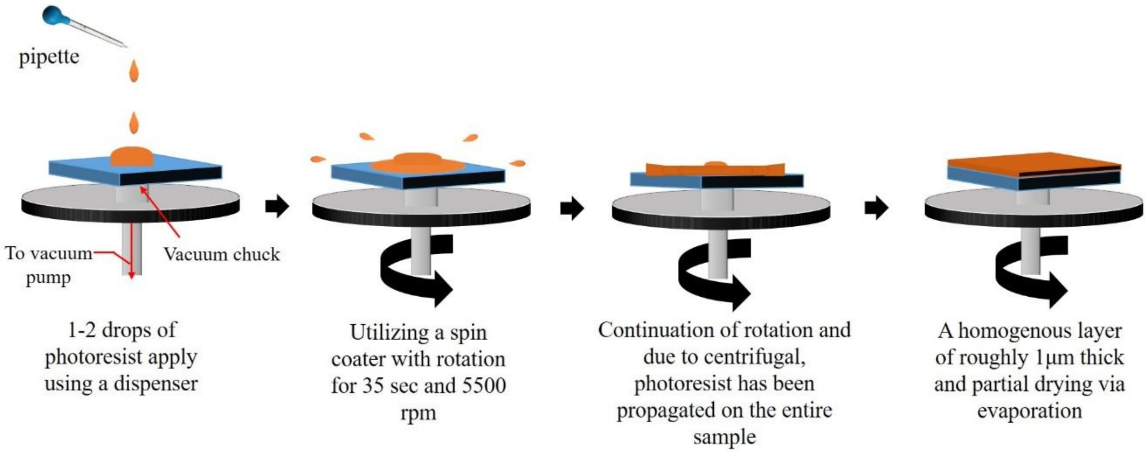

Figure 3.5 *Schematic diagram of the thin film coating process.*

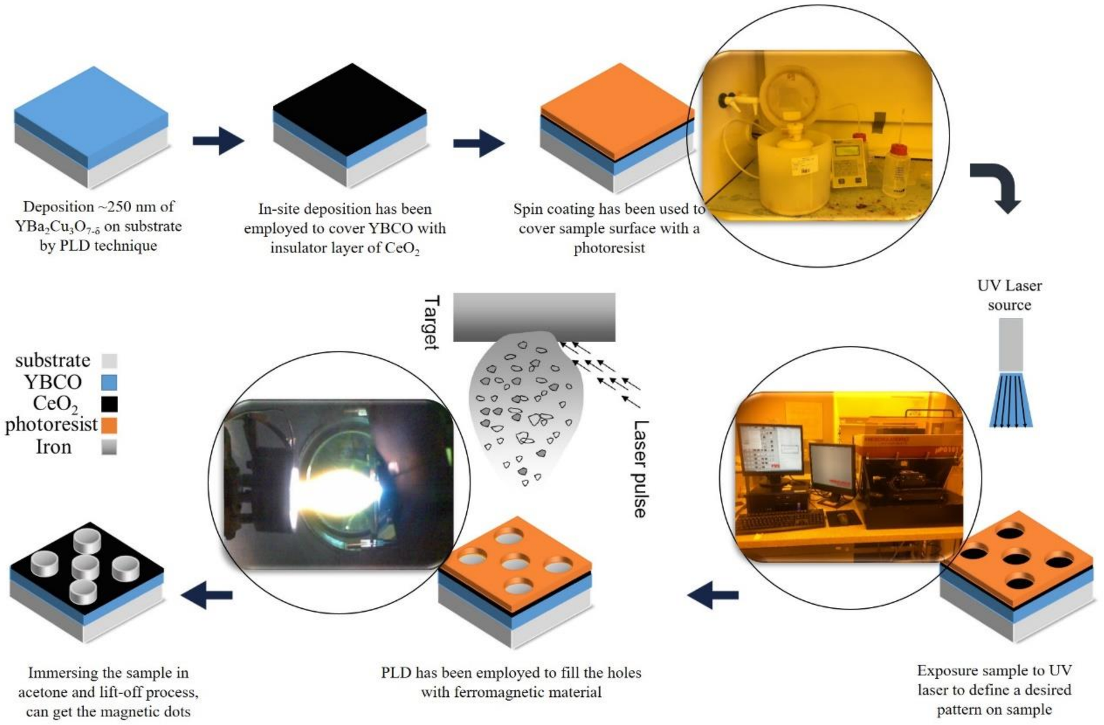

Figure 3.6 *Schematic diagram of the thin film manufacturing and pattering processes.*

3.2.4 Manufacturing a circuit by etching

Etching includes applying and removing process for certain material from the substrate surface with a suitably patterned mask for microfabrication. Different approaches have been used for etching material. One is by a liquid method (wet etching), which includes immersing the sample in a chemical solution to dissolve the un-coated material. Chemical etching is less precise, however, as in general, it is isotropic in direction, as indicated in Figure 3.7, and even with a mask present, chemical solutions can penetrate underneath the mask (producing sloped sidewalls), thus leading to degradation in the properties of the thin film. Moreover, wet etching is not safe, since it requires disposing of hazardous chemicals, so wet chemical etching was a less desirable technique for removing YBCO material in this project. An alternative way of etching samples is by using plasma etching (dry etching).

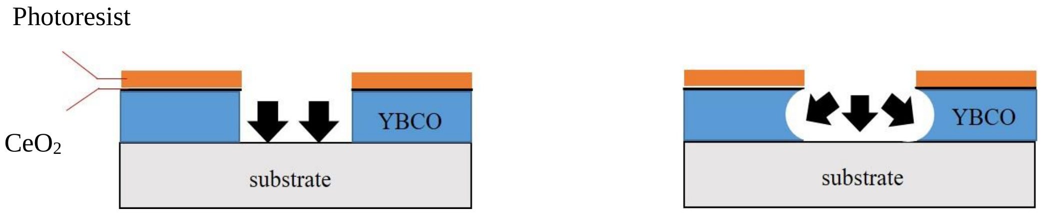

Dry Etching

Directionally asymmetric where etching in vertical direction >> horizontal one causes straight side wall

Chemical Etching

Directionally symmetric where etching in vertical direction work horizontally as well, undesirable for etching

Figure 3.7 *The differences between chemical vs. dry etching, and the influence of each of them on the material to be removed.*

3.2.4.1 Ion-beam etching (sputter etching)

Ion-beam etching (IBE), as shown in Figure 3.8, is one of the most versatile and productive technique, because it is capable of defining surface features down to nanoscale. It is characterized by high precision (highly anisotropic vertically and horizontally), especially valuable for the electronics industry, which demands exacting profile control and for the etching process to be repeatable for production applications. According to these features, samples were exposed to plasma to produce thin film wires for transport measurements, as these measurements required specific wire dimensions determined by the value of the alternating current (AC).

The ion-beam chamber initially is pumped down to below 2×10^{-6} mbar. A plasma is established when ultra-high purity atoms of argon gas are injected into the vacuum chamber of the ion beam etching apparatus and ionized via collisions with electrons emitted from the cathode filament and collected by the anode. The electrons are accelerated by applying magnetic field from a radio frequency (RF) supply to increase the probability of ionization. The Ar^+ ions form a conductive gas or plasma, and these ions are accelerated by a negative grid, so that a beam of Ar^+ ions are formed 12.7 cm in diameter directed towards the substrate that placed on a metal plate for etching, as shown in the schematic drawing in Figure 3.8 [185]. In this work, the settings used to control the current (ion density), voltage (accelerate the ions) and power (ion energy) were 22 mA, 350 V, and 118W respectively. According to these parameters, 250 nm of YBCO and ~10 nm of CeO_2 are completely removed after 45-50 min to obtain the intended pattern.

Moreover, bombardment of YBCO samples with Ar^+ ions will be particularly susceptible to increase the temperature. The sample stage (metal plate) was cooled down by using liquid nitrogen to lower the sample temperature. Sample overheating might cause a distortion of the photoresist and thus affect the quality of the etched sample. In addition, YBCO samples that are heated in a vacuum chamber are more likely to lose oxygen from their structure, which leads to a significant changes in thin film properties [186]. The argon partial pressure in vacuum chamber was kept at 10^{-4} mbar during etching to reduce the collisions of Ar^+ ions with other particles, and consistent etching of the whole sample surface was achieved, as well as minimizing sample contamination. Afterwards, the sample was left in the chamber for cooling down slowly to avoid any condensation as YBCO superconductor is very sensitive to moisture.

Following that, a different pattern was applied, following the same procedures of laser lithography and ion beam etching to remove the CeO_2 from the pads of the sample, and then a layer of gold was deposited on the sample pads.

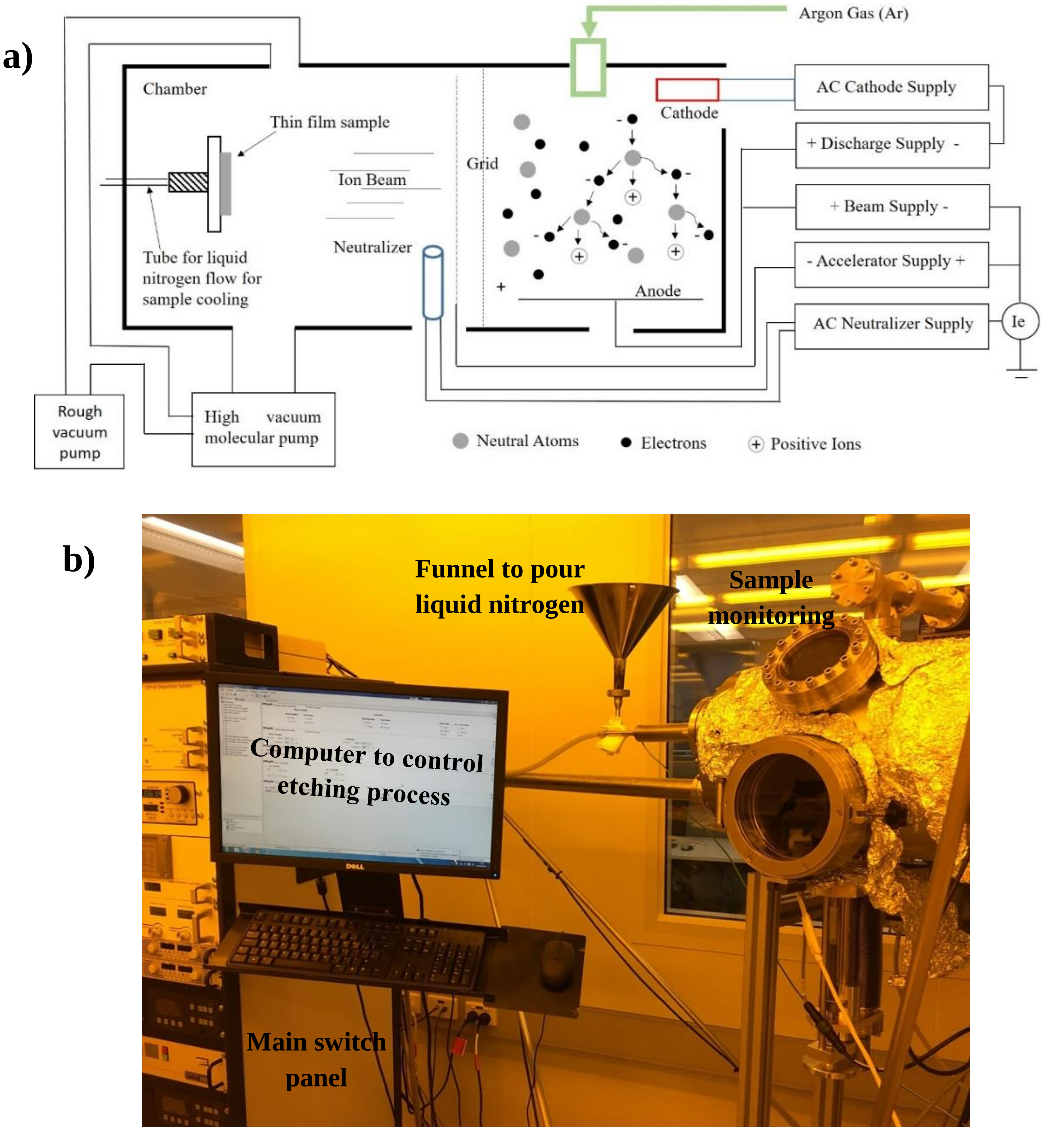

***Figure 3.8** a) Schematic diagram of the ion beam etching system [185], b) LabVIEW image of ion-beam etching apparatus.*

3.3 Thin film characterization

3.3.1 Magnetic characterization

The critical transition temperature (T_c) and critical current density (J_c) are the main characteristics for superconductor thin films. They are estimated either by direct or indirect magnetic measurement approaches, conducted either on a magnetic properties measurement system (MPMS) or a physical properties measurements system (PPMS) from Quantum Design. The main superconducting components included in the MPMS are:

- Superconducting magnet coil wound in a solenoidal configuration, for producing magnetic field.
- A superconducting detection coil which can electromagnetically couple with the sample.
- A superconducting quantum interface device (SQUID), which is connected to the detection coil.
- A superconducting magnet for shielding the SQUID.

The Quantum Design MPMS utilizes a SQUID magnetometer because it is an extremely sensitive device for measuring the variations in the output voltage corresponding to current variation at the detection coil as the sample moves up and down through it. The SQUID is noise sensitive, however, so a superconducting shield is provided for shielding it from fluctuations in the magnetic field.

The SQUID is a superconductor application comprising a superconducting loop with two Josephson junctions, as indicated in Figure 3.9 (b), connected by superconducting wires to a highly conductive coil (detection coil). These components are typically located within a cryogenic chamber, which is cooled by liquid helium and nitrogen.

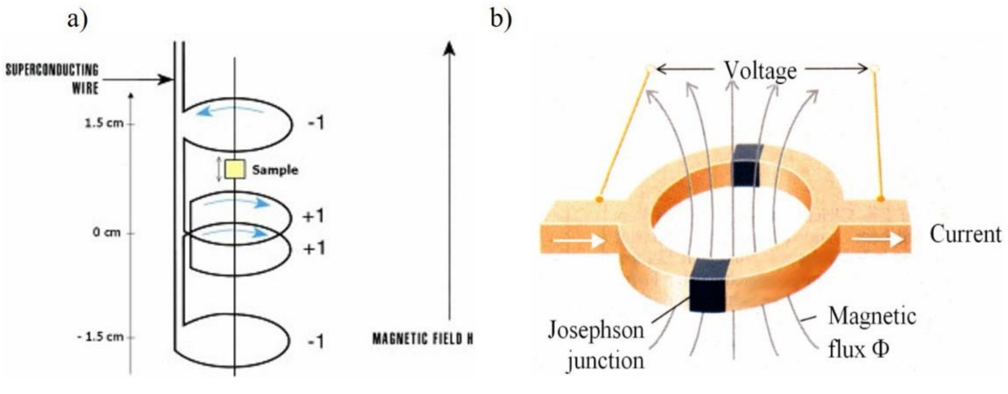

Figure 3.9 *Superconducting components in the MPMS: a) a pick-up coil, b) superconducting quantum interface sensor [187].*

The superconducting detection coil is wound in a set of three coils: the top and bottom ones consist of single turns wound in an anti-clockwise direction, while the coil in the centre consists of two turns wound in a clockwise direction, as shown in Figure 3.9 (a). These coils are located in the centre of the superconducting magnet outside the sample chamber. When the sample moves up and down inside the detection pick-up coil, it produces a change in the magnetic field, and because the sample is coupled inductively to the coils, an electrical current pass through the detection coils. A change in the magnetic flux occurs due to a change in the electrical current in detection coil, resulting in a variation in the SQUID voltage output (functions as a magnetic flux-voltage converter), and this voltage is proportional to the magnetic moment of the sample. Voltage signals are relayed to a monitoring device, which produces a topographical map of the magnetic impulses resulting from the specimen [187]. On the other hand, the PPMS apparatus, as shown in Figure 3.10 is not equipped with a SQUID for detecting signals of the changing magnetic moment, since the voltage signal induced in pickup-coilset (detection coil) as a result of sample vibration is amplified and synchronized in the vibrating sample magnetometer (VSM) detection module. The VSM detection module uses an encoder signal for determining the sample’s vertical position relative to the coil, which is obtained from the VSM motor module (functions as interpreter for raw encoder signals coming from VSM the linear motor transport). The signals of amplified voltage encoded for position are averaged and sent to the VSM application running on the PC as clearly shown in Figure 3.10, which illustrates the principle of the vibrating sample magnetometer [188].

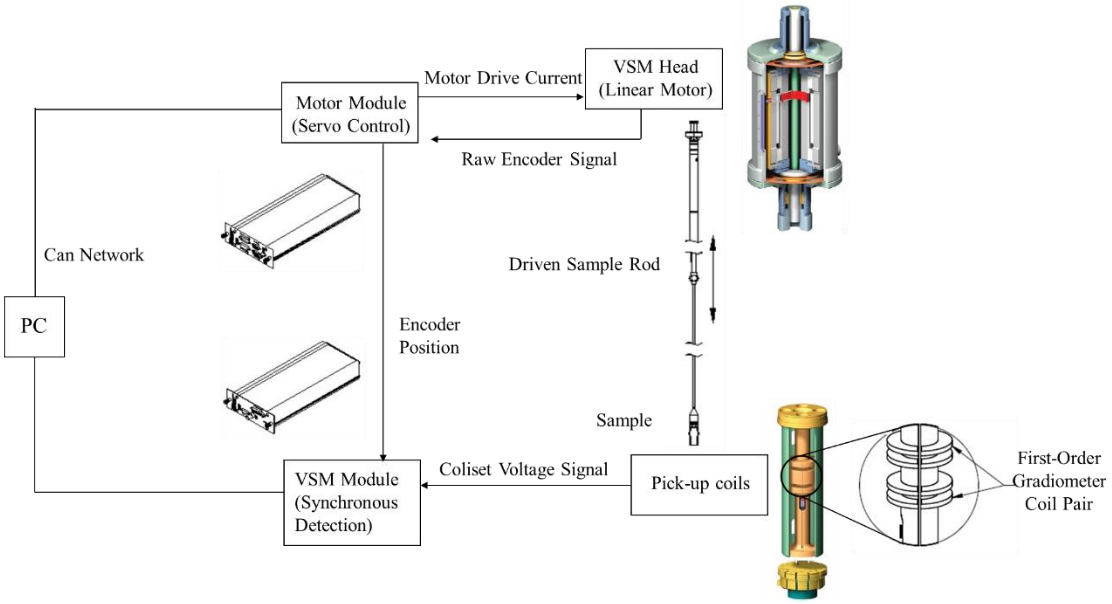

Figure 3.10 *Operating principle of the VSM option. The centre of the first-order gradiometer coils (pick-up coils), as shown in the schematic illustration, corresponds to the centre position of the PPMS with high homogeneity of the magnetic field [188]*

3.3.1.1 Critical temperature measurements

The onset of diamagnetism is defined by the critical temperature T_c, where the superconductor starts to show an impedance to penetrating magnetic fluxes by inducing an opposite magnetic moment when a weak external magnetic field is applied. This impedance starts to increase when the sample is further cooled to reach its peak at T_c-offset (complete diamagnetic signal). In contrast, the impedance starts to decay when the sample is warmed up to the point where the magnetic flux penetrates the sample, and it vanishes above the T_c, so that the magnetic moment for the sample becomes zero.

Magnetic transition measurements were conducted in this work via the MPMS and PPMS devices and revealed the superconducting transition temperature (T_c) and transition width (ΔT) for these samples, which were used to assess the quality of films.

These devices allow measurement of the magnetic moment of a sample and its variations as the temperature increases from below to above T_c, where the samples were zero-field cooled (ZFC) down to 10 K with no applied magnetic field (ZFC). Then a weak magnetic field (0.005-0.01 T) was applied, and the samples were warmed up by increasing the temperature progressively from 10 to 95 K. Proximate to T_c, the samples started to transition from the superconducting to the normal state (i.e., from negative magnetic moment values to zero), as indicated in Figure 3.11.

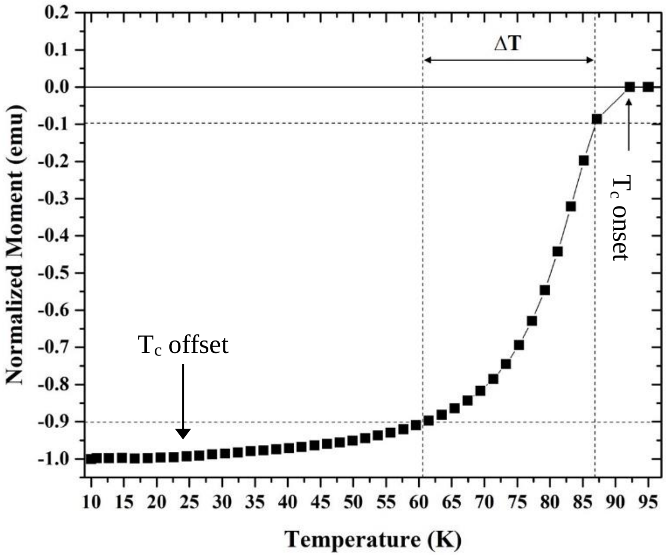

Figure 3.11 *Normalized magnetic moment as a function of temperature to extract the value of critical temperature and the transition width.*

Moreover, the value of the transition width ΔT was extracted from the magnetic moment curve as a function of temperature as well, which represents the difference between two temperatures, as shown in Figure 3.11 (dotted lines on the temperature scale), with the magnetic moment being normalized to eliminate the influence of differences in thickness and demagnetization factors.

It is also worth noting that the broadness of ΔT_c is because M-T measurement was conducted by applying B_a = 2.5 mT, which is required for magnetization measurements.

3.3.1.2 Critical current density estimation by DC magnetization loop

The critical current density J_c is defined as capability of the superconductor to carry a certain amount of current, while above it, the superconductor goes into the resistive state. As mentioned before, it is considered one of the most significant characteristics for thin film superconductors and can be estimated by measuring the magnetic moment as a function of applied magnetic field (hysteresis loop), as shown in Figure 3.12 at varying temperatures for studying their influence on the behaviour of the critical current density.

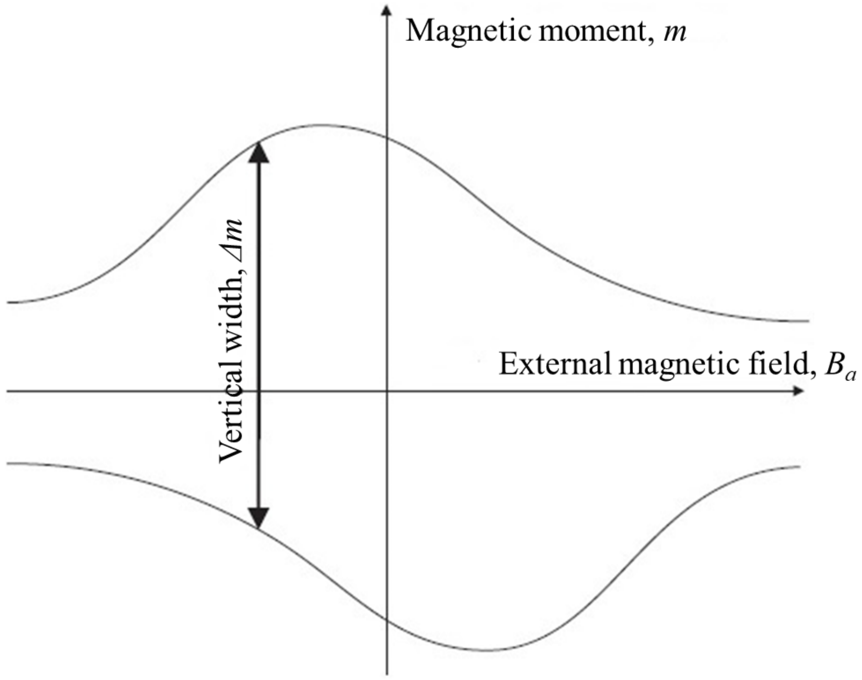

Figure 3.12 *Magnetic moment as a function of applied magnetic field. Note that the field has been applied perpendicular to the sample surface [179].*

The vertical width extracted from the hysteresis loop (Δm) is used to calculate the J_c based on the critical state model between the critical current density and the magnetization [74, 141].

In this model:

$$J_c = \frac{2\Delta M}{\left[W_p\left(1 - \frac{W_p}{3L_p}\right)\right]}\ , \qquad 3.1$$

where ΔM is defined as the quantity of magnetic moment per unit volume:

$$\Delta M = \frac{\Delta m}{V}\ . \qquad 3.2$$

W_p and L_p correspond to the width and length dimensions of the rectangular sample, respectively. If the sample is square then $W_p = L_p$, and the critical current density:

$$J_c = \frac{3\Delta M}{W_p} \qquad 3.3$$

3.3.1.3 Transport measurements

Direct measurements of the critical current and critical temperature are implemented by the electrical transport option (ETO) and the resistivity option provided by the PPMS, where the current is directly injected into superconductor sample. A specific design has been introduced due to the limited current applied to the sample in this option. For this reason, a series of processes: including spin-coating, laser lithography, lift-off and ion beam etching, were used for producing a superconductor wire with width and length (space between voltage contacts) of 30 and 150 μm respectively, for the four-point probe technique. Then, the sample has been installed in the puck provided with two channels (which each have two current and voltage contacts). Allowing measurement of more than one sample at the same time. Four gold wires were used to connect between the pads and the channel contacts, as indicated in Figure 3.13, where the outer contacts were used to deliver the current through the bridge, while the two inner were for measuring voltages.

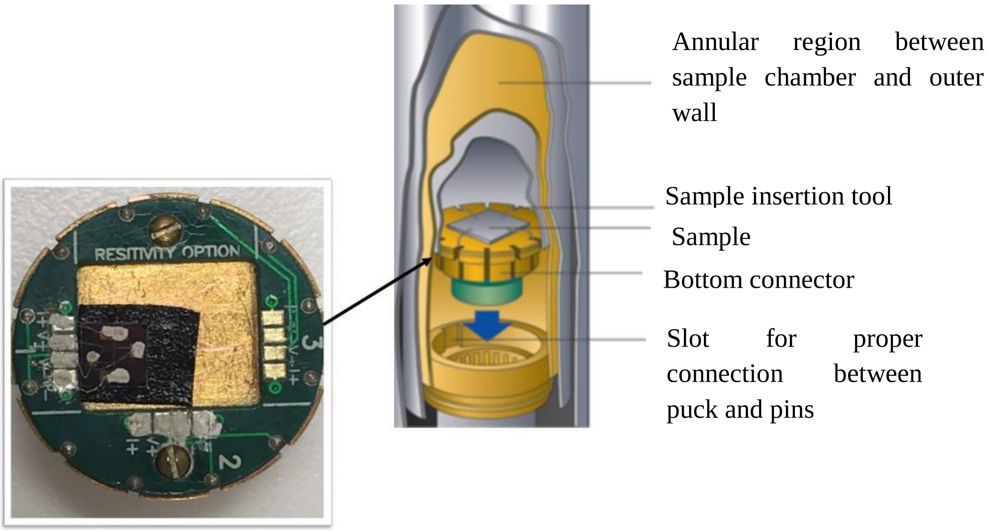

Figure 3.13 *Image (left) of DC transport puck showing the channels and specimen installed in the centre, and schematic illustration (right) of using the four-probe point technique to connect bridge pads with channels by gold wire and puck connection inside the vacuum chamber.*

As mentioned before, the resistivity option is characterized by its ability to provide direct measurements of the critical temperature T_c. A DC current is applied (100μA) through the bridge for measuring the resistivity as a function of temperature from the normal state (above T_c) down to its superconducting state (less than T_c). Furthermore, for studying the behaviour of the resistivity, varying magnetic fields are applied parallel to the *c*-direction, where the transition curve from the superconducting state to the resistive state either hase a sharper transition in low fields or a wider transition in higher fields, as exhibited in Figure 3.14.

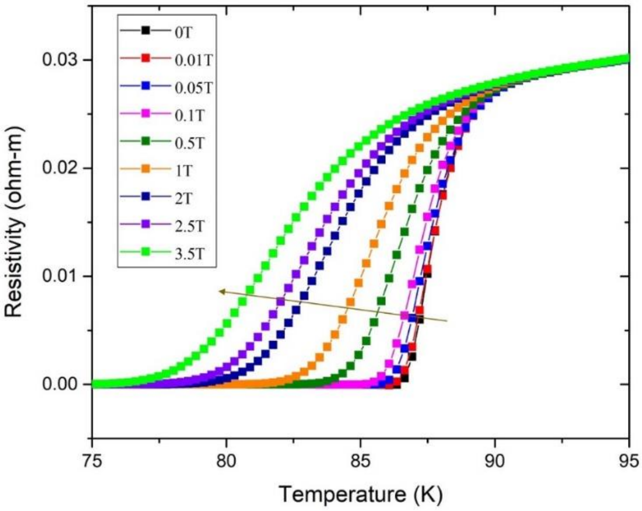

Figure 3.14 *Resistivity as a function of temperature in resistance mode, the arrow showing the direction of increasing applied magnetic field.*

In addition, the critical current (I_c) has been measured by using *I-V* mode in the ETO option, where transport measurements are implemented by the four-point probe method. When a DC current of (0.1A) is injected across a superconducting bridge, the potential voltage difference across the sample is measured in the superconducting state relative to varying either the applied magnetic field or the temperature. The value of the current at which the superconducting wire is no longer carrying a current without energy dissipation (resistance) is taken as I_c, where the voltage between inner contacts increases above the criterion value of 10^{-6} V. Then, the critical current density J_c was determined by dividing the critical current value I_c by the cross-sectional area of the film (S).

$$J_c = \frac{I_c}{S} \qquad 3.4$$

The current was reversed in the superconducting wire for studying some phenomena such as rectification flux motion and the same *I-V* measurements were performed.

3.3.2 Morphology Characterization

3.3.2.1 Transmission electron microscopy

Transmission electron microscopy (TEM) is one of the most powerful techniques in materials science. It provide analytical information on specimens such as the morphology, crystal structure, interfaces, and chemical composition on the nanometre scale and has been widely used for the characterization of materials and devices. In order to obtain accurate and precise information using TEM studies, however, specimens have to be very thin for transferring the highly accelerated electrons and require clean and smooth surfaces in the analysis region. The basic principle is similar to that of the light microscope, but TEM uses an electron bundle as an alternative source of illumination since the electron wave length is much shorter than those of light. The beam of electrons emitted from electron gun is focused into a small spot by a condenser lens. The condenser beam strikes the sample and, based upon the sample thickness, some bundle of electrons is transmitted through the specimen to be focused by an objective lens and form an image on a fluorescent screen. Characterization of film cross-sections has been analysed in this investigation by the TEM technique to reveal the effects of epitaxial growth of ferromagnetic layers on thin-film superconductors at their interfaces, since the layers of Fe and YBCO have incompatible order parameters. Where the images of cross-sections for samples were captured utilizing TEM is indicated in Figure 3.15.

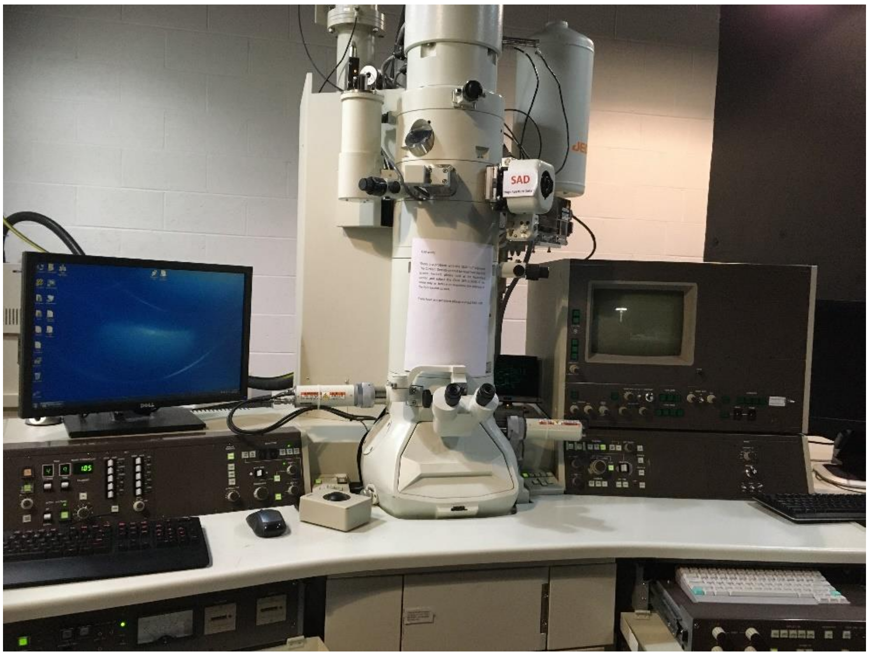

Figure 3.15 *Photograph of transmission electron microscopy at the University of Wollongong Electron Microscopy Centre*.

Chapter 4

Large artificial ferromagnetic dot arrays for critical current enhancement in superconducting $YBa_2Cu_3O_{7-\delta}$ thin films

4.1 Chapter outline

This chapter is devoted to the investigation of geometrical configurations of magnetic dots with size >> than the vortex length scale. A fabrication process for superconductor thin films and the epitaxial growth of dots (different geometries and patterns) on the YBCO surface has been characterized and then experimentally examined, along with an assessment of the films pre and post introducing the configurations. Critical current density calculation and characterizations for all sets of thin films have been undertaken and plotted as a J_c difference or $\Delta J_c/J_{c(as\text{-}grown\ film)}$ dependence on the applied magnetic field. This chapter also involved a characterization of the samples by SEM to clarify the morphology for both the YBCO surface and the magnetic configurations. Furthermore, to demonstrate the efficiency of the magnetic dot approach, an investigation has been conducted on a different approach, perforation of thin films (to create antidots). The outcomes are presented and analysed, with the results showing the differences in the pinning mechanisms for both approaches.

4.2 Introduction

Flux pinning of quantized magnetic vortex is arguably one of the most crucial parameters controlling the superconducting critical current density (J_c) at both self-field and applied magnetic field for many practical applications. As a result of passing electrical current in superconducting materials, a Lorentz force exerted on vortices that compels them to displacement from their positions, causes energy dissipation, thereby deterioration in superconducting state. However, avoiding the vortex mobility is via introducing counteracting force (pinning force) to hinder quantized vortices movement, so, achieving high critical current depends on the balance between pinning and Lorentz force. Tremendous efforts have been devoted to pinning enhancement by using different approaches, such as by introducing artificial pinning centre to localise vortices [60, 189-193], multilayering [17, 57, 58] and perforated films [136-138]. Researches has indicated the presence of intrinsic defects (in nanoscale) acting as pinning centre to pin normal vortex cores, are formed during thin film material growth process [60]. However, intrinsic defects (structural defects) facing abrupt decrease in the vortex pinning energy as temperature increases $U_{cp} \sim \left(\frac{H_c^2}{8\pi}\right)\pi\varepsilon^2 \approx (\frac{\emptyset_\circ}{8\pi\lambda_L})$, due to increasing London penetration depth λ_L as $\lambda_L(T) = \lambda_L(0)(1\text{-T}/T_c)^{-1/2}$, [$\lambda_L(0)$ ~160 nm for YBCO[194, 195]], thus very small or even negligible potentials pinning at temperature close to T_c [55, 142]. Therefore, introducing alternative effective artificial pinning centres (APCs) at high-temperature superconductor are required. The very fruitful approach to immobilize vortex motion in this work is through using magnetic configurations since they have the ability to pin (localize) the flux quantized magnetic vortices rather than the vortices core, in contrast to conventional pinning sites. This possibility has not been studied to a large extent, hence remains underutilized.

The magnetic pinning potential [143], figure out as an $U_{mp} \sim \Phi_\circ M_{(x)}\, d_s$, where $M_{(x)}$ and d_s are magnetization of ferromagnetic material and thickness of superconducting film respectively. Importantly, U_{mp} is independent of temperature, and overcome the limitations of temperature dependent condensation pinning energy U_{cp}. Therefore, magnetic pinning is considered a promising approach for increasing J_c at temperature close to T_c, which it is desirable for practical applications [143] and manipulation of magnetic flux [196, 197].

In thin films, regular periodic array of submicron magnetic dots have been used as an artificial flux pinning sites [198-200]. Vortex-antivortex pairs are induced by inhomogeneous stray field emanating from magnetic component, which interact with superconductor and locally degrade superconductivity. Moreover, the polarity of magnetic material, being in or out of-plane relative to the applied magnetic field, can play a significant role. Field-polarity dependent flux pinning was observed in the system consist of regular arrays of nickel dots, whose magnetization had an out-of-plane component, covered by niobium superconductor [201]. Asymmetric critical current density has been observed for positive and negative applied magnetic fields, which prove the dependence of J_c on mutual orientation of applied field and magnetization of the dots. Moreover, the magnetic contribution of the magnetic nano-inclusions has not been clearly singled out from the combined effect of additional strains and defects produced by these magnetic additions and their magnetic influence on vortex pinning in YBCO thin films [114, 202-205]. Furthermore, the nanoengineering of periodic and quasiperiodic arrays (size, thickness and spacing) has a substantial impact on the pinning strength by producing an vortex-antivortex configuration in the superconductor, which can be drastically different [152, 206]. M. V. Milošević et al. [18] demonstrate that superconductivity nucleation can be spatially controlled in an applied magnetic field using a system consist of Al thin film superconductor deposited on periodic square array of out-of-plane magnetized dots with gradually increasing diameter. They showed that superconductivity nucleate firstly at interstitial positions close to largest magnetic dots (higher magnetic moment) due to compensation effect, which annihilate the antivortex induced by magnetic dots. In contrast, when the ferromagnetic material is magnetized in-plane the vortex and antivortex induced by stray field are located at opposite sides of magnetic poles (trapped in the superconductor film) [207].

Microscopic magnets can provide stabilization for vortices, magnetic flux or giant vortices carrying more than one flux quantum by trapping magnetic flux more effectively [207]. Previous experiments with some configurations of nano-scale magnetic arrays demonstrated matching field effects with the density of pinning arrays being commensurate with that of vortex lattices [159, 162, 200, 208]. Matching effects in the nano-scale arrays occur at low fields.

In this work, we investigate how different geometric configurations and periodicity of magnetic dots in length scales comparable to the superconductor vortex physics (coherence length and penetration depth of YBCO superconductor) have on the superconductor properties affecting vortex pinning and current-carrying ability. These sizeable magnet can provide a stabilizing for a giant vortex which carrying more than one flux quantum, trapping magnetic flux more effectively [207]. Unlike to the previous experiments, the magnetic configurations were nanometre-sized, to investigate the effect of matching fields where corresponding density of pinning arrays are commensurate with that vortex lattices [159, 162, 200, 208]. The matching effects exist at low fields in contrast to present work where much boarder field rang, including high fields, over which measurable influence of the arrays with large magnetic dots is observed, furthermore, to increase the interactions between vortex-vortex and vortex-magnetic dots. These configurations give a value roughly 2.01×10^{-5} T and 4.8×10^{-5} T for first matching field at different lattice arrays of dots $H_n = n\emptyset_{\circ}/A_{uc}$ where the A_{uc} is the unit cell area of the magnetic dots lattice. Moreover, to achieve a matching effect in experiments with nano-scale arrays, a superconductor material was deposited on top of magnetic arrays where a possible source of pinning is present. In such systems, the areas of reduced thickness act as effective pinning centres (corrugations in the topography of the film due to the underlying disks) could lead to add pinning [209] in similar way to substrate engineering [125, 210]. In the present work, the magnetic arrays are deposited on the top of the film, hence the effect of corrugations is absent reducing the number of parameters in the analysis of the results obtained.

4.3 Thin films fabrication processes and introduce patterns

Our samples are >200 nm thick of $YBa_2Cu_3O_{7-\delta}$ thin film superconductor deposited on single crystal substrate $SrTiO_3$ (STO) of 5×5 mm^2 using pulsed laser deposition technique described elsewhere [17, 57, 211]. In-situ deposition of ~ 5-10 nm thick CeO_2 has been used as an intermediate layer (buffer layer) between superconductor and ferromagnetic material. CeO_2 has proven to be an effective buffer layer owing to its favourable film growth characteristic, minimal chemical reaction (chemical compatibility at high deposition temperature), a similar thermal expansion coefficient and good lattice match with YBCO [183, 212, 213] . Moreover, an intermediate layer has a role not only to damp the proximity effect [214], but also to avoid any deterioration in superconductor material due to loss of oxygen to oxidizing iron over time. The thicknesses are controlled according to the well-established deposition rates in our system, which depend on deposition frequency [57, 211], and verified by Dektak Profiler and transmission electron microscopy. Recently, these techniques was refined to the precision of about ±1Å [215]. The quality control has been done with the help of X-ray diffraction and X-ray reflectivity measurements [214], routinely producing excellent crystallinity for our YBCO thin films and hybrid structures. However, the ultimate property check is provided by the high critical temperatures of our YBCO thin films and their critical current density $J_c(0) > 10^{10}$ A/m^2 at $T = 77$ K in zero applied field (Table 4-1). It is well known that YBCO films with $J_c > 10^{10}$ A/m^2 show low misalignment angles $< 1^\circ$ between the structural film domains, allowing highest current carrying transparency [10, 69] and together with $T_c \geq 90$ K implying high quality thin films.

After coating the superconducting thin film with positive photoresist, the desired pattern was defined on a photoresist layer by an optical lithography technique (Heidelberg Instruments μPG 101). Using the same technique of pulse laser deposition at room temperature, a ~100 nm of ferromagnetic material (iron) was deposited on top of photoresist layer to fill the exposed holes (pattern), followed by baking and lift-off in developer process. Figure 4.1 shows a brief schematic of samples fabrication steps.

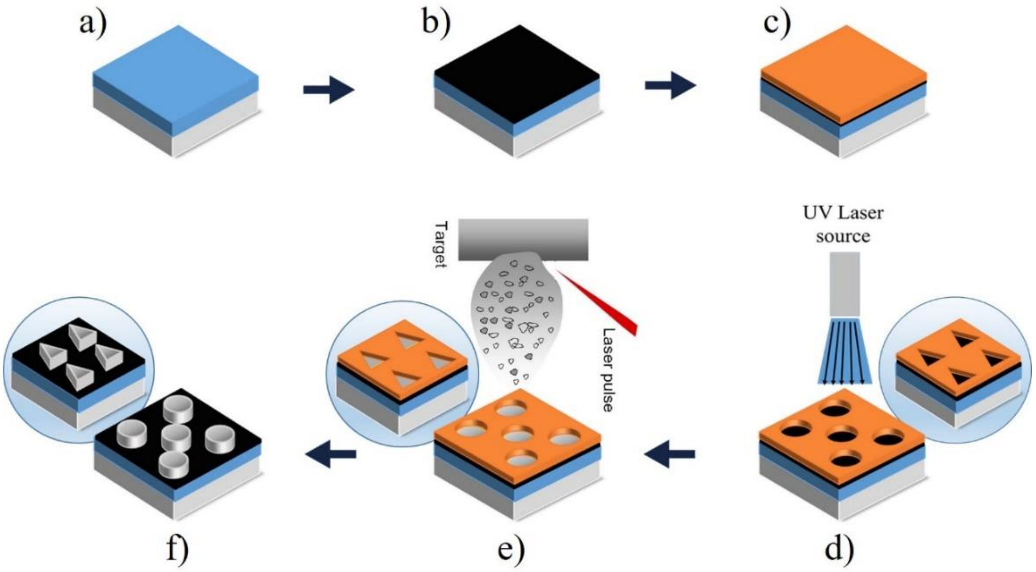

Figure 4.1 *Schematic diagram of the fabrication processes thin film superconductor and microstructure dots arrays: a) Deposition of ~250 nm of* $YBa_2Cu_3O_{7-\delta}$ *on Single crystal substrate by pulse laser deposition technique. b) in-site deposition has been employed to cover YBCO with an insulator layer of* CeO_2*. c) Spin coating has been used to cover sample surface with a positive photoresist. d) Exposure sample to UV laser making a desired pattern on sample. e) Filling the holes with ferromagnetic material by same technique of deposition YBCO but in different conditions. f) Immersing the sample in acetone and lift-off process, can get the magnetic dots.*

The structural property of so-obtained iron dots are not essential for this work dealing with the influence of their magnetic properties on the current carrying abilities. The magnetic properties are quite similar for every Fe dot pattern investigated. Typical hysteresis curves for in-plane and out-of-plane magnetizations are shown for sample 2 and 7 in Fig. 4.2 as an example where they have a different amount of ferromagnetic component.

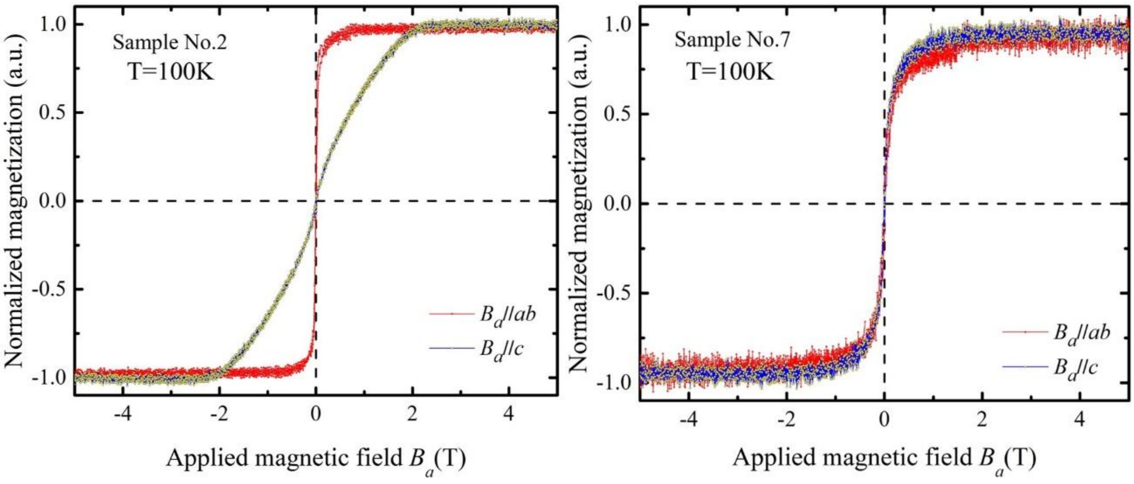

Figure 4.2 *Magnetization hysteresis loops for the Fe dot array of square array of triangles (sample 2)and Inv. Graded array of triangles (sample 7) as a function of the magnetic field applied in-plane and out-of-plane of the film measured at T=100 K, which is above* T_c*.*

In this work, we investigate two sets sample, one with seven different ferromagnetic (FM) arrays and second with three arrays of antidots (fully perforated), whose description together with the corresponding superconducting characteristics of their host as-grown YBCO films on top of which these arrays were introduced are listed in Table 4-1.

Furthermore, a confirmation have been done to prove the pinning performance by magnetic dots configuration is relatively significant effect on J_c behaviour compared to their counterparts of antidots arrays.

Table 4-1 *Sample characteristics, including superconducting characteristics of the as-grown YBCO films and their corresponding artificial pining arrays introduced on them*

Sample No.	**Array description**	**Total number of dots (antidots)**	**Total volume of iron (µm^3)**	**T_c (K)**	**J_c (0T, 10K) (×10^{11} A/m^2)**	**J_c (0T, 77K) (×10^{10} A/m^2)**
1	Square array of triangles, w=10µm	86400	40608	90.3	8.2	3.6
2	Square array of triangles, w=6µm	230000	108100	91.6	3.9	2.2
3	Hexagonal array of triangles, w=10µm	173100	81357	91.7	4.3	3.9
4	Square array of squares, w=10µm	86400	93312	92	2.07	0.75
5	Hexagonal array of circles, w=10µm	173100	147135	90.1	7.1	2.6
6	Graded array of triangles	10088	4741	91.9	7.8	6.8
7	Inv. graded array of triangles	2517	1183	90.2	6.4	5.4
8	Square array of triangles, w=10µm (antidots)	86400	--	93.7	4.1	3.5
9	Square array of triangles, w=6µm (antidots)	230000	--	92.3	4.2	3.7
10	Hexagonal array of triangles, w=10µm (antidots)	173100	--	90.7	3.2	0.89

The patterned samples include uniform are (circle in a triangular array, triangle and square in a square array), whereas the samples with non-uniform pattern are (graded and inverted graded triangles), as shown in the Figure 4.3, are implemented on area of 3×3 mm^2 of a corresponding YBCO film. The uniform arrays (circles, triangles and squares) Figure 4.3(a, b), had a period of 10 µm, with magnetic dots d = 3 µm (d is diameter or side length). These dimensions are much larger than both the coherence length and penetration depth of YBCO superconductor (ξ~2nm and λ = 160 nm respectively[194, 195]). The non-uniform (graded and inverted graded) Figure 4.3(c, d) consisting of a sets of triangle ring with a side length of triangle d = 3 µm. These films either have higher dense of rings at the centre and low at edges (increasing outward) or vice versa (increasing inward) for inverted gradient and graded sample respectively Figure 4.3(c, d). The spacing between adjacent rings increased by a factor of 1.618 for both non-uniform arrays. This factor is the so-called golden ratio shown to be beneficial for a 1D quasi-periodic chain [216] and graded antidote arrays [136].

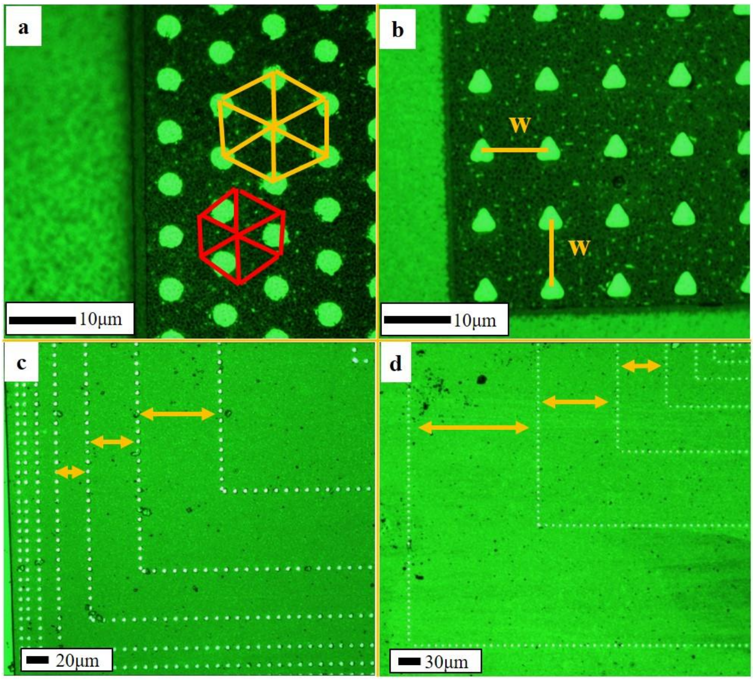

Figure 4.3 *Shows the arrays of these ferromagnetic configurations. a) circle arrays hexagons regions indicate to different vortices locations, beneath dots yellow line, and interstitial between dots red line, b) triangle arrays symbol (w) indicate to a periodic array, c) graded arrays and d) inverted graded arrays*

Magnetization measurements with the magnetic field applied perpendicular to YBCO sample surfaces (aligns along the z-direction) have been conducted by using Quantum Design Physical Properties Measurement System (PPMS) for each sample twice: first time after YBCO film deposition and then after introducing artificial pinning sites (fabrications of iron arrays on CeO_2 buffered YBCO surfaces and atidots arrays in YBCO structure) to enable the evaluation of J_c changes introduced by each arrays to a corresponding YBCO film.

The magnetic hysteresis measurements were carried out at temperatures 10 K, 40 K, 60 K and 77 K and up to the magnetic field of 5 T. We note that Fe dot arrays deposited on the top of CeO_2 layer protecting YBCO surface, we have not observed any substantial changes in T_c values.

The critical current density has been estimated from measurements of the hysteresis loop pre and post the pattern has been introduced at specimens. J_c was calculated by using the formula as following:

$$J_{c=}\frac{3\Delta M}{W_p} \qquad 4.1$$

Where ΔM is the magnetization and define as the quantity of magnetic moment per unit volume equal to ($\Delta M = \Delta m/\mathrm{v}$) Δm is the magnetization difference between ascending and descending magnetization branches, and (W_p) is the width of the square superconducting samples [17, 74, 141]. The $J_c(0)$ values measured at $B_a = 0$ T for as-grown films is given in Table 5-1.

Magnetic measurements in zero field-cooled regime also allows direct determination of critical temperature T_c and transition width ΔT_c at the applied magnetic field $B_a = 10$ mT. T_c is defined at the onset of the superconducting transition. The transition width and critical temperature are very important characteristics, they show the quality of samples (structure homogeneity) and reflects the fraction of non-superconducting phase in the material. Table 5-1 displays the critical temperature for all the samples investigated.

4.4 Results and discussion

4.4.1 Assessment sample quality

The aim of introducing a regular arrays and non-uniform arrays magnetic dots is not only to observe a clear pinning effect when vortex lattice interact with arrays of magnetic dots, but also to understand the behaviour of vortex dynamics which can be tuned by modification pinning properties of artificial arrays.

Magnetic transition analysis reveals a superconducting transition temperature (T_c) and transition width (ΔT_c) for these samples, which have been used to assess the quality of film. The highest T_c, B_{c2} and sharpest transition temperature is a desirable for practical application, as all these parameters broadens the domain at which superconductors can be applied. The transition temperature is defined from magnetization moment measurement, subtract between 10% which corresponding the highest temperature from 90% which is the lowest [217, 218]. The points where the two dashed lines are intersect as indicated in Figure 4.4 (a), where (b) shows the sample has not affected by deposition proceedings of ferromagnetic material. The two curve for the sample are practically identical, i.e. there is no distortion in superconductor thin film structure, which it is more likely that the specimen have highest periodicity between magnetic dots.

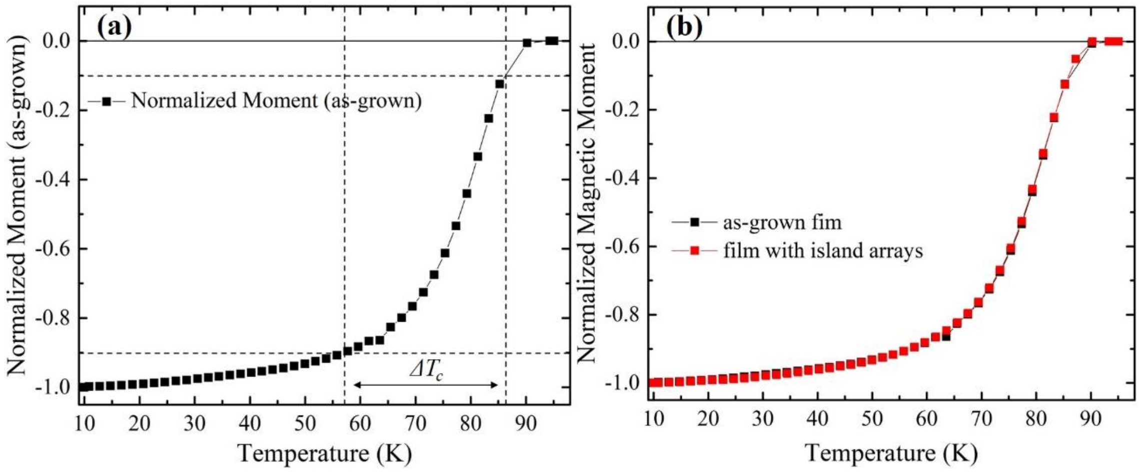

Figure 4.4 *Normalized magnetization vs temperature for: (a) as-grown film to define transition width and* T_c *for sample at ZFC condition and applied magnetic field 0.01T, (b) the two films pre and post introduce the artificial magnetic dots square array of triangles with w=10µm.*

4.4.2 Sample characterization

Figure 4.5 displays an image of Scan electron microscopy for an array of supposedly triangles (sample No.1). The images show that magnetic dots have a rounded corner which is unexpected (sharp corner instead), this attributed to the resolution of laser that has been exposed to the sample, as the minimum limit resolution of the optical laser used is 1μm. Furthermore, SEM images show that a brightness regions at the edges of dots and its clearly at Fig. 4.5 (a and b), where is a small amount of ferromagnetic material has propagated underneath photoresist layer due to improper lift off as some photoresist is removes during development process. In addition, a sidewall of magnetic dot is revealed at Fig. 4.5 (c) (indicated by a yellow lines) by using the camera's tilt feature of SEM. It is worth noting that due to CeO_2 buffer layer is present, common defects (such as pores) on YBCO surface are barely visible on image.

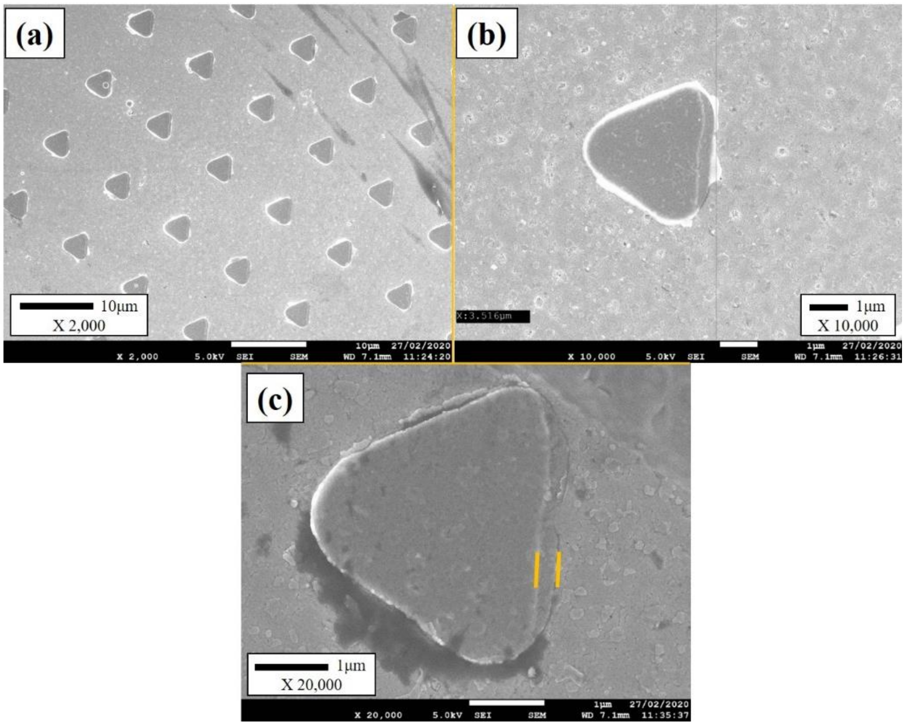

Figure 4.5 Low magnification of SEM images for sample No.1, showing surface of YBCO thin film and epitaxial growth of magnetic configurations.

4.4.3 Mechanism of flux lines pinning with micron magnetic configurations

The interaction between vortex lattice and the artificial pinning centres, created by arrays of magnetic dots results in a different pinning behaviour, which can be indicated as a reduction or increase in capability of carrying electrical current as a function of applied magnetic field. At low field, vortices are sparse, so the mutual interactions are less pronounced [219, 220], and mainly occur individually with different defects present in the material as a single vortex pinning regime. However, if a defect or rather a potential energy in the form of a magnetic dot is much larger than both ξ and λ, as well as the intervortex distance [194, 195], then any pronounced vortex pinning effect, such as matching [151], is unlikely. These dimensions and expectations are the case of this work.

By ramping up the applied magnetic field, collective pinning effect are dominated in which vortex matter enters in a regime where vortex–vortex and vortex–defect interactions start to compete [55, 131, 194, 195, 221-223]. Additional interactions of vortices with magnetic dots or those pinned interstitially can play a crucial role in localizing vortices. These vortex interactions and their probability to be pinning are likely to be proportional to the size of magnetic dots, i.e. the bigger size magnetic dot, the more vortices can occupy it (up to saturation number). The saturation value n_s defined as, the expected number of vortices accommodate at dots before a repulsive forces between vortices exceed the pinning potential, and given by $n_s = d/4\xi(T)$, where d is the dot dimeter [224-226]. Thus, the more vortices inside one dot, the stronger repulsive interaction between them. This may leads to mitigate motion of interstitial vortices [131, 163, 227, 228]. Moreover, due to increasing λ, the saturation of magnetic dots could decrease with increasing temperature.

Figure 4.6 shows examples of J_c behaviour and it is dependence on B_a for two as-grown YBCO film (samples 3 and 5) and the films with their corresponding magnetic dots arrays deposited on top of YBCO film at different temperature, showing different trends in J_c inflicted by the Fe arrays. The distinct feature for these curves has been observed, where crossover effect is apparent at B_a 0.5 T for sample 5 as a result of interaction between magnetic and vortex lattice, and it is obvious for all the temperatures measured. The J_c enhancement attains almost a factor of two at $B_a < 0.1$ T for $T = 77$ K. Sample 3 displays an example of non-monotonous dependence with degraded J_c at low fields, enhanced J_c

at intermediate fields, and almost no effect by FM arrays at high fields. The critical current density behaviour has been presented at Figure 4.7 for all the samples mentioned at Table 4-1.

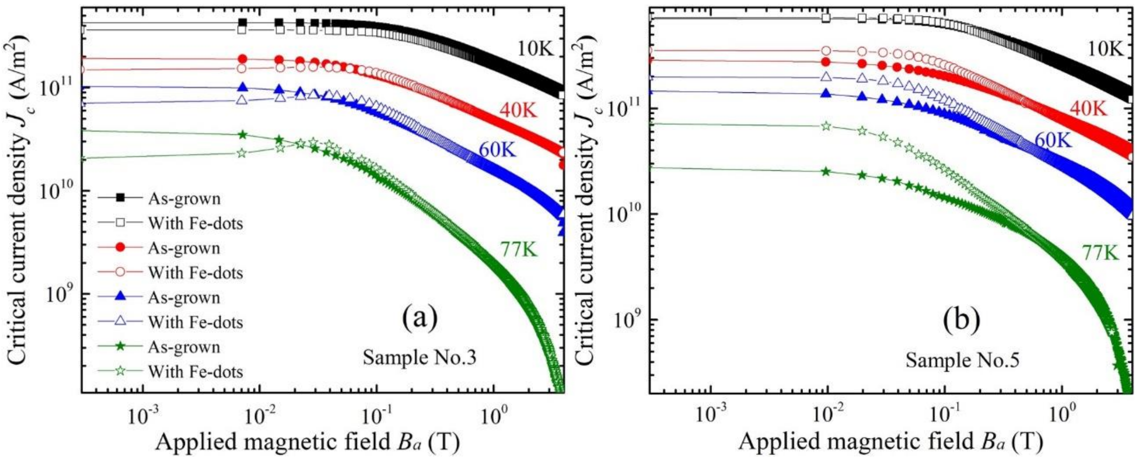

Figure 4.6 *Critical current density as a function of applied magnetic field in log-log scale at given temperature for sample, a) square array of triangles with w=10μm, b)hexagonal array of circles the* J_c *has been extracted by using the equation 4.1.*

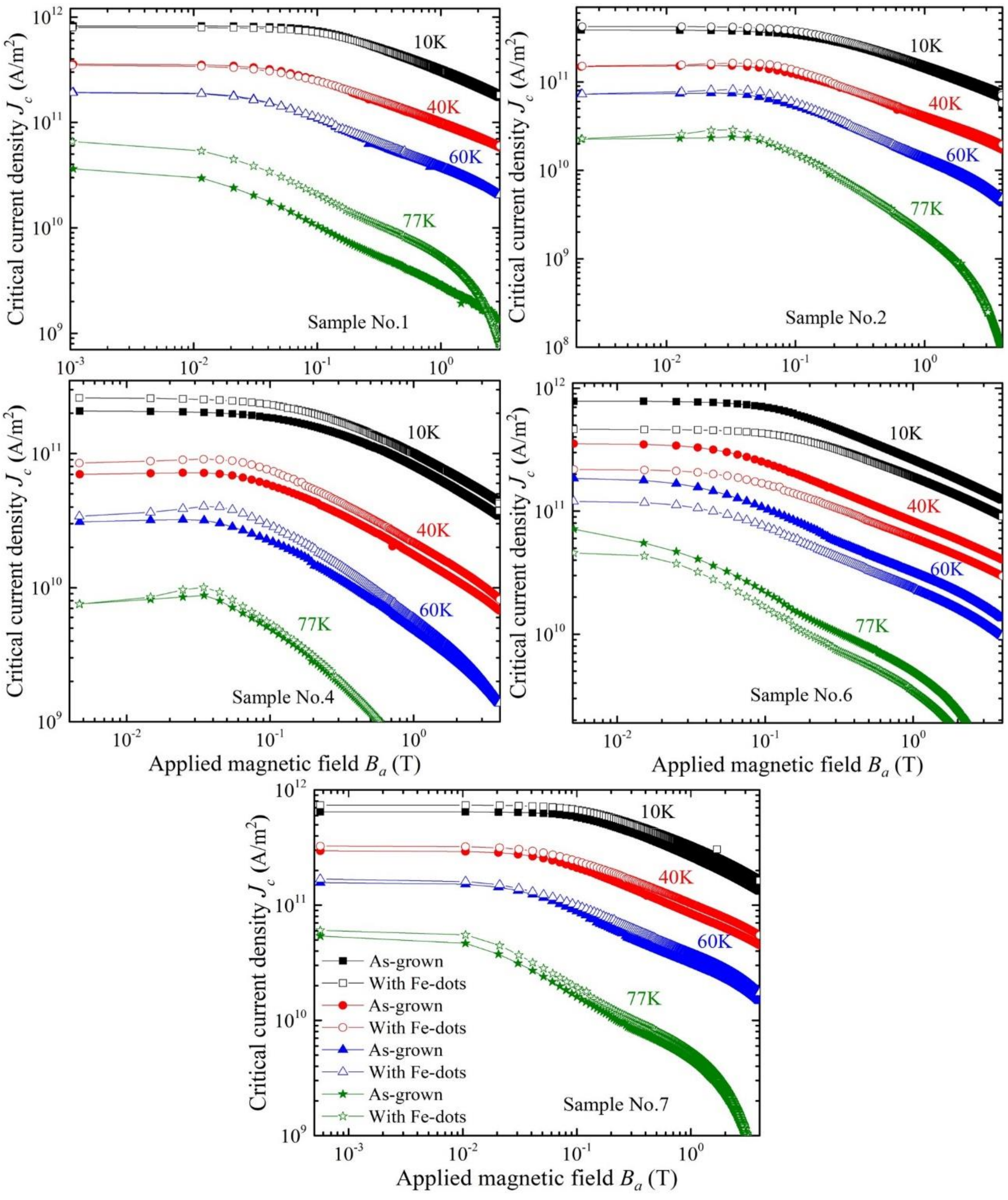

Figure 4.7 *log-log scale for magnetic field dependence of the critical current density J_c, the samples are presented at table 4-1 with magnetic dots lattice at given temperatures.*

The findings in Figure 4.8 present the differences in J_c ($\Delta J_c = J_c^{patterned} - J_c^{as\text{-}grown}$) for all samples pre and post introducing magnetic dots as a function of applied magnetic field. There is no obvious consistency between the results for different types of arrays. However, J_c affected clearly by magnetic dots arrays by either decreasing or/and increasing it quite dramatically. Moreover, the J_c behaviour have also very different trends to that obtained by similar sizes and shapes of fully and partially perforated (non-magnetic antidot arrays) [125, 136, 138, 210]. This difference immediately and firmly hints at the magnetic origin of the observed ΔJ_c features. A most striking general feature of magnetic dot influence on J_c is the ΔJ_c non-monotonous dependence as a function of applied magnetic field, as oppose to monotonous dependences observed for very similar sized, shape and arrangement non-magnetic antidote arrays [125, 136, 138, 210]. At a closer inspection, it is possible to find some qualitative explanations to the observed ΔJ_c (B_a) behaviour affected by the magnetic dot arrays.

The specimen 6 (graded magnetic dots) has shown a degradation in J_c over the entire range of magnetic field and temperature after magnetic dots were introduced. This outcome might be unexpected, especially in the light of the earlier work on inhomogeneous antidot arrays including the graded antidot arrays [136], which have been shown a consistently enhancement for this type of arrays although containing non-magnetic antidots. However, taking in to consideration a low number of magnetic dots, which mainly located around the edges of the film Figure 4.3(c), and low volume of iron Table 4-1. It is reasonable to expect a higher magnetic flux accumulation near the edges, where the flux is also always enhanced by the demagnetizing effect. This would create a lower potential for flux entry and exit, resulting in lower J_c.

Figure 4.8 mainly exhibit a positive ΔJ_c behaviour for Samples 2, 4 and 7, which imply that the enhancement at J_c is attributed to the magnetic dots arrays. The notable common features in the magnetic dots arrangements at samples 2 and 4, that they have a large number of magnetic dots in the arrays and highest overall Fe volumes Table 4-1. In contrast to sample 7, the majority of magnetic dots are at the centre part of sample Figure 4.3(d). These specific features are likely relevant to the J_c enhancements.

Sample 1, 3 and 6 have a similar trend, where the J_c behaviour to some extent constant at low applied fields $B_a < 0.1$ T Figure 4.9, and it raises up at higher fields. This trend in most cases is prone to samples with both positive and negative of J_c behaviour. Notably, there is one thing in common for samples with this trend, they all possess relatively small number of magnetic dots and total volume of iron deposited Table 4-1. Also, a similar behaviour of J_c have seen for samples 2, 4 and 5, which is unlike to the group of samples mentioned above. It start with a constant but in a positive value of J_c behaviour at low field and the degradation is more dominant at $B_a > 0.1$ T Figure 4.9. A most dramatic degradation is observed for sample 5 for all temperatures. Where the curve drops from positive to negative values at field around 0.5 to 0.7 T Figure 4.8 and 4.9. Furthermore, this group of samples have ultimately the highest number of magnetic dots and total volume of Fe among all the samples investigated in our work, with sample 5 having the most iron amount Table 4-1. Thus, a degradation in ΔJ_c behaviour at high fields can imply that an excessive magnetic flux are accumulated in the samples due to high magnetic susceptibility of Fe at high fields, which cannot be effectively pinned in YBCO films leading to suppression of J_c.

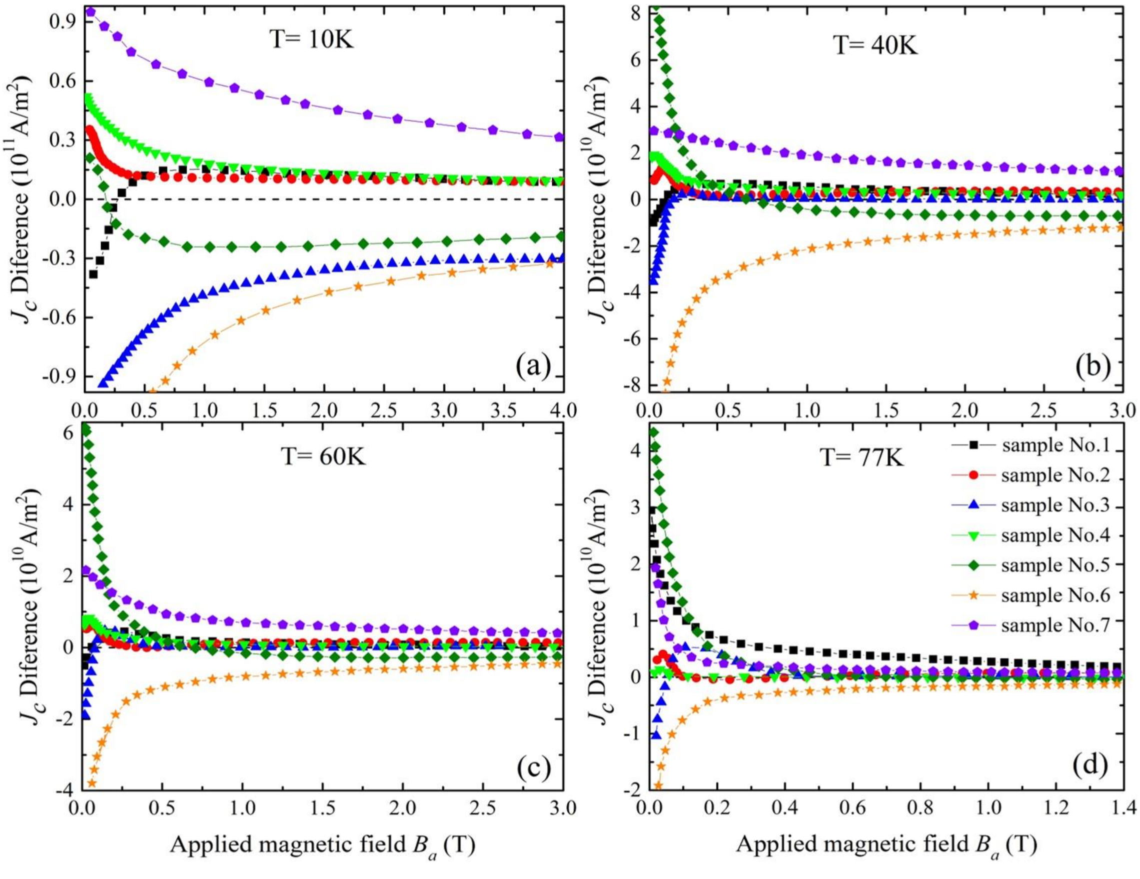

Figure 4.8 *Critical current density difference as a function of applied magnetic field between pre and post introduce an array of pinning sites for a) 10K, b) 40K, c) 60K and d) 77K.*

To give more precise and full insight on J_c behaviour, a relative change in J_c versus applied magnetic field for all samples investigated are shown in Figure 4.9, i.e., $\Delta J_c / J_c^{(as\text{-}grown)}$ as a function of magnetic field at given temperature. The inverted arrays of sample 7 display a distinctive dependence of J_c enhancement, since having the lowest number and total volume of iron magnetic dot Table 4-1. The curve shows an enhancement at J_c about 10% and further increses occurred up to ~25% at $B_a > 0.1$ T over the entire temperature rang. This increment is no longer exist at highest measured fields. However, a dramtic degradation has been observed for sample 5 at all temperature (having the large number of dots and highest Fe volume). A relative change at J_c drops from positive to negative values at range of field of (0.5-0.7)T. this behaviour is more obviously at $T = 77$ K, at which J_c deteriorat from ~ +100% to ~ -20. While the samples 2 and 4 showing a variations to J_c of about 10% compared to initial plateau-like behavior at low fields, with sample 4 developing the J_c drop of up to 25% at highest measured magnetic field and 60 K.

It is worth to emphasize that, magnetization hysteries loop measurements have been carried out on magnetic dots by applying amgnetic field in and out of sample plane above the T_c. Hysteric loop shows a saturation point of iron could not be achieved up to about $B_a \sim 2$ T for out of plane. In contrast to in plane field orentation, saturation point was achieved at around 0.5 T Figure 4.2, similar to that observed in [115]. Fe can effectively screen a superconductor from the applied magnetic field before reaching the full saturation as was observed for Fe-sheathed round wires in [86, 229, 230]. Thus, large amount of iron at these samples play a relatively role to provide some shielding from magnetic flux, so a contribution at the mostly positive J_c behaviour observed at Figure 4.9 (samples 2, 4 and 5).

Samples 3 and 4 show a conterviertial resutls although they have a certain commonalities, such as a total volume of iron Table 4-1. A relative change in J_c for sample 4 is > 0 and deteriorate at high fields. However, it has a lowest J_c among all the sample used in this investigation Table 4-1. In contrast, to sample 3 which has a mostly negative J_c behaviour. This might be imply that externally instigated J_c improvement could be more likely of the samples with the lowest J_c. while, samples with high J_c could have less ability to withstand J_c of higher amplitudes.

In addition to mentioned above, different shapes of dots arrays (triangle, square and circle) has been presneted at Table 4-1, which would also affect on behaviour of J_c and $\Delta J_c / J_c^{(\text{as-grown})}$ by provideing a lower or higher pinning properties of vortices. The base of triangle and square lattice dots which have a parallel orientation to sample edges provided a higher pinning effective (which is unlikely to occur for the array with the round dots sample 5) for vortices than vertices (due to vertical relationship between Lorentz force and the base of triangle) [163]. Moreover the high concentration of screening current near vertices and sharp bends in triangle and square suppresses superconductivity at this point thus, a large Lorentz force are induced. Hence, vortices have more opportunity to leave via vertices and sharp bends than the base of magnetic dots [231, 232]. While the tilted sides of the triangular dots allow sliding of vortices inward toward the centre forming an easy flux flow channelling with increasing of penetrating vortices for the film [131, 136, 140]. This explains the contrast in critical current density difference at Figure 4.8 for both triangle and square lattice (sample1 and 4 respectivly) with increasing temperature, even though such larger pinning strength cannot be attributed to the size of the dot, which is smaller for the triangle [233]. Furthermore, inverting the graded array (sample 7) prevents the formation of easy channels of vortex flow [234]. As mentioned before that sample has less density of magnetic dots near the edges as indicate in Figure 4.3(d), so, easy channelling of vortex flow inwardly to centre sample is unlikely to occur due to large distance between the first and second rings of magnetic dots. This in complete contrast to graded array sample as shown in Figure 4.3(c), which is revealed presence an easy channeling this elucidates the degradation in ΔJ_c of this configuration arrays Figure 4.8 [125].

It is particularly interesting to notice that, at large enough magnetic fields and temperature close to T_c where pinning strength of magnetic dots relatively higher than intrinsic, sample 1 has demonstrated somewhat better performance than counterpart sample 2 panel (d) Figure 4.9. At high temperature, less vortices can be packed per unit area. This can be explained as vortex order parameters (coherence length and penetration depth) and its dependence on temperature. As mentioned above sample 1 has larger periodic arrays posses less number of magnetic dots or less amount of iron Table 4-1, thus vortices penetrating sample has less opportunity to settle down, this increases the potential of interaction with trapped vortices induced by magnetic dots at sample. In contrast to sample 2 with less periodic arrays, vortex experinece a repulsive interaction with those being already pinned at magnetic dots. Thus, an increase in the applied magnetic field an accumulation of vortices is more likely to occur. This implies that interactions between penetration vortices and spontaneously induced by magnetic arrays are rare. In addition to that, sample 2 has the largest overall voulme of iron and number of magnetic dots confugrations Table 4-1, in this case a local suppression in an underlying superconductor order parameter is considerable, since an interactions of spontaneous vortices from magnetized magnetic dots with applied magnetic field flux quanta are rule out (a persistent nucleation of vortices at sample structure) [200].

On the other hand, circle dots arrays (round dots Figure 4.3(a)) in Figure 4.9 are provided stronger pinning areas, since this array have no vertices and magnetized more homogenously. An improvement in the performance with increasing temperature is seen at low field $B_a < 0.5$ T and $T > 10$ K. Increasing temperature, the intrinsic pinning of YBCO film, occurring on dislocations having suitable dimensions for it of the order of $\xi(0)$, is somewhat suppressed [17, 57, 195, 211]. This might be emphasis that magnetic pinning contribution is more substantial in this case. At the same time, magnetization measurements for dots showing that magnetic arrays are saturated at high applied magnetic fields Figure 4.2 (depend on dots number and total volume of iron). This negates a contribution of magnetic pinning and even likely degrading the J_c as observed in the measurements at Figure 4.9. Furthermore, local hexagonal ordering of this array Figure 4.3(a), is unlikely to distort the Abrikosov triangular vortex lattice which can play a crucial role at effectiveness of flux pinning. A theoretical studies has been carried out at perturbations that take place on triangular vortex-lattice phases as a function of periodic pinning potential strength [206], i.e. a definite relationship has been realized between vortex lattice and magnetic dots array [200].

In general, a striking feature of flux lines pinning magnetically, is the robustness to the rising temperature and magnetic field, which is obvious from behaviour of critical current density ΔJ_c and relative change at J_c Figure 4.8 and 4.9 respectively. Previous observation of critical current behaviour with antidots (non-magnetic) [136, 138] as pinning centres configuration, has indicated to the weakened performance of this type of pinning sites (damaging at superconducting integrity). The vortex is unlikely to existence within pinning sites (holes) where the pinning mechanism is performed on the edges of antidote. The Pinning mechanism affected by this approach through an abrupt decreasing at critical current density value and will discuss this issue in more details at section 4.6.

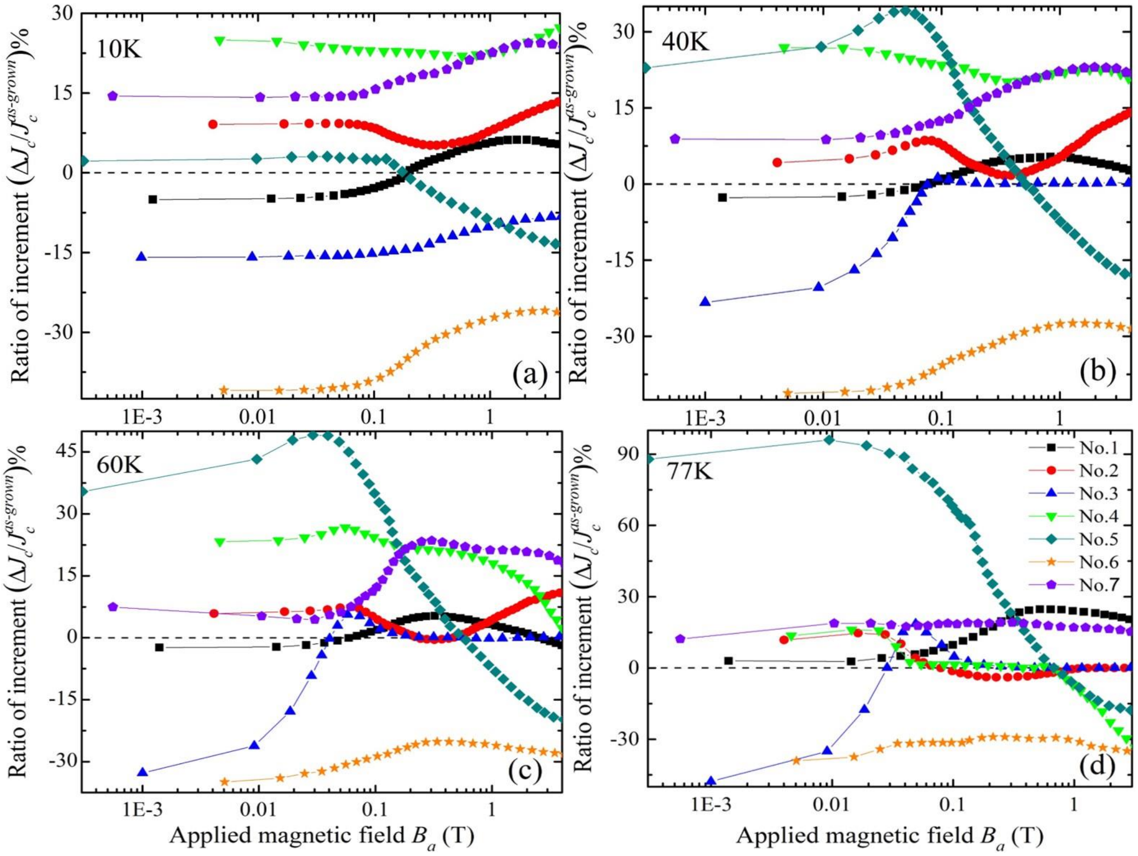

Figure 4.9 *Percentage of increment at critical current density as a function of applied magnetic field for different arrays of magnetic configurations at: a) 10 and 40 K, b) 60 and 77K.*

Another relevant note that need to be highlight, that using the critical state model for $J_c(B_a)$ estimations assuming uniform J_c distribution, which may not be the case for magnetic flux localizations within the magnetic dots, can be as much justified as for any other similar method of J_c estimation in inhomogeneous systems with likely even less uniform J_c. These inhomogeneous systems can be granular superconductors, such as Bi-tapes, polycrystalline bulk samples, compressed powders, some early poor quality YBCO coated conductors, as well as geometrically irregular samples including irregularly shaped single crystals.

4.5 Quantitative comparison of magnetic and non-magnetic flux line pinning

For realizing the comprehensive objective of flux pinning by large magnetic dots, a comparison with other approaches of artificial flux pinning is required. The main reason is to examine the effectiveness of this approach relative to others, since this feature expands the potential for using superconductors under varying ambient conditions.

The samples were fabricated, and a pattern was introduced in samples 8, 9 and 10 in the same manner as for samples 1, 2 and 3 respectively, as listed in Table 4-1 (with no need to deposit a buffer layer in this case). After development, ion beam etching was used to etch the samples with the desired pattern. The films were exposed to Ar^+ ions using an RFM30 ion gun for 45-50 minutes at chamber pressure of 3×10^{-4} mbar with current (ion density), acceleration voltage, and power of 22 mA, 350 V, and 118-120 W respectively. Therefore, any areas exposed to the UV laser were completely removed, followed by washing the samples with acetone and ethanol, and leaving behind a fully perforated samples with precise antidot arrays. A typical arrangement of asymmetric antidot lattice (pinning landscape) patterned in the YBCO films is shown in the SEM and optical microscope images in Figure 4.10.

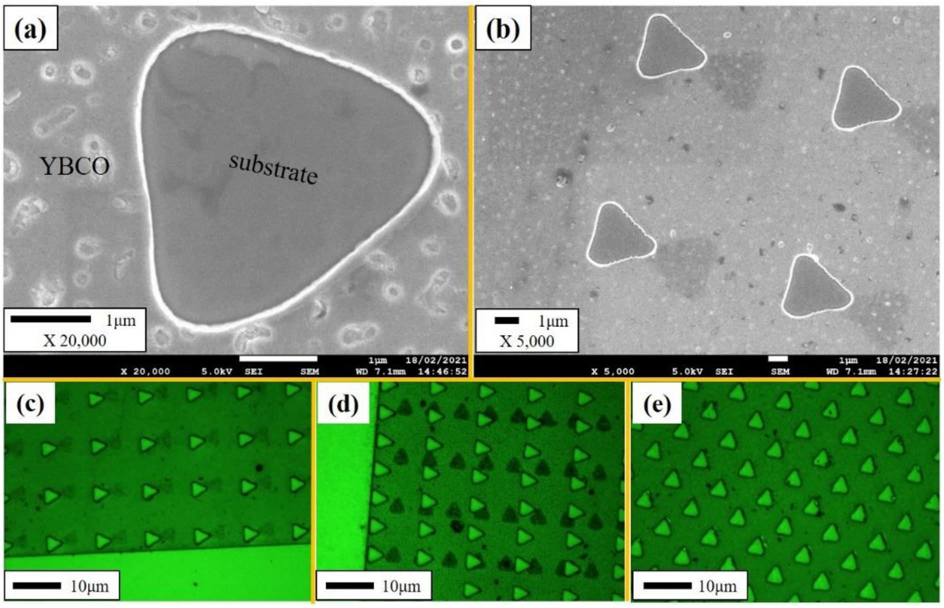

Figure 4.10 *Scanning electron microscope images of the YBCO surface with hole arrays (perforated samples) as artificial pinning sites: a) and b) samples 8 and 10, respectively, c), d), and e) are optical microscope surface images for samples 8, 9, and 10, respectively, post exposure to ion beam etching. The periodicity and number of antidote in the lattices for the samples mentioned are presented in Table 4-1.*

It is obvious from Figure 4.10(a) and (b) that the pattern edges for the samples are not sharp (rounded), which was not supposed to occur, and furthermore, did not correspond to the original pattern that was applied to the samples. This may be attributed to underexposure, limitations in laser optical resolution, extra scattering, diffraction from the edges [235], and improper lift-off of the photoresist [236]. The patches that are apparent in Figure 4.10(b), (c), and (d) are due to applying the pattern on the samples more than one time (exposure to laser lithography). Since the pattern was implemented over an area of 3 × 3 μm^2, more precision was needed to adjust and apply the pattern on the superconductor area solely by pre-exposing the film to the Ar^+ ion beam.

In addition, the critical temperature T_c of the YBCO films was not affected by the patterning, indicating that no damage was induced near the areas of the patterns. Values between 88 and 92 K were obtained in all the cases.

Analysis of the data for the films for J_c improvement was estimated from magnetization measurements, with the applied magnetic field B_a // c reaching as high as 4 T at the given temperatures shown in Figure 4.11. It is obvious that there was a reduction in J_c performance for all antidot (uniform array) samples at low and high applied magnetic field, which is consistent with the results of George et al.[136] and Jones et al. [138].

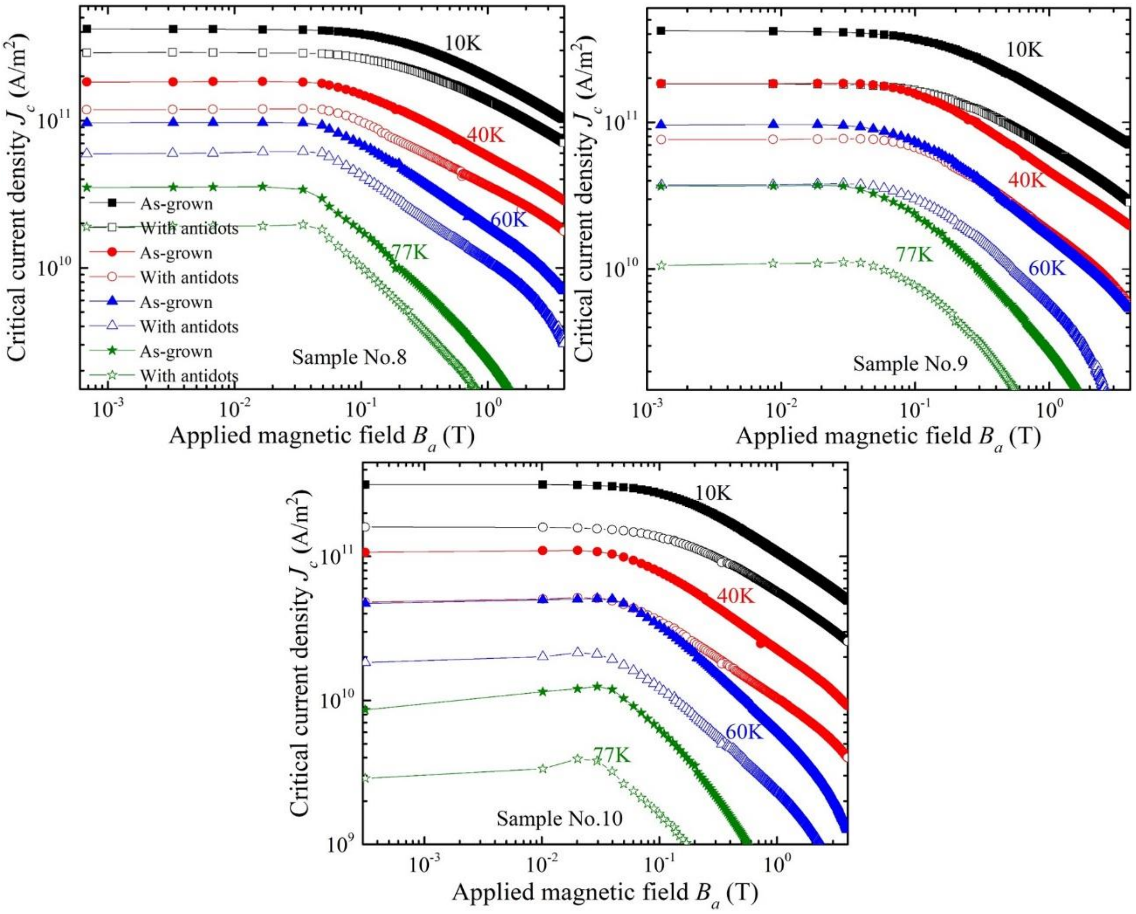

Figure 4.11 *log-log scale for magnetic field dependence of the critical current density J_c. The samples are presented in Table 4-1 with antidot (hole) lattices at given temperatures.*

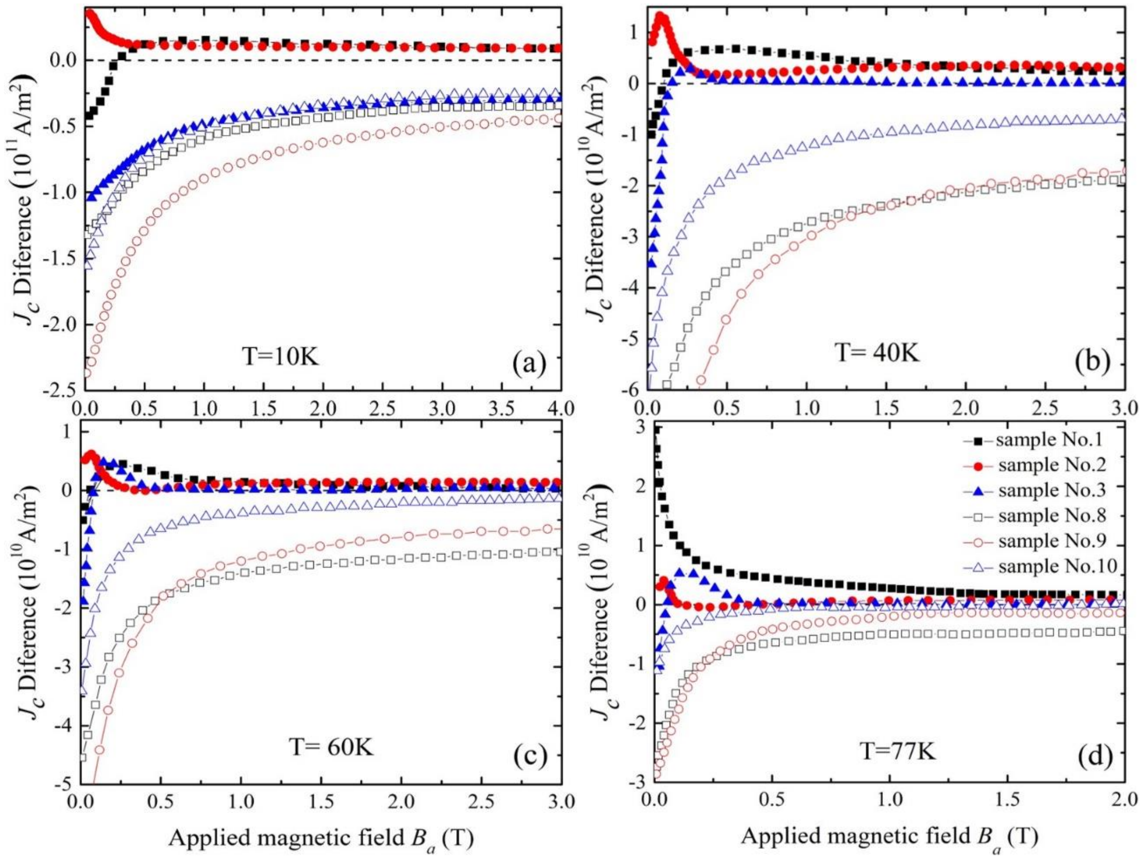

Figure 4.12 *J_c difference for samples patterned with antidots from equivalent samples patterned with magnetic dots as a function of applied magnetic field for the given samples, showing the effectiveness of each approach in flux pinning at low and high temperature.*

The main feature in flux pinning by antidots is that vortices cannot physically exist within holes (fully perforated antidote arrays) which might have an effect on the pinning mechanism in these configurations. In contrast to the pinning by magnetic dots. The J_c difference for the samples under consideration is displayed in Figure 4.12, and they are described in Table 4-1. It is clearly from the curves that the magnetic dot arrays are more effective in flux pinning over the whole magnetic field region in both low and high temperature, since the degradation of films with antidot configurations produces a negative values in J_c, which is more apparent in the plotted curves in Figure 4.12. An increase in the interaction between the pinning sites and vortices would promote establishment of a barrier to impede more vortices from penetrating the sample, i.e., a repulsive interaction with others as they approach. This barrier at antidots arrays has less effect, since the number of vortices confined at pinning sites are less because vortices are trapped at the edges of antidot arrays. Figure 4.11 shows that all the antidots arrays have the weakest performance in J_c behaviour at 10, 40, 60, and 77 K, and even negative values for J_c difference. This is in contrast to their counterpart magnetic dot arrays, even though these patterns are more likely to support the flux channelling effect [131, 140]. Whereas, the dot magnetic pattern showed a three-fold enhancement in critical current density at self-field compared to non-magnetic arrays, as shown in Figure 4.12(d). This enhancement is actually in agreement with the scenario of magnetic pinning. Accumulation of flux on triangle corners after vortices slide on channels toward triangle vertices, drive vortices to break away to a neighbouring triangle [237]. In addition to that, Table 4-1 indicates that the number of antidots introduced on sample 10 is more than on sample 8, i.e., extracting a greater amount of superconductor material has more effect on the film integrity (cross-section reduction). As mentioned previously, the edges of triangular antidot arrays play a significant role in pinning a large number of vortices (magnetic flux quanta), and that number is likely to be proportional to side the length and density of pinning sites. Furthermore, the antidot arrays for sample 10 are characterized by the presence of antidots at interstitial position for each array cell, while the periodicity of pinning sites (antidots) has a pronounced effect on behaviour of J_c difference sample 8 and 9 in Figure 4.12. A perturbation of the vortex lattice is more likely to occur with a sample of less periodicity, such as sample 9. Increasing the repulsive interactions between vortices that are already pinned at antidots and penetrating vortices as the field is ramped up gradually would promote distortion of homogeneous vortex configurations. Thus, a non-Bean-like profile for vortices on ascending and descending applied magnetic field branches (vortex entry and exit) is dominant [238].

We can arguably that the main characteristic features of magnetic configurations from antidots, are the restrictions in selection of the size of pinning sites and the way to disperse them on the sample (the sort of pattern). Whereas, the higher the density and the larger the antidot lattice is, the more likely it is to distort superconductor integrity. Therefore, this approach would not be a practical way to improve superconducting properties in high applied magnetic fields. In this case, precise selection of appropriate geometric configurations and patterns with lesser amounts of superconductor removal [138, 139] are required. On the other hand, magnetic pinning gives more opportunity to adopt any geometries or sizes, as long as the superconducting thin films are protected from any distortion in their structure, so that the pinning effectiveness may shift from one pinning type to another.

4.6 Conclusion

In summary, regular and irregular arrays of extrinsic “defects” in the form of magnetic dots with different shapes and their array configurations can be a powerful tool to hinder vortex motion. The J_c enhancement produced by Fe dot arrays can increase J_c by a factor of up to 2, as well as the enhancement can be observed for both low and high magnetic fields. Modifying the configuration of magnetic dots, with sizes much greater than the coherence length and the penetration depth of YBCO can exploit a range of interactions between vortices, pinning sites, and magnetic flux, with the traps in the form of FM dots and magnetic shielding.

Indeed, we clearly show that magnetic dot arrays affect the J_c behaviour by either increasing and/or decreasing it in a quite dramatically different fashion to non-magnetic (structural) dots, with antidot arrays in similar sizes and shapes. The most striking feature of the influence of magnetic dots on J_c is, its non-monotonous dependence as a function of applied magnetic field, which also reveals that magnetic configurations have the ability to retain J_c enhancement at high fields compared to antidots [136, 138]. Certain commonalities have been observed in samples with various dot arrays, such as more dots and iron, or their concentration in the central area of the superconducting films, which may hint that larger and broader range J_c enhancements are possible. Reducing the separation between adjacent FM dots can result in a crossover from weaker to stronger J_c, although more investigation is needed to examine the behaviour of arrays with size-dependent FM dots. After the driving factors governing certain $\Delta J_c(B_a)$ behaviour are established, a range of potential applications could be considered that require J_c enhancement or even degradation in different field ranges. Possible examples could be power applications, such as current leads for high field magnets, and electronics, where a few vortices may be produce a noise problem associated with vortex/flux movements, so that guiding vortices out of such electronic devices or promoting certain flux localization may be of great benefit.

Chapter 5

Effect of switching the magnetic domain orientation on vortex pinning in the high temperature superconductor $YBa_2Cu_3O_{7-\delta}$ in ferromagnet/superconductor heterostructures system.

5.1 Chapter Outline

This chapter is dedicated to investigating the effect of increasing the thickness of the magnetic components on the flux pinning of a high temperature superconductor in ferromagnet/superconductor heterostructures. This will include examination of the magnetic material in terms of the hysteresis loops behaviour with various layer thicknesses. Also, there will be an investigation of the epitaxial strain in the thin magnetic film at the interface with the substrate (effect on magnetic properties). Characterization will be provided to show the multilayers in these planar superconductor/ferromagnetic hetrostructures. The end of the chapter will include measurements of both magnetization and transport current for the system as a function of applied magnetic field in low and high temperatures. Qualitative research will be conduct to define the behaviour of the critical current density and how it is affected by different magnetic film thicknesses for both approaches.

5.2 Introduction

Coupling a ferromagnet (FM) and superconductor (SC) in a hybrid structure has acquired considerable attention because of the electronic interactions arising from the diffusion-like penetration of Cooper pairs from the superconductor to the ferromagnet, suppressing the superconducting order parameter due to the inverse proximity effect [239, 240] and magnetic interaction via the stray fields emanating from the ferromagnetic layer. The electronic interaction can effectively be controlled and attenuated by certain non-conducting interlayers to avoid Cooper-pair propagation, as long as a thin layer of superconductor near the ferromagnetic layer presumably does not support the flow of current [115]. This means that introducing an insulating layer is required, and thus the electromagnetic interaction would become dominant [241, 242]. The presence of a ferromagnetic material with its domains in FM/SC hybrid systems causes a significant change in the superconducting order parameter, as well as the critical current density (J_c) [243], which is the key point required for more electric-power applications. Vortex pinning in superconductors originates from the spatial modulation of the order parameter on the scale of the coherence length (ξ(T)), as well as of the local magnetic field on the length scale of the London penetration depth (λ(T)). Defect pinning can be introduced into thin films by various routes, producing nano-defects and nano-rods, as well as lithographically defined structures of dots and antidots, which includes arrays of FM dots of various shape and sizes, or intrinsic magnetic domains in ferromagnet/superconductor (F/S) bilayers, multilayers, etc. [207]. The presence of FM features and arrays may result in additional pinning, the so-called magnetic vortex pinning and enhanced critical current densities [207], as long as the suppression of the superconducting order parameter by proximity effects is not overwhelming.

The most distinctive characteristic of magnetic pinning may be its robustness with respect to temperature. This is because such flux pinning acts on the whole vortex rather than on the vortex core alone as in nonmagnetic pinning. The maximal pinning energy per unit length of vortex is the condensation energy of a Cooper pair in the volume of the vortex core: $U= (H_c^2/8\pi)\pi\xi^2 =(\Phi_\circ/8\pi\lambda_L)^2$ where H_c is the critical field, $\Phi_\circ$ is the flux quantum, and ξ, λ_L are the coherence length and London penetration depth, respectively. In high temperatures close to T_c, the pinning energy decreases abruptly due to the increase of ξ and λ_L [207, 244, 245], in agreement with the experimental results, which proved that flux pinning is increased in the F/S system [144, 245, 246], although details of the magnetic domain structure of the FM layer were not investigated. Moreover, the strength of magnetic pinning was estimated to be 100 times larger than the pinning by columnar defects [244], when the issue of vortex pinning enhancements by adjustment magnetic domain structure (out-of-plane magnetic anisotropy) was theoretically addressed in superconductor ferromagnetic multilayers. Therefore, electromagnetic interactions between the vortex and the magnetic microstructure can be easily anticipated in systems with FM dots, magnetic domains topologies, and correlated defects [247]

The hybrid system exhibits a variety of new physical phenomena, such as reverse domain superconductivity and domain wall superconductivity [248]. There is a gradient in the distribution of stray field above each domain, with field magnitude reaching a maximum at the centre of the domain, and below the critical temperature T_c, the expected location to nucleate superconductivity at the minimum stray field is at the domain wall [243]. Furthermore, when an external magnetic field is applied perpendicular to the film, the domains with antiparallel alignment compensate by weakening the applied field above the domain and thus, shift the superconducting nucleus to the centre of the reverse domains. Vortex pinning when the FM materials have in-plane magnetized domains has been also considered [249], and in this case, the domain walls carry enhanced stray field, thus locally suppressing the critical temperature [250]. Enhancement of ~1.5-fold in critical current density at T >50 K has been proven in a system consisting of YBCO and $Pr_{0.67}Sr_{0.33}MnO_3$, in which the FM has an in-plane anisotropy as compared to pure material [145], and the improvement was up to roughly 1.7-fold at a field 3 kOe and even > 2-fold for high temperature. It is unclear, however, why the boundaries of the in-plane magnetized domains improve their pinning efficiency with increasing perpendicular field [250]. One possible explanation could be that the microstructure of the YBCO film was optimized with the implementation of the buffer layer, which could likely enhance the epitaxial growth and create a beneficial defective structure produced by tuned crystal lattice strain at the buffer-film interface [251, 252], although this explanation has little to do with magnetic properties of the FM buffer layer. Furthermore, suppression of superconductivity is very common in system with heterogeneous planar structures. The mechanisms has been proposed in experimental studies of vortex pinning in heterostructures includ, that electronic contact between the superconducting and ferromagnetic layers (conventional proximity effect) exists, where exchange mediated pair breaking leads to strong suppression of the superconductor order parameter [92, 253-

255]. Where epitaxial growth of superconductor was on top of the magnetic material, degradation in the superconductor properties are likely to occur as a results of strain effects at interfaces between layers (lattice mismatch) [251, 252]. In this work, however, the proximity and strain effects are excluded, and thus, superconductor suppression is less prominent. Moreover, studies of the effect of the magnetic layer at high temperature where intrinsic pinning sites are hardly present remain scantly explored.

In general, there are still not enough consistent experimental results that can shed light on the behaviour driven by magnetic stray field interactions and possible magnetic vortex pinning associated with these interactions. In this context, a synthesis of heterostructure composed of, varying thickness of ferromagnetic layers of iron (Fe) with in-plane easy axis magnetization were grown on the surface of an YBCO superconductor layer to investigate the effects of the flux pinning in the superconductor as a function of increasing magnetic component. A thin layer of CeO_2 as an intermediate layer was deposited to suppress the proximity effect. The critical current density of such FM-SC hybrids was measured as a function of the applied magnetic field (B_a) and compared to the host YBCO films before depositing the FM layer. Characterization of the system by transmission electron microscopy (TEM) was applied to disclose the structure. A robust enhancement was observed, particularly for not too thick FM layers at rather high temperatures compared with the pristine YBCO layer. Various scenarios leading to the enhancement that was observed have been discussed.

5.3 Manufacturing procedure forYBCO microwire capped by magnetic material

FM/SC hybrid structures were fabricated by using pulsed laser deposition (PLD) technique for epitaxial growth. A layer of $YBa_2Cu_3O_{7-\delta}$ with thickness > 200 nm was typically grown on single crystal substrate of $SrTiO_3$ (or MgO if specified in the text). The substrate temperature was kept at T_{dep}=780°C during deposition process, with oxygen pressure of 300 mT [256], and then a layer of roughly 10 nm of CeO_2 was deposited *in-situ* as a cap layer on top of the YBCO to avoid any contamination and to make sure that the mutual magnetic interaction between the FM and the SC was dominant rather than the electrical one. The sample was annealed *in-situ* after filling the chamber with O_2 and letting the system cool down at the rate of 400°C in 60 min [256]. The selection of the pulsed laser deposition technique in sample manufacturing was to eliminate droplets and to achieve the extremely smooth and uniform surfaces of the resultant thin films, which are critically significant factors in achieving high quality superlattices [257]. Laser lithography and Ar^+ ion etching were used to define a bridge 30 μm in width and four pads as contacts for current-voltage measurements purposes, where the two outer pads were to deliver the current to the specimen, while the inner contacts were for voltage measurements. Figure 5.1 involve a schematic sketch illustration of the YBCO bridge with four-point probe connections for transport current measurements.

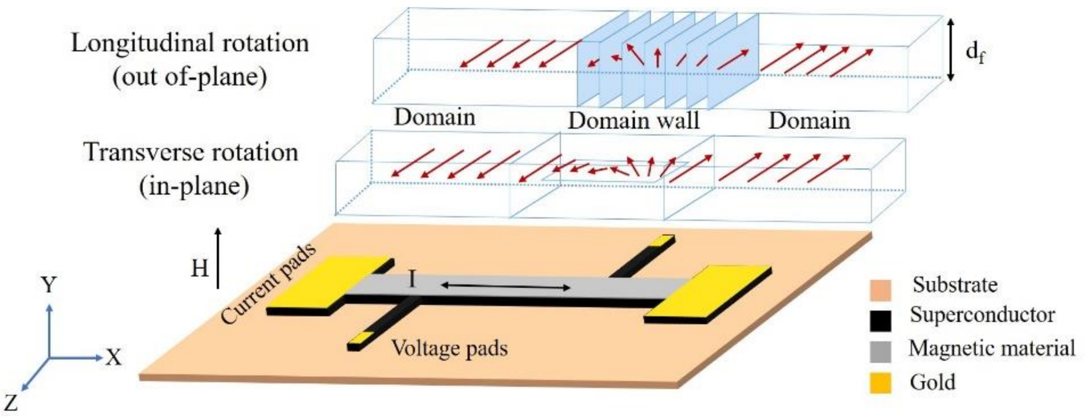

Figure 5.1 *Schematic illustration of sample components, with the overlying ferromagnetic layer showing the domain and domain wall configurations, and how the direction of rotation of the magnetization vector in a domain wall switches from transverse to longitudinal (from in-plane to out-of-plane)for thicker Fe.*

Prior to that, the sample was coated with positive photoresist by using a spin-coater. The entire patterning and etching process was carried out in a clean room environment to ensure that the sample was not contaminated by dust, which might interfere with producing the desire pattern. The cap layer of CeO was removed from the pads by using Layout-Editor for drawing a bridge, and lithography steps in ion-beam etching was used to achieve high contact between the YBCO and the gold (Au) layer, where the latter was deposited on the pad regions only. In addition to that, thin film samples (not patterned with a bridge), both having no iron on top of them and having FM/SC hybrid structures with different thicknesses of iron on top of the YBCO film, were fabricated for magnetization measurement purposes.

Transport and magnetization measurements were performed by using a physical properties measurements system (Quantum Design PPMS) at different temperatures and applied magnetic fields to determine the critical temperature and measure *I-V* curves of the bridge. Measurements were both for comparison purpose and to achieve a better understanding of the influence of Fe on the superconducting properties of YBCO thin films.

Magnetization measurements were implemented at low temperatures, since high temperature weakens superconductor signal so that the signal of the substrate is dominant in the measurement process. On the other hand, transport measurements show a noise signal at low temperature, which restrict experimental measurements to only being close to the critical temperature, where the superconducting system has more potential for application, since most devices require running at high temperatures.

Measurements of the temperature-dependence of magnetic moment at low field in magnetization measurements were performed to determine the T_c and quality of sample in zero field-cooling, where the sample is cooled down to 5K with no applied field, and then a certain value of field is applied. Zero-field-cooling curves were acquired by measuring the moment as a function of increasing temperature to over T_c.

The next step involved deposition of roughly > 100 nm Fe which had an in-plane magnetic anisotropy at room temperature on the entire YBCO bridge, including the side walls of the structure. It is worth noting that there was no contact between the Fe layer and the Au on the pads (to make sure that applied current was only passing through the superconductor sample, which is the intrinsic point of the research), a space was left of 25 μm between both of them. This space was determined using the programme Layout-Editor that was used to draw the pattern of the bridge. Figure 5.2 present optical microscope images showing the microstructure of the system.

Magnetization hysteresis loops measurements of Fe films deposited directly on $SrTiO_3$ substrates with similar thicknesses to those deposited on top of YBCO films were performed utilizing the reciprocating sample option (RSO) in the Quantum Design MPMS XL SQUID magnetometer. The measurements were conducted for both magnetic field orientations: applied in-plane and out-of-plane for the Fe film for comparison.

Cross-sectional transmission electron microscope (TEM) samples were prepared using the *in-situ* lift-out focused ion beam technique and were studied using an FEI Tecnai F20 field emission TEM operated at 200 keV. TEM was also combined with energy dispersive X-Ray Analysis and elemental mapping imaging (TEAM-EDAX), which was used to analyse the inter diffusion of the elements between the layers on the FM/SC interface. TEM images also assisted in verifying the thicknesses of all deposited layers, which were otherwise determined by the pre-calibrated deposition rate. Optical microscopy was also used to evaluate the topography of surfaces with a Nikon polarizing microscope (Eclipse LV100).

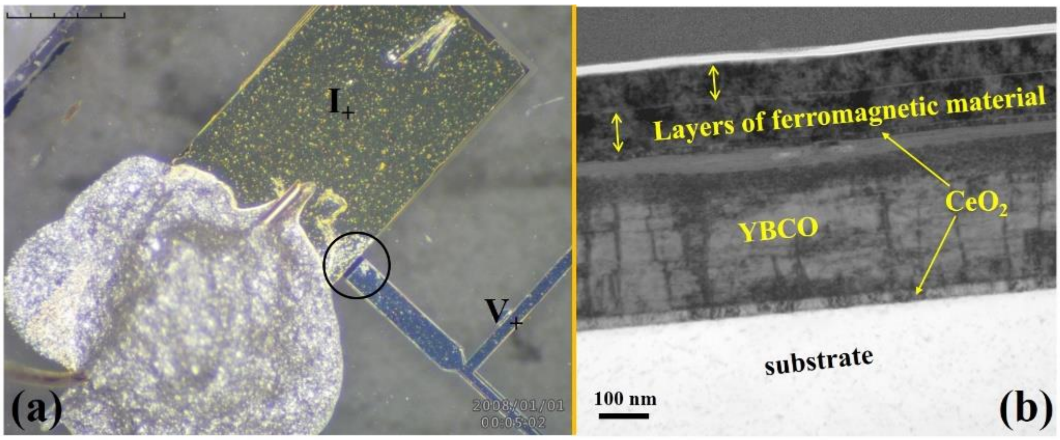

Figure 5.2 *a) Optical microscope of the typical sample geometry showing the space between the gold layer on pads and the iron layers in the four-point probe approach , b) cross sectional TEM image, showing the layers constituting the bridge.*

5.4 Results and discussion

5.4.1 Sample characterization

Low-magnification cross-sectional images were conducted to investigate the structure of the YBCO bridges fabricated by TEM. The thicknesses of all layers can be identified from the TEM image in Figure 5.2(b), including its buffer CeO_2 layers, deposited Fe layers, and substrate. In this particular case the substrate was MgO with a CeO_2 buffer layer deposited on top of the substrate to ensure better epitaxial growth than on a non-buffered MgO substrate. This was because there is a larger misfit between the relevant crystal lattice parameters of YBCO and MgO than between those of YBCO and CeO_2.

Here, we should note that the structure in Figure 5.2(b) possess two identically deposited Fe layers ~ 100 nm thick. The second layer of Fe was deposited on top of the first layer after all the desired measurements with one Fe layer were completed. This was done to enable a comparison of the observed behaviour between the identically prepared samples possessing different thicknesses of the FM layer, as will be discussed in more detail below.

Figure 5.2(b) reveals that there is an obvious thin layer about 5 nm thick between the two deposited layers of Fe. This is most likely the result of iron oxidation during measurements and handling of the sample with the first iron layer only. This was confirmed by the tiny peak in Figure 5.3(b) upon TEAM-EDAX analysis corresponding to oxygen increase compared to the neighbouring pure Fe region.

Figure 5.2(b) also shows clusters of threading edge dislocations forming a chain of domain walls in the YBCO layer, which were produced by the PLD technique for epitaxial thin film growth, and generally originate due to the mismatch between the crystal lattice parameters of the substrate and those of the YBCO thin film [258, 259], although in this particular case, we have a CeO_2 buffer layer (also visible between the MgO substrate and the YBCO film). Under certain conditions these columnar defects can provide effective pinning sites for vortices with their well-developed quantitative pinning mechanism able to explain $J_c(B_a)$ over the entire magnetic field range [10, 69, 260, 261]. Figure 5.2(a) is a sample image captured by optical microscope that shows the pads for current injection to the bridge, connected with a golden wire, and voltage pads for measuring the resistance on both ends of the bridge. It also shows that there is a gap between the magnetic layer and the golden pads to ensure that current passes only through the superconductor.

A thin layer about 40 nm thick at the top of YBCO film and underneath the CeO_2 cap layer that is shown in Figure 5.2(b) deserve special mention. It is supposed to be YBCO, but quite obviously its microstructure and likely crystallinity are notably degraded due to reactivity with the Fe layer even through the protective cap provided by the CeO_2 layer. The evidence of deterioration due to inter-diffusion during the deposition process and likely oxidation afterwards comes from the TEAM-EDAX analysis shown in Figure 5.3 (b). Near the interface with CeO_2, which can be identified by the onset of the Ce-peak (yellow line) at about 170 nm, a notable degradation of the Cu (pink line) and Ba (orange line) constituents can be seen, starting at about 195 nm. On the other hand, Fe (dark green line) can be detected up to 180-185 nm. It is also worthwhile noting that the thickness of the deteriorated YBCO layer near the CeO_2 capping interface is about a factor of 2 thinner than can be assumed from the inter diffusion of elements, as identified by TEAM-EDAX analysis. As shown below, however, this deterioration was not overwhelming compared to the benefits achieved with the FM/SC structure after Fe deposition.

In addition, Figure 5.3 shows the elements composition for the entire Fe/YBCO hybrid thin film structure. It can be observed that the constituent elements for YBCO (Y, Ba, Cu and O) are more apparent in the mapping images followed by the Fe-layers, and all are dispenser homogeneously in the thin film structure. Furthermore, the images in Figure 5.3 confirm the spatial distributions of constituent elements and their distributions for YBCO, Fe, and CeO_2, as well as the results of their reactivity at the oxide and metallic interface. Oxidation between the first and the second Fe-layer deposition can also be observed.

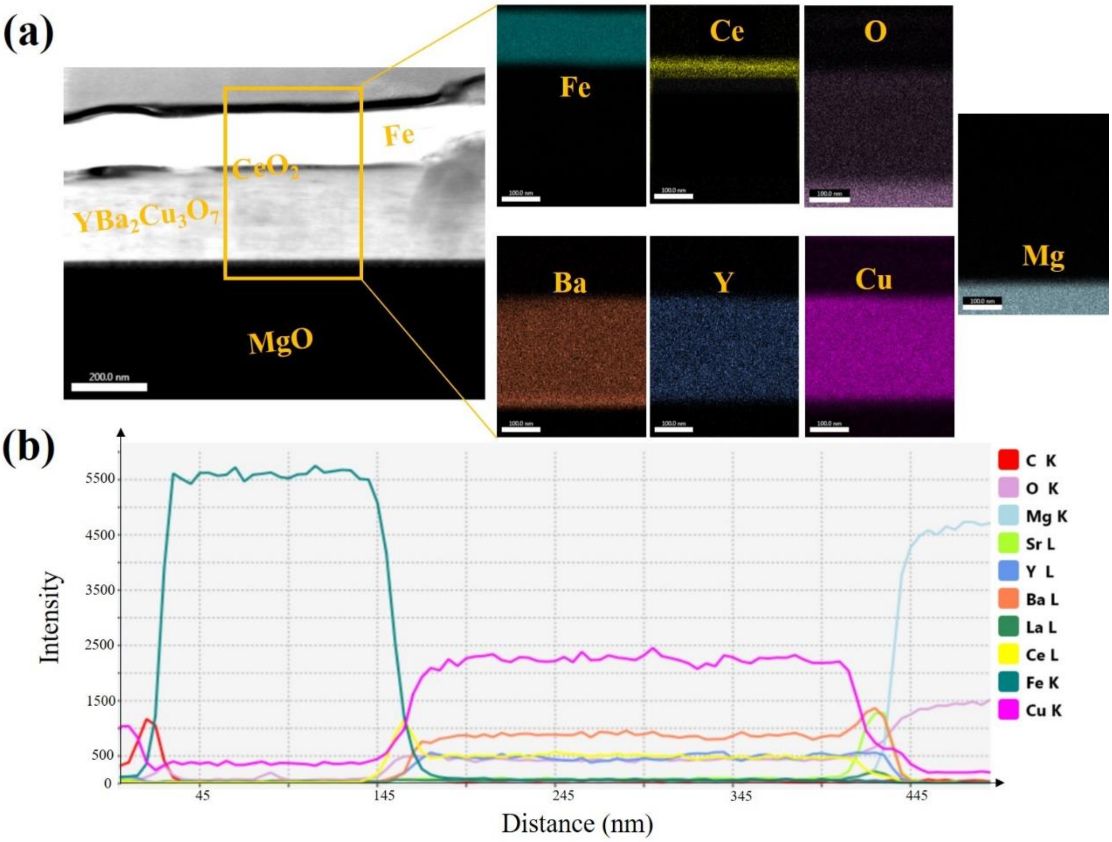

Figure 5.3 *a) TEAM and EDAX mapping analysis, b) element profile plot for thin film bridge constituents (intensity for region of interest versus distance).*

Afterwards, magnetic characterization of the magnetic film component was conducted, where a magnetization hysteresis loops were performed to investigate thin film magnetic properties utilizing the RSO in the MPMSXL SQUID. In this option, there are a rapid oscillations of the sample by a rotary actuator around the centre point of the pickup coils, which gives an accurate reading. Magnetic hysteresis loops are presented in Figure 5.4 for both Fe layers (~100 nm and ~ 200 nm) deposited directly on a $SrTiO_3$ substrate without an YBCO superconducting film. The magnetic film thickness is based on the time of deposition, while the rest of deposition parameters were kept constant. The Fe layer thickness was confirmed by a slot pattern applied on the magnetic film by laser lithography followed by an etching process down to substrate. The thickness of film was determined with a Dektak profilometer.

The hysteresis loops in Figure 5.4(a, b) reveal apparent differences for the two thicknesses of the film. In the case of the coercive field, which is the reverse applied field required to reduce magnetization to zero after the material has been saturated, it is obvious that the film with a low magnetic component has a wider hysteretic loop (higher coercivity) than the thick film, which was about 0.1 T at 10 K and about 0.05 T at 77 K, while the thicker film has a coercive field of about 0.005 T for both temperatures. This is attributed to spin reorientation of the magnetic moment at domain walls in response to the magnetic field sweep, where in the film with thickness > 100 nm, the flipping takes place in-plane (Néel walls) in contrast to the film with thickness > 200 nm (Bloch walls) with less density of domain walls as it becomes wider (since the easiest track for magnetic moment rotation is out-of-plane rather than in-plane). Moreover, it was observed that the epitaxial strain effect induced by the substrate in thin films at interfaces might produce substantial effects on various aspects of the film, including structural and physical properties, and not just in terms of the magnetic properties of thin magnetic films [262]. Whereas, increasing magnetic film thickness result in strain relaxation. Furthermore, the results show that the thicker film has irreversible behaviour above the conventionally defined coercivity up to about 0.4 T for both temperatures, which could be due to the oxidation of the initially deposited layer of Fe because of handling and measurements. This oxidation was measured for the thicker film because the oxidation was not extensive enough to be detected by the time of the measurements for the thinner film. Hence, the irreversibility does not appear for thinner film.

In addition, the findings show an anisotropic magnetic response, i.e., the hysteresis loops behave differently in the cases of *H*//*c* and *H*//*ab* in Figure 5.4(c), where the magnetic signal demonstrate that the easy axis magnetization is aligned in-plane for the Fe film, as expected. A significant difference in the value of magnetic saturation was observed from the hysteresis loops between transverse and longitudinal applied field, as shown in the inset of Figure 5.4(b), where both magnetic field orientations show a larger saturation field of about 2 T for *H*//*c*, and only about 0.1 T in the case of *H*//*ab*.

This comparison is of particular importance for measurement of the FM/SC structure because the field has always been applied out-of-plane. The results above show that the Fe films would reach full saturation only at 2 T in this orientation, which means that they would preserve the shielding effect up to this field.

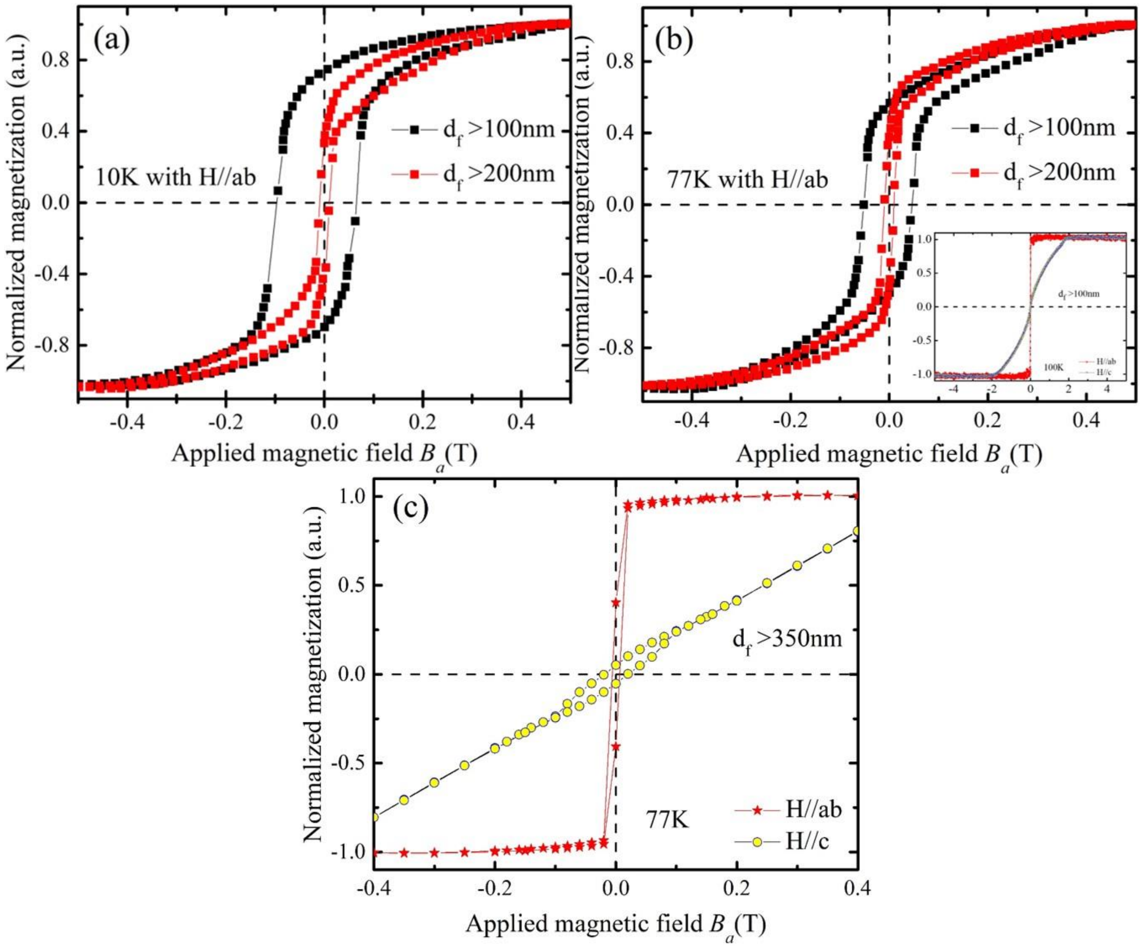

Figure 5.4 *Magnetization hysteresis loops at different temperatures for several Fe films with varying thickness: (a) and (b) show that increasing the magnetic film thickness is accompanied by switching the magnetic moment of domain walls from in-plane (Néel domain walls) to out of-plane (Bloch domain walls), (c) hysteresis loop magnetization measurements (100 K in the inset)for magnetic film with more than 350nm thickness in field applied perpendicular and parallel to the film plane, showing the easy axis orientation to magnetize this material.*

5.4.2 Quality and homogeneity of sample structures

Regarding the electromagnetic measurements, typical behaviour curves of electrical resistivity versus temperature for different applied magnetic fields for bilayer and as-grown films are shown in Figure 5.5. Transport measurements using PPMS allow measurement of the resistivity as temperature is increased from below T_c to above it. The sample is cooled down in zero applied field (ZFC) to temperature down to 75 K, and by applying a certain value of current through the bridge and ramping the temperature progressively to 95 K, we can determine the value of T_c in which the curve starts to transition from the normal to the superconducting state ($T_{c\,\mathrm{onset}}$), as shown in Figure 5.5(a). Magnetisation vs. temperature (M-T) curves in corresponding magnetization measurements, however, took place in ZFC from 10 K up to 100 K, as shown in Figure 5.5(b). In addition, the superconducting transition width ΔT_c can be estimated by the criterion of 10%–90% ρ_n, where ρ_n is the resistivity in the normal state just above the transition [263], as indicated in Figure 5.5(d). A striking result is that the onset of the superconducting transition for YBCO can be identify at T_c ~ 90.8 K at zero field, and this transition increased for the bilayer to about 92.5 K (Figure 5.5(a)). That is an almost a 2 K increase, which is in stark contrast to the T_c suppression expected as a result of suppression of the superconducting order parameter due to possible proximity effects. The T_c enhancement is also in contrast to some previous reports that revealed a reduction in T_c [149, 253, 262].

Furthermore, after doubling the thickness of the Fe layer to about 200 nm, the onset of T_c experienced only an insignificant reduction of about 0.5 K (Figure 5(a)). Although it has still exhibited a T_c higher than that for the YBCO film without the Fe layer.

On the other hand, the resistive transition width ΔT for the FM/SC bilayer exhibit a broadening of the resistive curve of 1.3 K, 0.2 K lower than for the as-grown film, in a high magnetic field such as 2.5 T, although it shows a smaller zero field transition width of about 0.4 K. The broadening of the transition curve in higher applied magnetic field arises from thermal dissipation as a result of vortex motion due to thermal activation at lower temperatures because of the increased number of vortices [264], and it is remarkable that the ΔT value increases with magnetic film thickness. In M-T curves, however, the broadening in the magnetization curve is unnoticeable, as there is no real current flowing in the sample.

Another notable result is tha the corresponding magnetization measurements of an as-grown YBCO film and then the same film with 100 nm and 200 nm thick Fe-layers deposited on it hardly showed any difference in the behaviour of the T_c transition for these three types of structures (Figure 5.5(b)). The difference between the results of the resistance and magnetization measurements could be either due to inherent differences in the measuring techniques used or due to the geometrical configuration of the FM/SC structure, and hence due to different ways in which the FM layer interacts with the superconducting film.

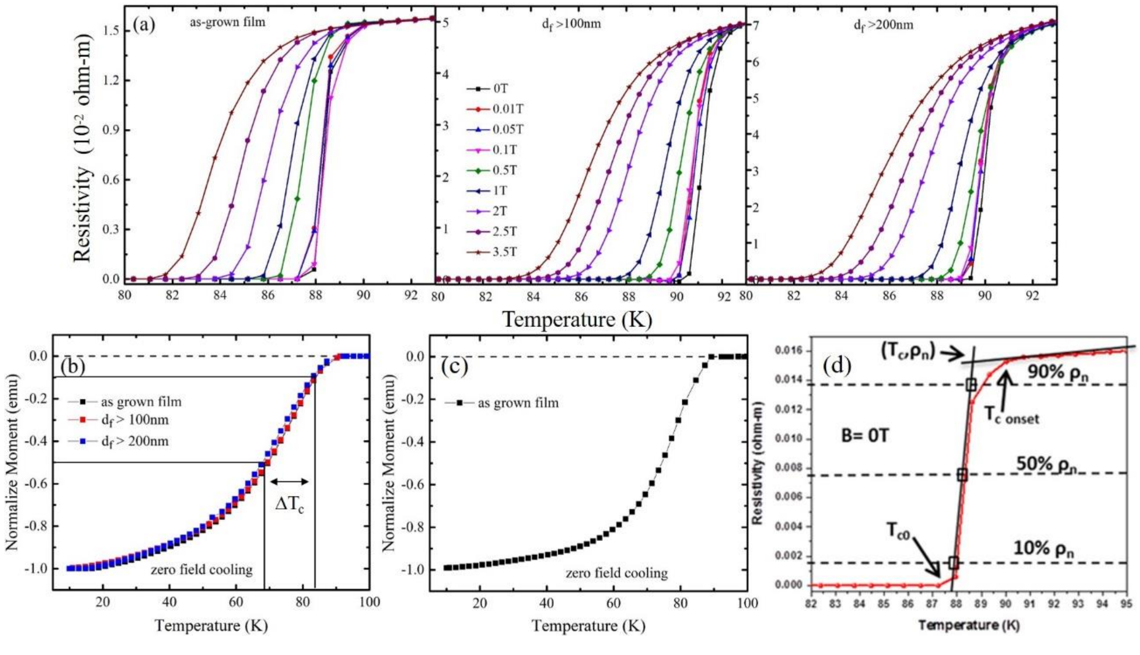

Figure 5.5 *a) Temperature dependence of the resistivity (ρ) at various applied magnetic fields of pure YBCO bridge and YBCO bridge with different thicknesses of iron d_f >100, 200 nm respectively, (b, and c) normalized magnetization measurement as a function of T during warm-up process for sample in 100 Oe applied parallel to c-axis of YBCO, (d) the approach applied to determine the critical temperature T_c for a superconductor. A line has been drawn in the normal state and at transition region of the resistive curve (R-T), where the intersection gives the T_c and ρ_n. Dotted lines parallel to T-axis at 90%, 50% and 10% of ρ_n with the corresponding T_c values at the intersection point shown as a box. This approach can be applied to deduce T_c values under applied magnetic fields [263].*

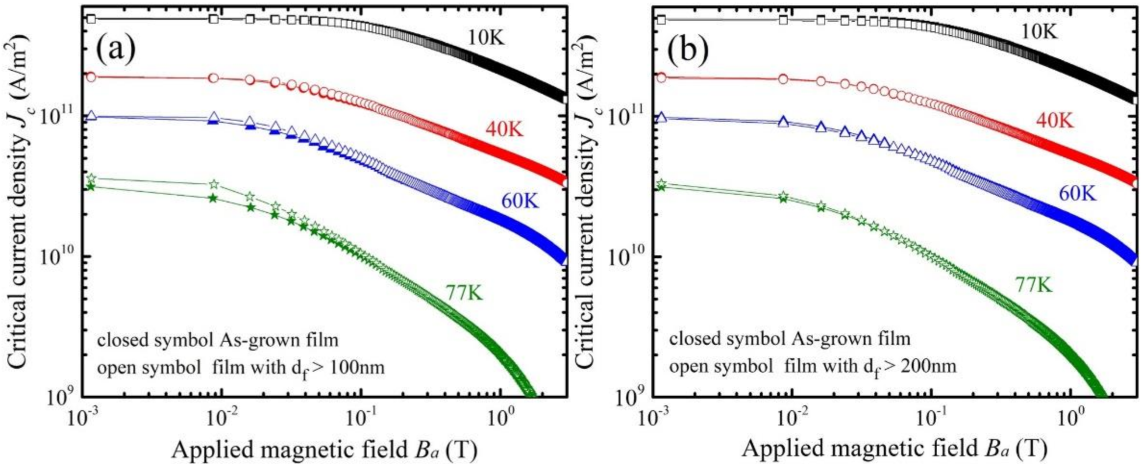

***Figure 5.6** Critical current density for as-grown YBCO film and film after a series of deposition processes for the magnetic component at several given temperatures: (a) for a thin Fe layer and (b) for a thick Fe layer.*

5.4.3 Planar superconductor/ferromagnetic heterostructure in magnetization measurements

To give a clear perception of the flux pinning performance of a superconductor, it is essential to highlight its critical current density behaviour and its dependence on applied magnetic field and temperature, as shown in Figure 5.6 in the log-log scale for a sample, where J_c has been extracted from the corresponding magnetization loop measurements.

It is observed from the curves for as-grown and multilayer films that they do not show much difference in their critical current density values at low temperature. At zero applied field, the J_c for a multilayer film achieved 4.8×10^{11} A.m^{-2}, which is 10% less than for the as-grown film. The difference in J_c between the curves seems to increase, however, with rising temperature. Figure 5.7 reveal a clear $\Delta J_c/J_c^{\text{as-grown}}$ dependence on the thickness of the magnetic component at several given temperatures, where $\Delta J_c = J_c^{bilayer} - J_c^{as\text{-}grown}$. The J_c for a given sample has been extracted from magnetic hysteresis loops measured for film prior to (plain film) and post deposition of magnetic layers. According to the modified critical state model [70, 76], the critical current density can be expressed as:

$$J_c = 2\Delta M / \left[W_p\left(1-\frac{W_p}{3L_p}\right)\right] \qquad 5.1$$

Where W_p and L_p are the width and length of the sample, respectively, where $\Delta M(B_a, T) = |M^+|+|M^-|$ is the width of magnetization hysteresis loop between ascending and descending magnetic field. The main feature of these curves is that flux pinning is weak or absent at low temperature, in agreement with previous experiments [253, 262, 265]. The magnetic strip domains are play a significant role in vortex channelling, as the latter has a length scale dependence on temperature compared to the domain size, and thus facilitates flux propagation in the YBCO sample. Degradation in the critical state no longer exists, however, when the temperature is increased, as it is obvious from Figures 5.6 and 5.7(a) that the highest flux pinning was achieved at 77 K.

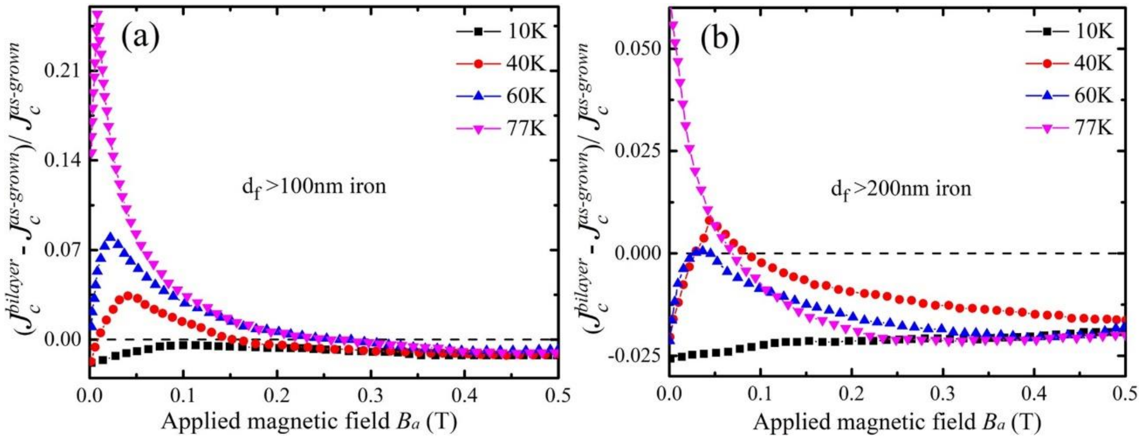

Figure 5.7 *Relative change in critical current density as a function of applied magnetic field for planar heterostructure system with thinner and thicker magnetic components, a) and b), respectively.*

Another notable feature is that J_c enhancement occurs at rather low magnetic fields < 0.3 T for the FM/SC hybrid structure with the 100 nm thick Fe-layer, and < 0.1 T for the structure with the 200 nm thick Fe-layer, but only above ~ 60 K. This enhancement experiences a maximum after sharply rising from zero applied magnetic field and then fall off more gradually after peaking.

On the other hand, modulation in flux pinning can be observed in Figure 5.6 and 5.7(b), and it is clear that superconductivity is more effective at low field (77 K), even when domain wall moments flipped from in-plane to out of-plane as the magnetic film becomes thicker. It was found that the strength of the stray field at domain walls was much stronger for out-of-plane compared to in-plane components as a result of expansion in the domain walls region for the thick magnetic film. It is apparent from Figure 5.8 that the domain wall region (region marked with black line) in panel (b) is more pronounced than that in panel (a) [149]. This scenario explains the minimum in critical current density behaviour at low temperature compared to highest one occurring at 77 K, where the domain size matches the vortex length scale [48].

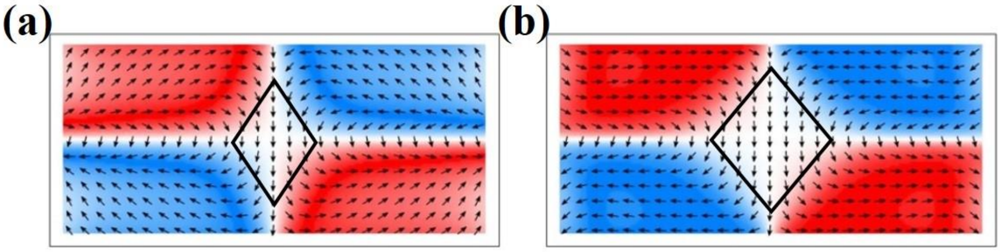

Figure 5.8 *Images showing the domain structure in a nickel thin film a) 20 and b) 100nm thick, taken by 3D objected oriented micromagnetic framework (OOMMF) simulation at a field near the coercive value [149].*

The curves in Figure 5.7 are also characterized by a jump followed by a sharp decreas in behaviour of the $\Delta J_c/J_c$, as the low field-$\Delta J_c/J_c$ follows the hysteresis loop for the magnetic thin film. The maximum of the superconducting state is achieved at roughly the coercive field where the maximum density of domain walls would be expected. In contrast, when the magnetic film is in the saturated state, it behaves as a single domain, i.e., less pinning of flux. It is worth noting that in this sample an edges effect is present, where the scratches and grooves at the edges of the sample allow vortices to penetrate more readily and thus weaken the superconducting state [266].

5.4.4 Transport characteristic in planar superconductor/ferromagnetic heterostructure wire

The previous behaviour of J_c has indicated that flux pinning can be achieved at high temperature and even with an increasing amount of magnetic component. Therefore, this subsection will focus on the electrical transport measurements in high temperature, which is not easy to implement in magnetization measurements. Furthermore, at high temperatures close to T_c, spontaneous flux penetration is more likely to occur, even at low field, because H_{c1} for thin film superconductors is reduced with increasing temperature [148], since the lower critical field can be expressed as:

$$H_{c1}(0K) = \emptyset_{\circ}/4\pi\lambda(0K)^2 ln\left[\frac{\lambda(0K)}{\xi(0K)}\right] \qquad 5.2$$

Where λ and ξ are the penetration depth and coherence length, respectively, at zero temperature, and both of them depend on the ambient temperature.

Figure 5.9 shows the current-voltage curve and its dependence on temperature and applied magnetic field for a typical (YBCO) bridge, as well as for the corresponding FM/SC hybrid structures obtained by depositing 100 nm and 200 nm thick layers on top of YBCO films capped by a thin layer of CeO_2. The I_c was derived, and calculations have been applied using the formula $I_c = J_c \times S$ (where S is the cross-sectional area of the bridge). If a current is injected into the bridge below the critical value and in the superconducting state, no voltage will be recorded, as there is no dissipation in the flowing current. With increasing applied current, however, the voltage will manifested evidently, as visualized in Figure 5.9, which shows the bending in the curve after its linear behaviour. Arguably, the wire has been switched from the dissipation-free to the resistive state for current flow. Therefore, I_c has been determined to be the value of the applied transport current at which the voltage increases above 0.001 mV, also the distance between the inner voltage contacts has an effect on the measured voltage value.

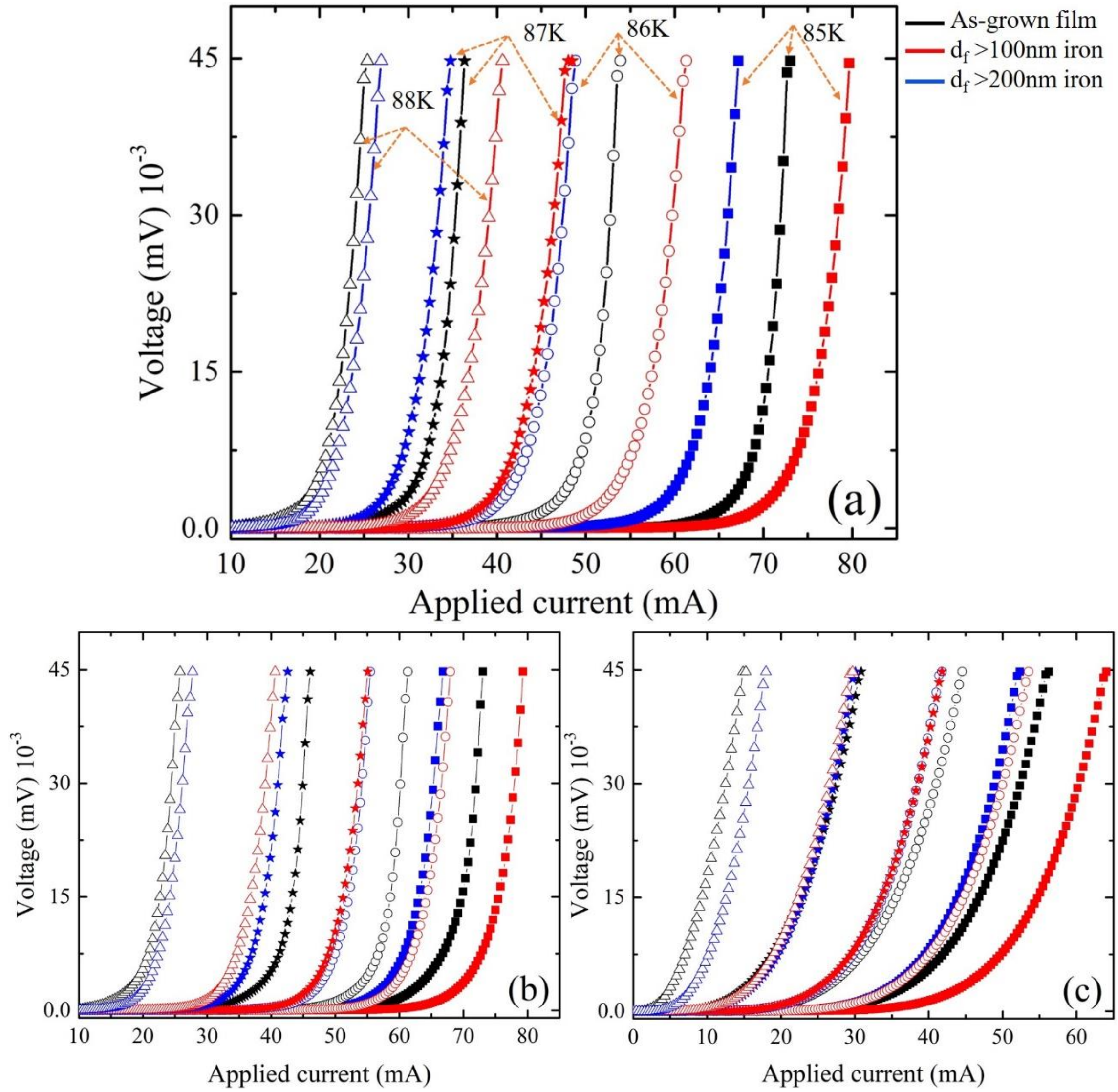

Figure 5.9 *I-V curves in electrical transport mode for YBCO micro-wire prior and post deposition with a magnetic layer of varying thickness at given temperatures and zero applied field (self-field) (a), at 5 mT (b) and at 100 mT (c).*

The curves in Figure 5.10(b) are characterized by a low-field plateau where J_c is independent of applied magnetic field and remains relatively constant, followed by rapid decay at high magnetic fields. This is actually a common feature of all epitaxial high-temperature superconducting films [267], and arises from the interaction between the ferromagnet and the superconductor [87], in contrast with the as-grown film with no magnetic layer. A crossover between the J_c for FM/SC heterostructures and the YBCO film can also be observed, with J_c of the heterostructures being higher than that for the YBCO film at low magnetic fields and vice versa at higher magnetic fields.

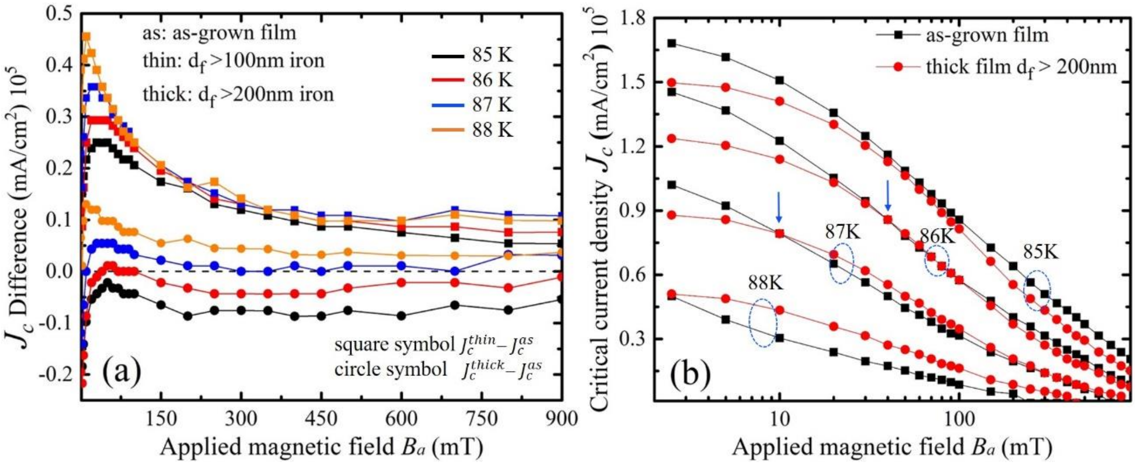

Figure 5.10 *a) Field dependence of the critical current density difference for bilayer bridges, with the J_c values extracted from the I-V curves. b) Evolution of the crossover behaviour of J_c-H curves as a function of ambient temperature for the plain film and the film with > 200 nm of iron.*

It is obvious from Figure 5.10(a) that the J_c differences are significantly larger for the bilayer with ~100 nm thick ferromagnetic material than for the YBCO films with ferromagnetic layer ~200 nm thick over the entire range of accessible temperatures. Moreover, at relatively low fields, the differences in critical current become more pronounced at elevated temperatures, which then gradually degrade at higher applied fields. It is clearly shown from the curve of differences between J_c for bilayers (~100 nm Fe) and the as-grown film in Figure 5.10(a) that the maximum difference is at the temperature of 88 K. This behaviour is remarkably similar to the behaviour and trend exhibited by the $J_c(B_a)$, measured with the help of magnetization measurements, as shown in Figure 5.7. It is worth noting that separating iron from YBCO by a CeO_2 capping layer not only protects both materials from degrading due to chemical reactions and proximity effects, but also rules out any possibility of any microstructure modifications for YBCO superconducting films. Indeed, in our case, the microstructure was unaffected by the combination with the ferromagnetic layer, whereas in other works [246, 254, 268], the superconductor was deposited on the top of the ferromagnetic material, which could lead to beneficial microstructure enhancements, which are well documented for multilayered structures.

Such enhancement can be directly attributed to the increas in the interactions between the flux and the magnetic domain structure from increasing the temperature [145]. Therefore, the enhanced flux pinning will become more appreciable. The interaction between the flux and the domain structure can be explained with more precision. Below the critical temperature and at zero applied field, the ferromagnet is magnetized by self-field as a consequence of current flow in the superconductor in the x-direction, while the stray field emanating from magnetic domains that have in-plane anisotropy (multidomain configuration), as depicted by the red arrows in Figure 5.1, suppresses superconductivity locally below the domain walls due to the high density of flux lines (interaction of vortices with the domain walls), unlike from the regions neighbouring the domain walls. Put differently, the vortices are trapped at domain walls where the maximum spin disorder exists, which gives the lowest energy state [145], so domain walls require an extra driving force to facilitate their movement. When applying magnetic field perpendicular to the film plane, the magnetization process is dominated by rotation of the magnetization vector out of plane rather than domain wall movement (to minimize magnetostatic energy), as is obvious from the curves of critical current densities and their dependences on temperature and magnetic field. Note that the highest density of flux lines is on the sides of the bridge, so a compensation effect can exist on one edge of the bridge, depending on the polarity of the current. As mentioned before, the interaction between the flux and the magnetic domain structure becomes more important at elevated temperature, so it is straightforward that the temperature effect on domain structure will cause expansion with decreasing T (decreasing domain wall area) and vice versa [127], so this promotes the number of vortices interacting with domain walls, which explains the high difference in J_c at elevated temperature. Moreover, J_c in the as grown film, which has only pinning by structural defects, decreases with temperature as $\lambda_L^{-2}(T)$ α $(T_c - T)$ [244], which is another reason for the enhancement of the gap in values between a film with a ferromagnetic layer and an as-grown film at high temperature. On increasing the applied magnetic field close to the coercivity field, most domains rotate their orientation to agree with the external field, i.e., increase the monodomain region at the expense of domain walls, so vortices start to move freely. By increasing the thickness of the ferromagnetic layer (sample with > 200 nm thickness), the stripe domain width is made to expand, and the domain wall density is decreased, resulting in weaker pinning, in agreement with a report on CoFeB deposited on top of YBCO, where the YBCO with the thin sample of CoFeB showed the highest difference in critical current density close to the critical temperature [115]. The change in the magnetic domain structure and its influence on the properties of the superconductor were investigated by D. Mancusi et al. [146], and the results showed that the pinning strength for a larger thickness of the ferromagnetic layer in the Py/Nb system, where Py is permalloy, was found to be lower than for the sample with a thinner Py layer. Moreover, when magnetic force microscopy imaging was performed at room temperature to determine the domain structure of the Py films, the images showed that average stripe domain width decreased with reduced thickness of the permalloy. The striking feature in Figure 5.10(b) at high temperature is the crossover behaviour in J_c-H curves for the sample with a ferromagnetic layer > 200 nm thick was observed, and it is more likely to occur at intermediate field and more apparent at high temperature, which implies that additional strong pinning centres are present [269]. The crossing field shifts from high magnetic field to low field at 86 K and disappears at 88 K, in agreement with C. Z. Chen et al. [265]. Furthermore, at temperatures close to T_c, the thicker sample in Figure 5.10(b) outperforms the as-grown film over the entire applied magnetic field range, which is compatible with the higher T_c value in the former case relative to the as-grown film. The vortices are influenced by magnetic inhomogeneity on the length scale of the London penetration depth λ_L, and the magnetic pinning reaches its maximum when domain size and λ_L match [48]. This scenario explains the occurrence of the crossing field in the sample with thicker ferromagnetic material. The J_c behaviour was confirmed by Figure 5.10(a, b), which shows the critical current density-magnetic field dependence and the differences in J_c for the bilayer (> 200 nm Fe) and as-grown films. Whereas, the J_c curve in (a) starts to ramp up from a negative value up to a positive value with increasing temperature (where positive and negative value in J_c difference indicate that J_c has been enhanced or reduced, respectively), and in (b) the arrows in the curves are indicate to crossover points.

Another obvious feature to note in the FM/SC system is the strengthening in J_c enhancement at high temperatures. This is likely to occur due to weakening of the inherent natural pinning of the YBCO film, which is governed by its microstructure. At high temperature, the magnetic pinning, which is unaffected by the temperature, can overwhelm the strong microstructural pinning, and as a result, effectively contribute to the overall pinning that is observed.

5.5 Conclusion

In summary, planer heterostructures of YBCO superconductor and a magnetic material were successfully prepared by using pulsed laser deposition and were of good quality according to critical temperature resulta for the samples. TEM images indicated that the substrate induced strain effect on the YBCO layer due to the lattice mismatch between them was prohibited, and thus, no suppression of superconductivity could be observed, although an intermedate layer at the top of the YBCO film was induced as a result of inter diffusion during the deposition process even with the presence of a buffer layer.

Magnetic characterization of magnetic layers (~100 nm and ~200 nm) overlying superconductor thin films revealed that, iron has an easy axis and in-plane magnetic anisotropy, as it is shows linear behaviour in its hysteresis loop when the applied magnetic field is parallel to magnetic film plane. Furthermore, an examination of the thin and thick magnetic films indicated that a transition in the magnetic moments for domain walls had occurred, where the larger magnitude of the coercive field for the thin film as compared to the thicker one was clear in the magnetization loops.

Magnetization and transport measurements for planar heterostructures strongly emphasized that magnetic pinning is more effective at elevated temperature. Furthermore, the modulation of flux pinning exists where there is a narrow strip geometry (domain walls), where it is possible for the transverse magnetic moment to rotate. Suppression of superconductivity with switching of the magnetic moment in thicker magnetic film has been identified at lower temperature, but supereconductivity has been recovered when both the vortex length scale and the magnetic domains are matched at a temperature where thermal fluctuations are more pronounced.

The differences in critical current density showed that the thin magnetic layers in planar FM/SC heterostructures outperformed the thicker ones over the whole magnetic field range. A collapse in pinning strength for the thicker ferromagnetic layer was noticed, however, because the lower domain boundary density in the ferromagnetic film produced a weaker interaction between the moving vortices and those trapped at domain walls. The breakdown in flux pinning was no longer present with increasing temperature of the sample medium, where the crossover effect became more dominate

Chapter 6

6.1 Thesis conclusion and recommendations

In summary, different arrays with large magnetic dots that have dimensions much greater than the coherence length and the penetration depth have been manufactured and investigated in high quality YBCO thin films. This is in contrast to vast majority of arrays with small dot dimensions of $\sim \xi$ that have been considered to date. It was shown that regular and irregular arrays of artificial "defects" in the form of these magnetic dots with different shapes and their array configurations can be a powerful tool to hinder vortex motion. The J_c enhancement produced by Fe dot arrays can enhance J_c by a factor of up to 2. The enhancement can be observed for both low and high magnetic fields. Modifying the configuration of magnetic dots enables a range of interactions between vortices and intrinsic (natural) pinning sites, and between magnetic flux and its traps in the form of FM dots, as well as the effects of magnetic shielding. This work clearly shows that magnetic dot arrays affect the J_c behaviour in a quite remarkably different way to non-magnetic arrays, with similar sizes and shapes of antidot arrays.

A most striking feature of the magnetic dot influence on J_c is its non-monotonic dependence as a function of applied magnetic field, which also reveals that magnetic configurations have the ability to retain J_c enhancement at high fields.

In contrast, antidots (lithographically shaped perforations in YBCO films) show enhancement or degradation in a very monotonic way, with stronger enhancement/degradation in low fields, which decreases in high magnetic fields. Depending on their shapes and array configurations, tuneable J_c enhancement is present in all types of non-uniform antidot arrays, with the strongest effect being up to 20% in graded and inverted arrays over the entire applied magnetic field range.

In contrast to magnetic dot arrays, for which explanations for the somewhat unpredictable behaviour of J_c enhancements are based on simple empirical factors, the antidot behaviour can be explained more plausibly. The "vortex vacuum" pinning model has been suggested to account for this enhancement with non-Bean-like magnetic flux penetration leading to the formation of "vortex vacuum" regions created by the rings of antidots. These regions occur because of vortex pinning along the edges of the individual antidots and repulsive vortex-vortex interactions creating vortex jams (or bottlenecks) for the conventional Bean-like vortex arrangements.

In the case of magnetic dots, certain commonalities have still been observed in samples with various dot arrays and have been analysed to provide some guidance for future research. (i) More dots and iron, as well as a higher concentration of iron in the central region of the superconducting films suggests a larger and broader range of J_c enhancements.

(ii) Reducing the separation between adjacent FM dots results in a crossover from lower to higher J_c as a function of the applied magnetic field.

More investigations are needed, however, to examine the behaviour of arrays with size-dependent FM dots. After the driving factors governing certain $\Delta J_c(B_a)$ behaviour are established, a range of potential applications could be considered that requiring J_c enhancement or even degradation in different field ranges. Possible examples could be power applications, such as current leads for high field magnets, and electronics, where a few vortices may be a problem because they produce noise associated with vortex/flux movements, so guiding vortices out of such electronic devices or establishing a certain amount of flux localization may be of great benefit.

Combining YBCO thin films with Fe films in the form of bilayer heterostructures has enabled a range of interesting and reproducible results. One of the most remarkable results is the significant enhancement of critical temperature by more than 2 K by simply depositing a 100 nm thick iron layer on top of the YBCO thin films. This result was only slightly modified by doubling the thickness of the iron layer. This T_c increase shows that the combination of two antagonistically ordered systems, one with the ferromagnetic spin order and the other with electrons in the form of Cooper pairs having opposite spins, so as to enable Bose-Einstein condensation and hence superconductivity, can together produce an enhancement to superconducting properties. This was only possible, however, if the structures were separated by a thin layer of non-magnetic and insulating CeO_2 materials, which prevented any possible order-suppressing proximity effects.

In addition, the hybrid bilayer also enabled J_c enhancement over the magnetic field range, which is somewhat consistent with the sharp remagnetisation in the iron layer. This remagnetisation occurs due to magnetic anisotropy of the Fe film, which has its easy magnetization axis in-plane of the film, while the magnetic field upon J_c measurements was applied out-of-plane. Upon this remagnetising event, the vortices experience an additional magnetic-like pinning due to the huge permeability in this field range. Notably, this magnetic-like pinning becomes more effective as the temperature increases. This is in agreement with the theory proposing that magnetic pinning is temperature independent, while natural pinning on structural defects gradually loses its effectiveness due to thermal activation. This explains the J_c enhancement at high temperatures.

Lastly, it is worthwhile to point out that the second generation of superconducting HTS YBCO tapes (the so-called coated conductors) can be manufactured on magnetic templates. Hence, the results obtained suggest that the magnetic property of the template can be converted into a beneficial factor rather than diminishing a problem.

Overall, this work has produced novel results useful for electronics for critical current manipulations, as well as for electricity handling, generation, and transmission, due to the enhancement of the critical current density.

Publications

- Al-Qurainy, M., et al., Large artificial ferromagnetic dot arrays for the critical current enhancement in superconducting $YBa_2Cu_3O_{7-\delta}$ thin films. Superconductor Science and Technology, 2020. 33(10): p. 105006.

- Jones, A., et al., Dominant factors for the pinning enhancement by large artificial partial and complete antidots in superconducting films. Superconductor Science and Technology, 2020. 33(3): p. 035004.

- George, J., et al., Tunable pinning effects produced by non-uniform antidot arrays in YBCO thin films. Annalen der Physik, 2017. 529(4): p. 1600283.

- Al-Qurainy, M., et al., The switching effect in magnetic domain moment orientation on vortex pinning at high temperature superconductor $YBa_2Cu_3O_{7-\delta}$ shielded by ferromagnetic material in heterostructure system, submitted to Phys Rev B (2022).

References

1. Larbalestier, D., et al., *High-Tc superconducting materials for electric power applications*, in *Materials For Sustainable Energy: A Collection of Peer-Reviewed Research and Review Articles from Nature Publishing Group*. 2011, World Scientific. p. 311-320.

2. Tolpygo, S.K., *Superconductor digital electronics: Scalability and energy efficiency issues.* Low Temperature Physics, 2016. **42**(5): p. 361-379.

3. M.M. Awang Kechik, R.A.-S., S.A. Halim and A. Masrianis., *Transport Critical current density of* $(Bi_{1.6}Pb_{0.4})Sr_2Ca_2Cu_3O_\delta$ *superconductor by* Fe_3O_4 *addition.* J. Solid St. Sci. and Technol. Lett., 2006. **13**(1): p. 232-236.

4. Matsumoto, K. and P. Mele, *Artificial pinning center technology to enhance vortex pinning in YBCO coated conductors.* Superconductor Science and Technology, 2009. **23**(1): p. 014001.

5. Kwok, W.-K., et al., *Vortices in high-performance high-temperature superconductors.* Reports on Progress in Physics, 2016. **79**(11): p. 116501.

6. Tixador, P., et al., *Quench in bulk HTS materials - Application to the fault current limiter.* Superconductor Science and Technology, 2000. **13**(5): p. 493.

7. Li, B., et al., *Materials process and applications of single grain (RE)–Ba–Cu–O bulk high-temperature superconductors.* Physica C: Superconductivity, 2012. **482**: p. 50-57.

8. Buckel, W. and R. Kleiner, *Superconductivity: Fundamentals and applications*. 2008: John Wiley & Sons.

9. Chong, I., et al., *High Critical-Current Density in the Heavily Pb-Doped* $Bi_2Sr_2CaCu_2O_{8+\delta}$ *Superconductor: Generation of Efficient Pinning Centers.* Science, 1997. **276**(5313): p. 770-773.

10. Pan, V., et al., *Supercurrent transport in* $YBa_2Cu_3O_{7-\delta}$ *epitaxial thin films in a dc magnetic field.* Physical Review B, 2006. **73**(5): p. 054508.

11. Huijbregtse, J., et al., *Vortex pinning by natural defects in thin films of* $YBa_2Cu_3O_{7-\delta}$. Superconductor Science and Technology, 2002. **15**(3): p. 395.

12. Hylton, T. and M. Beasley, *Flux-pinning mechanisms in thin films of* YBa_2Cu_3O *x.* Physical Review B, 1990. **41**(16): p. 11669.

13. Daeumling, M., J. Seuntjens, and D. Larbalestier, *Oxygen-defect flux pinning, anomalous magnetization and intra-grain granularity in* $YBa_2Cu_3O_{7-\delta}$. Nature, 1990. **346**(6282): p. 332.

14. Crisan, A., et al., *Sputtered nanodots: A costless method for inducing effective pinning centers in superconducting thin films.* Applied Physics Letters, 2001. **79**(27): p. 4547-4549.

15. Baert, M., et al., *Composite flux-line lattices stabilized in superconducting films by a regular array of artificial defects.* Physical Review Letters, 1995. **74**(16): p. 3269.

16. Schuster, T., et al., *Enhancement of critical current densities by heavy-ion irradiation in* $YBa_2Cu_3O_{7-\delta}$ *observed using the high-resolution Faraday effect.* Physical Review B, 1993. **47**(1): p. 373.

17. Pan, A.V., S. Pysarenko, and S.X. Dou, *Drastic improvement of surface structure and current-carrying ability in* $YBa_2Cu_3O_7$ *films by introducing multilayered structure.* Applied Physics Letters, 2006. **88**(23): p. 232506.

18. Milošević, M., et al., *Guided nucleation of superconductivity on a graded magnetic substrate.* Applied Physics Letters, 2010. **96**(3): p. 032503.

19. Del Valle, J., et al., *Superconducting/magnetic three-state nanodevice for memory and reading applications.* Scientific Reports, 2015. **5**: p. 15210.

20. Feldmann, D.M., et al., *Grain orientations and grain boundary networks of* $YBa_2Cu_3O_{7-\delta}$ *films deposited by metalorganic and pulsed laser deposition on biaxially textured Ni–W substrates.* Journal of Materials Research, 2006. **21**(04): p. 923-934.

21. Aloysius, R.P., P. Guruswamy, and U. Syamaprasad, *Highly enhanced critical current density in Pr-added (Bi, Pb)-2212 superconductor.* Superconductor Science and Technology, 2005. **18**(5): p. L23.

22. Clarke, J., H. Weinstock, and R. Ralston, *The new superconducting electronics.* H. Weinstock & RW Ralston (Eds.), The new superconducting electronics, 1993: p. 123.

23. Castellanos AM, W.R., Ockenfuss G, A. v.d. Hart, Keck K., Appl. Phys. Lett., 1997. **71**(962).

24. de Souza Silva, C.C., J.A. Aguiar, and V. Moshchalkov, *Linear ac dynamics of vortices in a periodic pinning array.* Physical Review B, 2003. **68**(13): p. 134512.

25. Savel'Ev, S. and F. Nori, *Experimentally realizable devices for controlling the motion of magnetic flux quanta in anisotropic superconductors.* Nature Materials, 2002. **1**(3): p. 179.

26. Hänggi, P. and F. Marchesoni, *Artificial Brownian motors: Controlling transport on the nanoscale.* Reviews of Modern Physics, 2009. **81**(1): p. 387.

27. Jones, A., et al., *Dominant factors for the pinning enhancement by large artificial partial and complete antidots in superconducting films.* Superconductor Science and Technology, 2020. **33**(3): p. 035004.

28. Poole Jr, C.P., H. Farach, and R. Creswick, *Superconductivity* New York. 1995, California: Academic Press. 154.

29. Doss, J.D., *Engineer's guide to high-temperature superconductivity*. 1989, New York, Wiley-Interscience. 471.

30. Meissner, W. and R. Ochsenfeld, *Ein neuer effekt bei eintritt der supraleitfähigkeit.* Naturwissenschaften, 1933. **21**(44): p. 787-788.

31. Kasap, S.O., *Principles of electronic materials and devices*. 3rd ed. 2006, New York, USA: McGraw-Hill.

32. London, F. and H. London, *The electromagnetic equations of the supraconductor.* Proceedings of the Royal Society of London. Series A-Mathematical and Physical Sciences, 1935. **149**(866): p. 71-88.

33. London, H., *Phase-equilibrium of supraconductors in a magnetic field.* Proceedings of the Royal Society of London. Series A-Mathematical and Physical Sciences, 1935. **152**(877): p. 650-663.

34. Tinkham, M., *Introduction to Superconductivity*. 2nd ed. 1996: Dover Publications. 454.

35. Gennes, P.D., *Superconductivity Of Metals And Alloys*. 1999: Advanced Book Program, Perseus Books. 274.

36. V.Ginzburg, L.L., *Ginzburg–Landau theory of phase transitions*. Vol. 20. 1950, New York: Pergamon press.

37. Müller, P., A.V. Ustinov, and V. Schmidt, *The physics of superconductors. Introduction to fundamentals and applications.* 1997.

38. Bardeen, J., L.N. Cooper, and J.R. Schrieffer, *Theory of superconductivity.* Physical Review, 1957. **108**(5): p. 1175.

39. Müller, P., A.V. Ustinov, and V. Schmidt, *The physics of superconductors. Introduction to fundamentals and applications*. 1997, New York: Berlin, Heidelberg: Springer Berlin / Heidelberg. 217.

40. Gómez Gutiérrez, A., *Magnetic control of superconducting vortices. Control magnético de vórtices superconductores*. 2014, Universidad Complutense de Madrid.

41. Tinkham, M., *Introduction to superconductivity*. 1996: Courier Corporation.

42. Wu, M.-K., et al., *Superconductivity at 93 K in a new mixed-phase Y-Ba-Cu-O compound system at ambient pressure.* Physical Review Letters, 1987. **58**(9): p. 908.

43. Tallon, J.L., et al., *High-Tc superconducting phases in the series* $Bi_{2.1}(Ca, Sr)_{n+1}Cu_nO_{2n+4+\delta}$. Nature, 1988. **333**(6169): p. 153-156.

44. Cooper, S., K. Gray, and D. Ginsberg, *Physical Properties of High Temperature Superconductors IV.* World Scientific, 1994.

45. *Coalition for comercial application of superconductors*. 2011; Available from: http://www.ccas-web.org/superconductivity/.

46. Rouco Gómez, V., *Controlling Vortex Pinning and Dynamics of Nanostructured YBCO Thin Films Grown by Chemical Solution Deposition*. 2014: Universitat Autònoma de Barcelona.

47. Cyrot, M. and D. Pavuna, *Introduction to superconductivity and high-Tc materials*. 1992: World Scientific.

48. Blatter, G., et al., *Vortices in high-temperature superconductors.* Reviews of Modern Physics, 1994. **66**(4): p. 1125.

49. Homes, C., et al., *Coherence, incoherence, and scaling along the c-axis of* $YBa_2Cu_3O_{6+x}$. Physical Review B, 2005. **71**(18): p. 184515.

50. Varshney, D., R. Singh, and S. Shah, *Coherence lengths and magnetic penetration depths in* $YBa_2Cu_3O_7$ *and* $YBa_2Cu_4O_8$ *superconductors.* Journal of Superconductivity, 1996. **9**(6): p. 629-635.

51. Norton, D., *Science and Technology of high temperature superconducting films1.* Annual Review of Materials Science, 1998. **28**(1): p. 299-347.

52. Jorgensen, J., et al., *Structural properties of oxygen-deficient* $YBa_2Cu_3O_{7-\delta}$. Physical Review B, 1990. **41**(4): p. 1863.

53. Miu, L., et al., *Vortex unbinding and layer decoupling in epitaxial* $Bi_2Sr_2Ca_2Cu_3O_{10+\delta}$ *films.* Physical Review B, 1995. **52**(6): p. 4553.

54. Van Bael, M.J., et al., *Vortex pinning in ferromagnet/superconductor hybrid structures.* Physica C: Superconductivity, 2001. **364–365**: p. 491-494.

55. Foltyn, S., et al., *Materials science challenges for high-temperature superconducting wire.* Nature Materials, 2007. **6**(9): p. 631.

56. Larkin, A. and Y.N. Ovchinnikov, *Pinning in type II superconductors.* Journal of Low Temperature Physics, 1979. **34**(3-4): p. 409-428.

57. Pan, A.V., et al., *Multilayering and Ag-Doping for Properties and Performance Enhancement in* $YBa_2Cu_3O_7$ *Films.* IEEE Transactions on Applied Superconductivity, 2007. **17**(2): p. 3585-3588.

58. Pan, A., et al., *Enhancing Properties of High-Temperature Superconducting Step-Edge Josephson Junctions by Nano-Multilayers with a Small Mismatch.* Advanced Materials Interfaces, 2014. **1**(3): p. 1300112.

59. Mele, P., et al., *Ultra-high flux pinning properties of* $BaMO_3$*-doped* $YBa_2Cu_3O_{7-x}$ *thin films (M= Zr, Sn).* Superconductor Science and Technology, 2008. **21**(3): p. 032002.

60. MacManus-Driscoll, J., et al., *Strongly enhanced current densities in superconducting coated conductors of* $YBa_2Cu_3O_{7-x}$*+* $BaZrO_3$. Nature Materials, 2004. **3**(7): p. 439.

61. Matsushita, T., et al., *The effect of heavy ion irradiation on the critical current density in DyBCO coated conductors.* Superconductor Science and Technology, 2008. **21**(5): p. 054014.

62. Silhanek, A.V., et al., *Enhanced vortex trapping by a composite antidot lattice in a superconducting Pb film.* Physica C: Superconductivity, 2007. **460–462, Part 2**: p. 1434-1435.

63. Baca, F., et al., *Control of* $BaZrO_3$ *nanorod alignment in* $YBa_2Cu_3O_{7-x}$ *thin films by microstructural modulation.* Applied Physics Letters, 2009. **94**(10): p. 2512.

64. Abrikosov, A.A., *On the magnetic properties of superconductors of the second group.* Soviet Physics JETP, 1957. **5**: p. 1174-1182.

65. Polyanskii, A., et al., *Examination of current limiting mechanisms in monocore* $Bi_2Sr_2Ca_2Cu_3O_x$ *tape with high critical current density.* IEEE Transactions on Applied Superconductivity, 2001. **11**(1): p. 3269-3272.

66. Hilgenkamp, H. and J. Mannhart, *Grain boundaries in high-T_C superconductors.* Reviews of Modern Physics, 2002. **74**(2): p. 485.

67. Dew-Hughes, D., *The critical current of superconductors: An historical review.* Low Temperature Physics, 2001. **27**(9): p. 713-722.

68. Lang, W., et al., *Depairing current and superconducting transition of YBCO at intense pulsed currents.* physica status solidi (c), 2005. **2**(5): p. 1615-1624.

69. Pan, V. and A. Pan, *Vortex matter in superconductors.* Low Temperature Physics, 2001. **27**(9): p. 732-746.

70. Pan, A.V., I. Golovchanskiy, and S. Fedoseev, *Critical current density: Measurements vs. reality.* EPL (Europhysics Letters), 2013. **103**(1): p. 17006.

71. Golovchanskiy, I., et al., *Rectifying differences in transport, dynamic, and quasi-equilibrium measurements of critical current density.* Journal of Applied Physics, 2013. **114**(16): p. 163910.

72. Golovchanskiy, I.A., et al., *Vibration effect on magnetization and critical current density of superconductors.* Superconductor Science and Technology, 2016. **29**(7): p. 075002.

73. Schwartzkopf, L., et al., *The use of the in-field critical current density, J_c (0.1 T), as a better descriptor of (Bi, Pb)$_2$Sr$_2$Ca$_2$Cu$_3$O$_x$/Ag tape performance.* Applied Physics Letters, 1999. **75**(20): p. 3168-3170.

74. Bean, C.P., *Magnetization of hard superconductors.* Physical Review Letters, 1962. **8**(6): p. 250.

75. Yeshurun, Y., A. Malozemoff, and A. Shaulov, *Magnetic relaxation in high-temperature superconductors.* Reviews of Modern Physics, 1996. **68**(3): p. 911.

76. Campbell, A. and J. Evetts, *Flux vortices and transport currents in type II superconductors.* Advances in Physics, 1972. **21**(90): p. 199-428.

77. Kittel, C., *Physical theory of ferromagnetic domains.* Reviews of Modern Physics, 1949. **21**(4): p. 541.

78. Spaldin, N.A., *Magnetic Materials: Fundamentals and Applications*. 2nd ed. 2010: Cambridge University Press.

79. Michael E.McHenry, D.E.L., *Physical Metallurgy (19 - Magnetic Properties of Metals and Alloy)*. 5th ed. Vol. 1. 2015: Elsevier BV.

80. Qiu, F., et al., *Correlating non-linear behavior of in-plane magnetic field and local domain wall velocities for quantitative stress evaluation.* AIP Advances, 2019. **9**(1): p. 015325.

81. Patino, E.J., C. Bell, and M.G. Blamire, *Sudden critical current drops induced in S/F structures.* The European Physical Journal B, 2009. **68**(1): p. 73-77.

82. Carapella, G., F. Russo, and G. Costabile, *Low-field transport measurements in superconducting Co/Nb/Co trilayers.* Physical Review B, 2008. **78**(10): p. 104529.

83. Hsieh, C., J. Liu, and J. Lue, *Magnetic force microscopy studies of domain walls in nickel and cobalt films.* Applied Surface Science, 2005. **252**(5): p. 1899-1909.

84. Löhndorf, M., et al., *Structure of cross-tie wall in thin Co films resolved by magnetic force microscopy.* Applied Physics Letters, 1996. **68**(25): p. 3635-3637.

85. Methfessel, S., S. Middelhoek, and H. Thomas, *Domain walls in thin Ni-Fe films.* IBM Journal of Research and Development, 1960. **4**(2): p. 96-106.

86. Pan, A.V., S. Zhou, and S. Dou, *Iron-sheath influence on the superconductivity of MgB_2 core in wires and tapes.* Superconductor Science and Technology, 2004. **17**(5): p. S410.

87. Horvat, J., et al., *Improvement of critical current in MgB_2/Fe superconducting wires by a ferromagnetic sheath.* Applied Physics Letters, 2002. **80**(5): p. 829-831.

88. Aladyshkin, A.Y., et al., *Domain-wall superconductivity in hybrid superconductor-ferromagnet structures.* Physical Review B, 2003. **68**(18): p. 184508.

89. Yang, Z., et al., *Domain-wall superconductivity in superconductor–ferromagnet hybrids.* Nature Materials, 2004. **3**(11): p. 793.

90. Baibich, M.N., et al., *Giant magnetoresistance of (001)Fe/(001)Cr magnetic superlattices.* Physical Review Letters, 1988. **61**(21): p. 2472.

91. Dagotto, E., *Complexity in strongly correlated electronic systems.* Science, 2005. **309**(5732): p. 257-262.

92. Buzdin, A.I., *Proximity effects in superconductor-ferromagnet heterostructures.* Reviews of Modern Physics, 2005. **77**(3): p. 935.

93. Robinson, J., et al., *Zero to π transition in superconductor-ferromagnet-superconductor junctions.* Physical Review B, 2007. **76**(9): p. 094522.

94. Piano, S., et al., *0-π oscillations in nanostructured Nb/Fe/Nb Josephson junctions.* The European Physical Journal B, 2007. **58**(2): p. 123-126.

95. Robinson, J., et al., *Enhanced supercurrents in Josephson junctions containing nonparallel ferromagnetic domains.* Physical Review Letters, 2010. **104**(20): p. 207001.

96. Keizer, R., et al., *A spin triplet supercurrent through the half-metallic ferromagnet CrO_2.* Nature, 2006. **439**(7078): p. 825-827.

97. Robinson, J., J. Witt, and M. Blamire, *Controlled injection of spin-triplet supercurrents into a strong ferromagnet.* Science, 2010. **329**(5987): p. 59-61.

98. Khaire, T.S., et al., *Observation of spin-triplet superconductivity in Co-based Josephson junctions.* Physical Review Letters, 2010. **104**(13): p. 137002.

99. Klose, C., et al., *Optimization of spin-triplet supercurrent in ferromagnetic Josephson junctions.* Physical Review Letters, 2012. **108**(12): p. 127002.

100. Anwar, M., et al., *Long range supercurrents in ferromagnetic CrO_2 using a multilayer contact structure.* Applied Physics Letters, 2012. **100**(5): p. 052602.

101. Robinson, J., et al., *Supercurrent enhancement in Bloch domain walls.* Scientific Reports, 2012. **2**(1): p. 1-6.

102. Gingrich, E., et al., *Spin-triplet supercurrent in Co/Ni multilayer Josephson junctions with perpendicular anisotropy.* Physical Review B, 2012. **86**(22): p. 224506.

103. Halász, G.B., M. Blamire, and J. Robinson, *Magnetic-coupling-dependent spin-triplet supercurrents in helimagnet/ferromagnet Josephson junctions.* Physical Review B, 2011. **84**(2): p. 024517.

104. Witt, J., J. Robinson, and M. Blamire, *Josephson junctions incorporating a conical magnetic holmium interlayer.* Physical Review B, 2012. **85**(18): p. 184526.

105. Usman, I., et al., *Evidence for spin mixing in holmium thin film and crystal samples.* Physical Review B, 2011. **83**(14): p. 144518.

106. Linder, J. and J.W. Robinson, *Superconducting spintronics.* Nature Physics, 2015. **11**(4): p. 307-315.

107. Eschrig, M., *Spin-polarized supercurrents for spintronics.* Phys. Today, 2011. **64**(1): p. 43.

108. Bergeret, F., A.F. Volkov, and K.B. Efetov, *Odd triplet superconductivity and related phenomena in superconductor-ferromagnet structures.* Reviews of Modern Physics, 2005. **77**(4): p. 1321.

109. Blamire, M. and J. Robinson, *The interface between superconductivity and magnetism: Understanding and device prospects.* Journal of Physics: Condensed Matter, 2014. **26**(45): p. 453201.

110. Przyslupski, P., et al., *Structure and magnetic characterization of* $La_{0.67}Sr_{0.33}MnO_3/YBa_2Cu_3O_7$ *superlattices.* Journal of Applied Physics, 2004. **95**(5): p. 2906-2911.

111. Fedoseev, S.A., *Investigation of Superconducting Thin Films and Multilayered Structures for Electronic Applications,.* 2014, University of Wollongong,: Australia.

112. Yonamine, A.H., et al. *Magnetic properties of YBCO/LCMO superlattices with and without STO interlayers*. in *Advanced Materials Research*. 2014. Trans Tech Publications Ltd, Switzerland.

113. Masilamani, N., et al., *Effect of Substrate and Buffer Layer Materials on Properties of Thin* $YBa_2Cu_3O_{7-x}$ *Films.* IEEE Transactions on Applied Superconductivity, 2013. **23**(3): p. 6601105-6601105.

114. Malmivirta, M., et al., *A Structural Optimization of Ferrite/YBCO Bilayers.* IEEE Transactions on Applied Superconductivity, 2016. **27**(4): p. 1-5.

115. Stahl, C., et al., *Using magnetic coupling in bilayers of superconducting YBCO and soft-magnetic CoFeB to map supercurrent flow.* EPL (Europhysics Letters), 2014. **106**(2): p. 27002.

116. Giapintzakis, J., et al., *Production and identification of flux-pinning defects by electron irradiation in* $YBa_2Cu_3O_{7-x}$ *single crystals.* Physical Review B, 1992. **45**(18): p. 10677.

117. Civale, L., et al., *Defect independence of the irreversibility line in proton-irradiated Y-Ba-Cu-O crystals.* Physical Review Letters, 1990. **65**(9): p. 1164.

118. Van Dover, R., et al., *Critical currents near* 10^6 Acm^{-2} *at 77 K in neutron-irradiated single-crystal* $YBa_2Cu_3O_7$. Nature, 1989. **342**(6245): p. 55.

119. Sauerzopf, F., et al., *Neutron-irradiation effects on critical current densities in single-crystalline* $YBa_2Cu_3O_{7-\delta}$. Physical Review B, 1991. **43**(4): p. 3091.

120. Civale, L., et al., *Vortex confinement by columnar defects in* $YBa_2Cu_3O_7$ *crystals: Enhanced pinning at high fields and temperatures.* Physical Review Letters, 1991. **67**(5): p. 648.

121. Roas, B., et al., *Effects of 173 MeV* ^{129}Xe *ion irradiation on epitaxial* $YBa_2Cu_3O_x$ *films.* EPL (Europhysics Letters), 1990. **11**(7): p. 669.

122. Christen, D., et al. *Orientation-dependent critical currents in* $Y_1Ba_2Cu_3O_{7-x}$ *epitaxial thin films: Evidence for intrinsic flux pinning*. in *AIP Conference Proceedings*. 1991. American Institute of Physics.

123. Haugan, T., et al., *Addition of nanoparticle dispersions to enhance flux pinning of the* $YBa_2Cu_3O_{7-x}$ *superconductor.* Nature, 2004. **430**(7002): p. 867.

124. Baert, M. and V. Metlushko, *Jonckheere. R., Moshchalkov, VV, and Bruynseraede, Y.: Composite Flux-Line Lattices Stabilized in Superconducting Films by a Regular Array of Artificial Defects.* Phys. Rev. Lett, 1995. **74**: p. 3269.

125. Jones, A., et al., *Enhancing the critical current of* $YBa_2Cu_3O_7$ *thin films by substrate nanoengineering.* Journal of Applied Physics, 2018. **124**(23): p. 233905.

126. de Lara, D.P., et al., *Vortex lattice motion in the flux creep regime on asymmetric pinning potentials.* Superconductor Science and Technology, 2013. **26**(3): p. 035016.

127. Vlasko-Vlasov, V., et al., *Domain structure and magnetic pinning in ferromagnetic/superconducting hybrids.* Physical Review B, 2012. **85**(6): p. 064505.

128. Jan, D., et al., *Flux pinning enhancement in ferromagnetic and superconducting thin-film multilayers.* Applied Physics Letters, 2003. **82**(5): p. 778-780.

129. Raedts, S., et al., *Flux pinning properties of holes and blind holes arranged periodically in a superconductor.* Physica C: Superconductivity, 2004. **404**(1-4): p. 298-301.

130. Gheorghe, D.G., et al., *Anisotropic avalanches and flux penetration in patterned superconductors.* Physica C: Superconductivity and its Applications, 2006. **437**: p. 69-72.

131. Wang, Y.-L., et al., *Enhancing the critical current of a superconducting film in a wide range of magnetic fields with a conformal array of nanoscale holes.* Physical Review B, 2013. **87**(22): p. 220501.

132. Kemmler, M., et al., *Commensurability effects in superconducting Nb films with quasiperiodic pinning arrays.* Physical Review Letters, 2006. **97**(14): p. 147003.

133. Montero, M., O. Stoll, and I.K. Schuller, *Mechanisms of periodic pinning in superconducting thin films.* The European Physical Journal B-Condensed Matter and Complex Systems, 2004. **40**(4): p. 459-462.

134. Villegas, J., et al., *A superconducting reversible rectifier that controls the motion of magnetic flux quanta.* Science, 2003. **302**(5648): p. 1188-1191.

135. Motta, M., et al., *Enhanced pinning in superconducting thin films with graded pinning landscapes.* Applied Physics Letters, 2013. **102**(21): p. 212601.

136. George, J., et al., *Tunable pinning effects produced by non-uniform antidot arrays in YBCO thin films.* Annalen der Physik, 2017. **529**(4): p. 1600283.

137. Wördenweber, R., *Engineering of superconductors and superconducting devices using artificial pinning sites.* Physical Sciences Reviews, 2017. **2**(8).

138. Jones, A., et al., *Changing the Critical Current Density and Magnetic Properties of* $YBa_2Cu_3O_7$ *by Using Large Antidots.* IEEE Transactions on Applied Superconductivity, 2018. **28**(4): p. 1-5.

139. Wang, Y., et al., *Enhancing superconducting critical current by randomness.* Physical Review B, 2016. **93**(4): p. 045111.

140. Misko, V. and F. Nori, *Magnetic flux pinning in superconductors with hyperbolic-tessellation arrays of pinning sites.* Physical Review B, 2012. **85**(18): p. 184506.

141. Bean, C.P., *Magnetization of high-field superconductors.* Reviews of Modern Physics, 1964. **36**(1): p. 31.

142. Bulaevskii, L., E. Chudnovsky, and M. Maley, *Magnetic pinning in superconductor-ferromagnet multilayers.* Applied Physics Letters, 2000. **76**(18): p. 2594-2596.

143. Huang, J. and H. Wang, *Effective magnetic pinning schemes for enhanced superconducting property in high temperature superconductor* $YBa_2Cu_3O_{7-x}$*: A review.* Superconductor Science and Technology, 2017. **30**(11): p. 114004.

144. Garcıa-Santiago, A., et al., *Enhanced pinning in a magnetic-superconducting bilayer.* Applied Physics Letters, 2000. **77**(18): p. 2900-2902.

145. Zhang, X., et al., *Enhanced flux pinning in a high-*T_C *superconducting film by a ferromagnetic buffer layer.* EPL (Europhysics Letters), 2001. **56**(1): p. 119.

146. Mancusi, D., et al., *Magnetic pinning in a superconducting film by a ferromagnetic layer with stripe domains.* Superconductor Science and Technology, 2014. **27**(12): p. 125002.

147. Huang, J., et al., *Magnetic* $(CoFe_2O_4)_{0.1}$ $(CeO_2)_{0.9}$ *nanocomposite as effective pinning centers in* $FeSe_{0.1}Te_{0.9}$ *thin films.* Journal of Physics: Condensed Matter, 2015. **28**(2): p. 025702.

148. Patiño, E.J. and M. Blamire, *Sudden magnetization drops in superconductor/ferromagnet bilayered structures.* Superconductor Science and Technology, 2018. **32**(1): p. 01LT02.

149. Bhatia, E., et al., *Domain wall induced modulation of low field HT phase diagram in patterned superconductor-ferromagnet stripes.* AIP Advances, 2019. **9**(4): p. 045107.

150. Montero, M., et al., *Flux pinning by regular nanostructures in Nb thin films: Magnetic vs. structural effects.* EPL (Europhysics Letters), 2003. **63**(1): p. 118.

151. Hoffmann, A., P. Prieto, and I.K. Schuller, *Periodic vortex pinning with magnetic and nonmagnetic dots: The influence of size.* Physical Review B, 2000. **61**(10): p. 6958-6965.

152. Hoffmann, A., et al., *Superconducting Vortex Pinning with Magnetic Dots: Does Size and Magnetic Configuration Matter?* Journal of Superconductivity and Novel Magnetism, 2012. **25**(7): p. 2187-2191.

153. Martın, J., et al., *Fabrication of submicrometric magnetic structures by electron-beam lithography.* Journal of Applied Physics, 1998. **84**(1): p. 411-415.

154. Villegas, J., et al., *Vortex-lattice dynamics with channeled pinning potential landscapes.* Physical Review B, 2005. **72**(6): p. 064507.

155. Villegas, J., et al., *Directional vortex motion guided by artificially induced mesoscopic potentials.* Physical Review B, 2003. **68**(22): p. 224504.

156. Martin, J.I., et al., *Artificially induced reconfiguration of the vortex lattice by arrays of magnetic dots.* Physical Review Letters, 1999. **83**(5): p. 1022.

157. Silhanek, A., et al., *Tunable pinning in superconducting films with magnetic microloops.* Applied Physics Letters, 2006. **89**(18): p. 182505.

158. Silhanek, A., et al., *Manipulation of the vortex motion in nanostructured ferromagnetic/superconductor hybrids.* Applied Physics Letters, 2007. **90**(18): p. 182501.

159. Katzir, E., et al., *Enhanced vortex pinning in Nb using proximity effect through organic molecules.* Journal of Physics Communications, 2018. **2**(2): p. 025001.

160. Andreev, A., *Thermal conductivity of the intermediate state of superconductors.* JETP Letters,, 1964. **46**(5): p. 1823-1828.

161. Kramer, R., et al., *Imaging the statics and dynamics of superconducting vortices and antivortices induced by magnetic microdisks.* Physical Review X, 2011. **1**(2): p. 021004.

162. Marchiori, E., et al., *Reconfigurable superconducting vortex pinning potential for magnetic disks in hybrid structures.* Scientific Reports, 2017. **7**: p. 45182.

163. Palau, A., et al., *Guided vortex motion in* $YBa_2Cu_3O_7$ *thin films with collective ratchet pinning potentials.* Physical Review B, 2012. **85**(1): p. 012502.

164. Plourde, B.L., *Nanostructured superconductors with asymmetric pinning potentials: Vortex ratchets.* IEEE Transactions on Applied Superconductivity, 2009. **19**(5): p. 3698-3714.

165. Schoelkopf, R. and S. Girvin, *Wiring up quantum systems.* Nature, 2008. **451**(7179): p. 664-669.

166. Yi, H., S. Remillard, and A. Abdelmonem. *A superconducting thin film filter of very high wide-band rejection*. in *IEEE MTT-S International Microwave Symposium Digest, 2003*. 2003. Philadelphia, PA, USA: IEEE.

167. Ye, S. and C. Sans. *New advances in HTS microstrip filter design*. in *IEEE MTT-S International Microwave Symposium Digest, 2003*. 2003. IEEE.

168. Malozemoff, A.P., J. Mannhart, and D. Scalapino, *High-temperature cuprate superconductors get to work.* Physics Today, 2005. **58**(4): p. 41-6.

169. Hwang, H.Y., et al., *Emergent phenomena at oxide interfaces.* Nature Materials, 2012. **11**(2): p. 103-113.

170. Abrutis, A. and C. Jimenez, *MOCVD" DIGITAL" GROWTH OF HIGH-*T_C *superconductors, related hetrostructures and superlattices*. Recent Developments in Superconductivity Research. 2007. 133.

171. Adachi, S., et al., *Characterization of La-doped YBCO superconducting films deposited by DC magnetron sputtering at various off-axis geometries.* Journal of the Ceramic Society of Japan, 2010. **118**(1381): p. 830-836.

172. Koster, G., D.H. Blank, and G.A. Rijnders, *Oxygen in Complex Oxide Thin Films Grown by Pulsed Laser Deposition: A Perspective.* Journal of superconductivity and Novel Magnetism, 2020. **33**(1): p. 205-212.

173. *MTI Corporation*. 8/03/2019; Available from: [http://www.mtixtl.com/superconductfilmsubstrates.aspx].

174. Boffa, V., et al., *Properties of in-situ laser-pulsed deposited YBCO thin films on MgO with $SrTiO_3$ buffer layer.* Physica C: Superconductivity and its Applications, 1996. **260**(1-2): p. 111-116.

175. Fedoseev, S., *Investigation of superconducting thin films and multilayered structures for electronic applications*. 2014, PhD thesis, University of Wollongong: Australia.

176. Mattox, D.M., *Handbook of physical vapor deposition (PVD) processing*. 2010: William Andrew.

177. *http://www2.physics.colostate.edu/groups/PattonGroup/systems/pld_desc.html*.

178. Haugan, T.J., et al., *Pulsed Laser Deposition of $Y_1Ba_2Cu_3O_{7-\delta}$ Thin Films in High Oxygen Partial Pressures.* MRS Online Proceedings Library Archive, 2001. **689**.

179. Pysarenko, S., *multilayering approach to enhance current carrying capability of YBCO films*. 2010, PhD thesis, University of Wollongong: Australia.

180. Liu, L., et al., *Effect of deposition temperature on the epitaxial growth of YBCO thin films on RABiTS substrates by pulsed laser deposition method.* IEEE Transactions on Applied Superconductivity, 2010. **20**(3): p. 1553-1556.

181. Pysarenko, S.V., A.V. Pan, and S.X. Dou, *Origin of Surface Morphology Variation During Pulsed Laser Deposition of YBCO Superconducting Films.* IEEE Transactions on Applied Superconductivity, 2011. **21**(3): p. 3179-3183.

182. Pan, A.V., et al. *Structure, pinning and supercurrent in $YBa_2Cu_3O_7$ films and $ReBa_2Cu_3O_7$ multilayers*. in *Journal of Physics: Conference Series*. 2006. IOP Publishing.

183. Guo, R., et al., *Surface crystallographic structure compatibility between substrates and high T_C (YBCO) thin films.* Journal of Materials Research, 1994. **9**(7): p. 1644-1656.

184. Avinash P. Nayak, L.V., and M. Saif Islam., *Wet and dry etching*. 2014, University of California.

185. Wayne M. Stauss, T.E.L. http://www.microfabnh.com/ion_beam_etch_technology.php.

186. Barber, D.J., *Radiation damage in ion-milled specimens: characteristics, effects and methods of damage limitation.* Ultramicroscopy, 1993. **52**(1): p. 101-125.

187. Mcelfresh, M., *Fundamentals of magnetism and magnetic measurements featuring quantum design's magnetic property measurement system*. 1994: University of Purdue.

188. Design, Q., *Vibrating Sample Magnetometer (VSM) Option User's Manual*. 2011: USA.

189. Chepikov, V., et al., *Pinning Properties of PLD-Obtained* $GdBa_2Cu_3O_{7-x}$ *Coated Conductors Doped With* $BaSnO_3$. IEEE Transactions on Applied Superconductivity, 2017. **27**(4): p. 1-5.

190. Hänisch, J., et al., *Formation of nanosized* $BaIrO_3$ *precipitates and their contribution to flux pinning in Ir-doped* $Y\,Ba_2Cu_3O_{7-\delta}$ *quasi-multilayers.* Applied Physics Letters, 2005. **86**(12): p. 122508.

191. Kaname, M. and M. Paolo, *Artificial pinning center technology to enhance vortex pinning in YBCO coated conductors.* Superconductor Science and Technology, 2010. **23**(1): p. 014001.

192. Paturi, P., M. Irjala, and H. Huhtinen, *Greatly decreased critical current density anisotropy in* $YBa_2Cu_3O_{6+x}$ *thin films ablated from nanocrystalline and* $BaZrO_3$*-doped nanocrystalline targets.* Journal of Applied Physics, 2008. **103**(12): p. 123907.

193. Menushenkov, A., et al., *Correlation of local structure peculiarities and critical current density of 2G MOCVD YBCO tapes with* $BaZrO_3$ *nanoinclusions.* Superconductor Science and Technology, 2017. **30**(4): p. 045003.

194. Pan, A., et al., *Thermally activated depinning of individual vortices in* $YBa_2Cu_3O_7$ *superconducting films.* Physica C: Superconductivity, 2004. **407**(1-2): p. 10-16.

195. Pan, A.V. and S.X. Dou, *Comparison of small-field behavior in* MgB_2*, Low-and high-temperature superconductors.* Physical Review B, 2006. **73**(5): p. 052506.

196. Kashurnikov, V., et al., *Domain of a magnetic flux in superconductors with ferromagnetic pinning centers.* Physics of the Solid State, 2015. **57**(9): p. 1726-1734.

197. Kashurnikov, V., et al., *The critical current density in the layered superconductors with ferromagnetic nanorods.* Physica C: Superconductivity and its Applications, 2016. **528**: p. 17-22.

198. Geoffroy, O., et al., *Magnetic and transport properties of ferromagnetic particulate arrays fabricated on superconducting thin films.* Journal of Magnetism and Magnetic Materials, 1993. **121**(1–3): p. 223-226.

199. Otani, Y., et al., *Magnetostatic interactions between magnetic arrays and superconducting thin films.* Journal of Magnetism and Magnetic Materials, 1993. **126**(1): p. 622-625.

200. Martin, J.I., et al., *Flux pinning in a superconductor by an array of submicrometer magnetic dots.* Physical Review Letters, 1997. **79**(10): p. 1929.

201. Morgan D. J., K.J.B., *Asymmetric flux pinning in a regular array of magnetic dipoles.* Physical Review Letters, 1998. **80**: p. 3614.

202. Huang, J., et al., *Enhanced Flux Pinning Properties in $YBa_2Cu_3O_{7-\delta}/(CoFe_2O_4)_{0.3}(CeO_2)_{0.7}$ Multilayer Thin Films.* IEEE Transactions on Applied Superconductivity, 2014. **25**(3): p. 1-4.

203. Huang, J., et al., *Enhanced superconducting properties of $YBa_2Cu_3O_{7-\delta}$ thin film with magnetic nanolayer additions.* Ceramics International, 2016. **42**(10): p. 12202-12209.

204. Huang, J., et al., *Self-assembled vertically aligned Ni nanopillars in CeO_2 with anisotropic magnetic and transport properties for energy applications.* Nanoscale, 2018. **10**(36): p. 17182-17188.

205. Huang, J., et al., *Magnetic properties of $(CoFe_2O_4)_x$:$(CeO_2)_{1-x}$ vertically aligned nanocomposites and their pinning properties in $YBa_2Cu_3O_{7-\delta}$ thin films.* Journal of Applied Physics, 2014. **115**(12): p. 123902.

206. Vélez, M., et al., *Superconducting vortex pinning with artificial magnetic nanostructures.* Journal of Magnetism and Magnetic Materials, 2008. **320**(21): p. 2547-2562.

207. Aladyshkin, A.Y., et al., *Nucleation of superconductivity and vortex matter in superconductor–ferromagnet hybrids.* Superconductor Science and Technology, 2009. **22**(5): p. 053001.

208. Martin, J., et al., *Temperature dependence and mechanisms of vortex pinning by periodic arrays of Ni dots in Nb films.* Physical Review B, 2000. **62**(13): p. 9110.

209. Van Bael, M., et al., *Local observation of field polarity dependent flux pinning by magnetic dipoles.* Physical Review Letters, 2001. **86**(1): p. 155.

210. Jones, A., et al., *Modification of Pinning in $YBa_2Cu_3O_7$ Thin Films by Substrate Annealing.* IEEE Transactions on Applied Superconductivity, 2019. **29**(5): p. 1-5.

211. Golovchanskiy, I.A., et al., *Significant tunability of thin film functionalities enabled by manipulating magnetic and structural nano-domains.* Applied Surface Science, 2014. **311**: p. 549-557.

212. Shi, D., et al., *Growth orientation and surface morphology of CeO_2 films deposited by PLD using different deposition atmospheres.* Physica C: Superconductivity, 2001. **356**(4): p. 304-310.

213. Cole, B., et al., *Large-area $YBa_2Cu_3O_{7-\delta}$ thin films on sapphire for microwave applications.* Applied Physics Letters, 1992. **61**(14): p. 1727-1729.

214. Paull, O.H., et al., *Field dependence of the ferromagnetic/superconducting proximity effect in a YBCO/STO/LCMO multilayer.* Nanoscale, 2018. **10**(40): p. 18995-19003.

215. Meaney, S., et al., *Partial carrier freeze-out at the $LaAlO_3/SrTiO_3$ oxide interface.* APL Materials, 2019. **7**(10): p. 101105.

216. Misko, V.R., S. Savel’ev, and F. Nori, *Critical currents in superconductors with quasiperiodic pinning arrays: One-dimensional chains and two-dimensional Penrose lattices.* Physical Review B, 2006. **74**(2): p. 024522.

217. Kang, W., et al., *MgB_2 superconducting thin films with a transition temperature of 39 Kelvin.* Science, 2001. **292**(5521): p. 1521-1523.

218. Deen, M., *The effect of the deposition rate on the properties of dc-magnetron-sputtered niobium nitride thin films.* Thin Solid Films, 1987. **152**(3): p. 535-544.

219. Wells, F.S., et al., *Analysis of low-field isotropic vortex glass containing vortex groups in $YBa_2Cu_3O_{7-\delta}$ thin films visualized by scanning SQUID microscopy.* Scientific Reports, 2015. **5**.

220. Wells, F.S., et al., *Direct measurements of field-dependent ordering in a low-field vortex glass state.* IEEE Transactions on Applied Superconductivity, 2016. **26**(3): p. 1-5.

221. Aytug, T., et al., *Analysis of flux pinning in $Y Ba_2Cu_3O_{7-\delta}$ films by nanoparticle-modified substrate surfaces.* Physical Review B, 2006. **74**(18): p. 184505.

222. Palau, A., et al., *Isotropic and anisotropic pinning in TFA-grown* $YBa_2Cu_3O_{7-x}$ *films with* $BaZrO_3$ *nanoparticles.* Superconductor Science and Technology, 2011. **24**(12): p. 125010.

223. Zuev, Y.L., et al., *Near-isotropic performance of intrinsically anisotropic high-temperature superconducting tapes due to self-assembled nanostructures.* Applied Physics Letters, 2008. **93**(17): p. 172512.

224. Shmidt, V. and G. Mkrtchyan, *Vortices in type-ll superconductors.* Soviet Physics Uspekhi, 1974. **17**(2): p. 170.

225. Grigorenko, A., et al., *Direct imaging of commensurate vortex structures in ordered antidot arrays.* Physical Review B, 2001. **63**(5): p. 052504.

226. Moshchalkov, V., et al., *Pinning by an antidot lattice: The problem of the optimum antidot size.* Physical Review B, 1998. **57**(6): p. 3615.

227. Latimer, M., et al., *Vortex interaction enhanced saturation number and caging effect in a superconducting film with a honeycomb array of nanoscale holes.* Physical Review B, 2012. **85**(1): p. 012505.

228. Berdiyorov, G., M. Milošević, and F. Peeters, *Superconducting films with antidot arrays—Novel behavior of the critical current.* EPL (Europhysics Letters), 2006. **74**(3): p. 493.

229. Pan, A.V., et al., *Direct visualization of iron sheath shielding effects in* MgB_2 *superconducting wires.* Superconductor Science and Technology, 2003. **16**(10): p. L33.

230. Pan, A.V. and S. Dou, *Overcritical state in superconducting round wires sheathed by iron.* Journal of Applied Physics, 2004. **96**(2): p. 1146-1153.

231. Rouco, V., et al., *Geometrically controlled ratchet effect with collective vortex motion.* New Journal of Physics, 2015. **17**(7): p. 073022.

232. Van de Vondel, J., C. de Souza Silva, and V. Moshchalkov, *Diode effects in the surface superconductivity regime.* EPL (Europhysics Letters), 2007. **80**(1): p. 17006.

233. Motta, M., et al., *Controllable morphology of flux avalanches in microstructured superconductors.* Physical Review B, 2014. **89**(13): p. 134508.

234. Ray, D., et al. *Strongly Enhanced Vortex Pinning by Conformal Crystal Arrays*. in *APS Meeting Abstracts*. 2013.

235. Pease, R.F. and S.Y. Chou, *Lithography and other patterning techniques for future electronics.* Proceedings of the IEEE, 2008. **96**(2): p. 248-270.

236. Mallick, S. and S. Bedanta, *Size and shape dependence study of magnetization reversal in magnetic antidot lattice arrays.* Journal of Magnetism and Magnetic Materials, 2015. **382**: p. 158-164.

237. Colauto, F., et al., *Limiting thermomagnetic avalanches in superconducting films by stop-holes.* Applied Physics Letters, 2013. **103**(3): p. 032604.

238. Wells, F.S., et al., *Dynamic magneto-optical imaging of superconducting thin films.* Superconductor Science and Technology, 2016. **29**(3): p. 035014.

239. Sillanpää, M., et al., *Inverse proximity effect in superconductors near ferromagnetic material.* EPL (Europhysics Letters), 2001. **56**(4): p. 590.

240. Kalcheim, Y., et al., *Inverse proximity effect at superconductor-ferromagnet interfaces: Evidence for induced triplet pairing in the superconductor.* Physical Review B, 2015. **92**(6): p. 060501.

241. Iavarone, M., et al., *Visualizing domain wall and reverse domain superconductivity*. 2014, Nature Communications. p. 4766.

242. Aladyshkin, A.Y., et al., *Planar superconductor/ferromagnet hybrids: Anisotropy of resistivity induced by magnetic templates.* Applied Physics Letters, 2009. **94**(22): p. 222503.

243. Buzdin, A.I. and A.S. Mel'nikov, *Domain wall superconductivity in ferromagnetic superconductors.* Physical Review B, 2003. **67**(2): p. 020503.

244. Bulaevskii, L.N., E.M. Chudnovsky, and M.P. Maley, *Magnetic pinning in superconductor-ferromagnet multilayers.* Applied Physics Letters, 2000. **76**(18): p. 2594-2596.

245. Habermeier, H., J. Albrecht, and S. Soltan, *The enhancement of flux-line pinning in all-oxide superconductor/ferromagnet heterostructures.* Superconductor Science and Technology, 2004. **17**(5): p. S140.

246. Albrecht, J., S. Soltan, and H.U. Habermeier, *Magnetic pinning of flux lines in heterostructures of cuprates and manganites.* Physical Review B, 2005. **72**(9): p. 092502.

247. Hubert, A. and R. Schäfer, *Domain observation techniques,* in *Magnetic Domains*. 1998, Springer. p. 11-97.

248. Fritzsche, J., et al., *Local observation of reverse-domain superconductivity in a superconductor-ferromagnet hybrid.* Physical Review Letters, 2006. **96**(24): p. 247003.

249. Curran, P., et al., *Continuously tuneable critical current in superconductor-ferromagnet multilayers.* Applied Physics Letters, 2017. **110**(26): p. 262601.

250. Vlasko-Vlasov, V., et al., *Guiding superconducting vortices with magnetic domain walls.* Physical Review B, 2008. **77**(13): p. 134518.

251. Albrecht, J., et al., *Inhomogeneous vortex distribution and magnetic coupling in oxide superconductor–ferromagnet hybrids.* New Journal of Physics, 2007. **9**(10): p. 379.

252. Habermeier, H.-U. *Ferromagnet-superconductor interfaces: The length scales of interactions*. in *Journal of Physics: Conference Series*. 2008. IOP Publishing.

253. Chen, C., et al., *Suppressed Superconductivity Induced by Spin Diffusion Effect in* $La_{0.67}Sr_{0.33}MnO_3/YBa_2Cu_3O_{7-\delta}$ *Bilayers.* Journal of Superconductivity and Novel Magnetism, 2014. **27**(7): p. 1683-1688.

254. Chen, C., Y. Li, and C. Cai, *Field-suppressed interfacial spin scattering in* $YBa_2Cu_3O_{7-\delta}/La_{0.67}Sr_{0.33}MnO_3$ *heterostructures.* Solid State Communications, 2012. **152**(14): p. 1203-1207.

255. Peng, L., et al., *Magnetic dependent proximity effects of superconductivity and ferromagnetism in* $YBa_2Cu_3O_{7-\delta}/La_{1-x}Ca_xMnO_3$ *bilayers.* Solid State Communications, 2008. **148**(11-12): p. 545-549.

256. Pysarenko, S.V., A.V. Pan, and S.X. Dou, *Origin of Surface Morphology Variation During Pulsed Laser Deposition of* $YBa_2Cu_3O_7$ *Superconducting Films.* IEEE Transactions on Applied Superconductivity, 2011. **21**(3): p. 3179-3183.

257. Holzapfel, B., et al., *Off-axis laser deposition of* $YBa_2Cu_3O_{7-\delta}$ *thin films.* Applied Physics Letters, 1992. **61**(26): p. 3178-3180.

258. Pan, V., et al., *Dislocation model of superconducting transport properties of YBCO thin films and single crystals.* Cryogenics, 1993. **33**(1): p. 21-27.

259. Fedotov, Y.V., et al., *Magnetic-field and temperature dependence of the critical current in thin epitaxial films of the high-temperature superconductor* $YBa_2Cu_3O_{7-\delta}$. Low Temperature Physics, 2002. **28**(3): p. 172-183.

260. Pan, A.V., S.V. Pysarenko, and S.X. Dou, *Quantitative description of critical current density in YBCO films and multilayers.* IEEE Transactions on Applied Superconductivity, 2009. **19**(3): p. 3391-3394.

261. Golovchanskiy, I., et al., *An all-field-range description of the critical current density in superconducting YBCO films.* Superconductor Science and Technology, 2011. **24**(10): p. 105020.

262. Chen, C., et al., *Flux pinning of stress-induced magnetic inhomogeneity in the bilayers of* $YBa_2Cu_3O_{7-\delta}/La_{0.67}Sr_{0.33}MnO_{3-\delta}$. Journal of Applied Physics, 2009. **106**(9): p. 093902.

263. Gaurav, A., et al., *Suppressed* B_{c2} *in a superconducting/ferromagnetic bilayer.* Journal of Physics Communications, 2017. **1**(3): p. 035008.

264. Tinkham, M., *Resistive transition of high-temperature superconductors.* Physical Review Letters, 1988. **61**(14): p. 1658.

265. Chen, C., et al., *Robust high-temperature magnetic pinning induced by proximity in* $YBa_2Cu_3O_{7-\delta}/La_{0.67}Sr_{0.33}MnO_3$ *hybrids.* Journal of Applied Physics, 2011. **109**(7): p. 073921.

266. Brisbois, J., et al., *Magnetic flux penetration in Nb superconducting films with lithographically defined microindentations.* Physical Review B, 2016. **93**(5): p. 054521.

267. Cai, C., et al., *Magnetotransport and flux pinning characteristics in* $RBa_2Cu_3O_{7-\delta}$ *(R=Gd,Eu,Nd) and* $(Gd_{1/3}Eu_{1/3}Nd_{1/3})Ba_2Cu_3O_{7-\delta}$ *high-*T_c *superconducting thin films on* $SrTiO_3$ *(100).* Physical Review B, 2004. **69**(10): p. 104531.

268. Iavarone, M., et al., *Vortex confinement in planar superconductor/ferromagnet hybrid structures.* IEEE Transactions on Magnetics, 2012. **48**(11): p. 3275-3279.

269. Peng, L., et al., *Formation of nanosized* $BaZrO_3$ *and the magnetotransport properties in* $YBa_2Cu_3O_{7-\delta}$*/YSZ quasi-multilayers.* Journal of Physics D: Applied Physics, 2008. **41**(15): p. 155403.